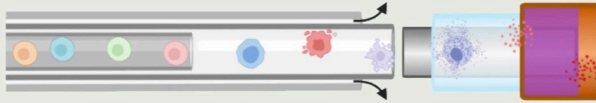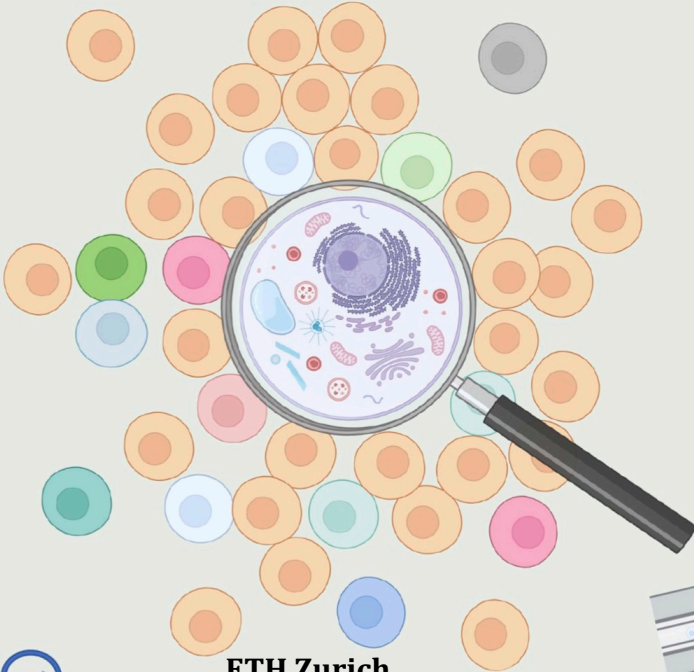# Development and Application of Ambient Ionization Sources for Analyzing Metabolites in Single Cells
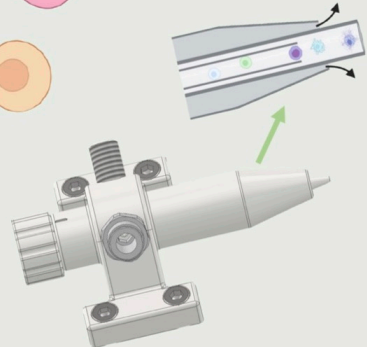
Qinlei Liu

ETH Zurich

2022
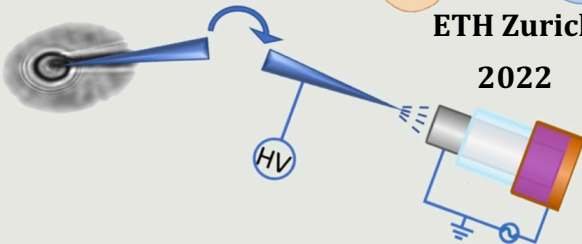
Diss. ETH No. 28759

Development and Application of Ambient Ionization Sources for Analyzing Metabolites in Single Cells

A thesis submitted to attain the degree of

DOCTOR OF SCIENCES of ETH ZURICH

(Dr. sc. ETH Zurich)

presented by

Qinlei Liu

MSc of Chemistry, Sichuan University, China

born on 29.12.1993

citizen of China

accepted on the recommendation of

Prof. Dr. Renato Zenobi

Prof. Dr. Markus Stoffel

2022

Acknowledgements

First of all, I would like to thank Prof. Dr. Renato Zenobi for giving me the opportunity to do my PhD in his group. I appreciated his guidance and support over the years. He encouraged me to work independently and supported my decisions at all times, both of which were very helpful to me.

I am grateful to Prof. Dr. Markus Stoffel for agreeing to be my co-examiner and, more importantly, for his ongoing support of my collaborative projects with Dr. Wenjie Ge. I would like to thank my collaborator Dr. Wenjie Ge at ETH Zurich, it was a great pleasure to collaborate with him.

I appreciate Brigitte Bräm and Pamela Knupp for handling all the financial and administrative work. Big thanks go to Marco Zesiger, Christian Marro and Christoph Bärtschi from the mechanical workshop and Heinz Benz from the electronics for all the assistance they provided.

Many thanks to all the current and former group members of the Zenobi lab. I really enjoyed the happy and cohesive atmosphere of the group and the various fun group activities, including the cheese and wine parties, group hikes, group ski outings and Christmas dinners. Many thanks to the plasma team members (Alina and Sandra), as we always say "our team is small but very powerful", I am very happy that I had a chance to work with you. I also want to thank the other group members that I had a nice time with during my PhD: Bettina, Jiayi, Irina, Masha, Na, Liqing, Nora, Siiri, Despoina, Zhenfeng, Jérôme, Ri, Prince, Jonas, Naresh, Stamatios, Julian, Dusan, Giovanni Luca, Lukas, Philipp, Yash, Adam, Cedric and so on. Thank you all very much for keeping a very nice working environment.

Contents

Abstract

Cellular heterogeneity is essential for physiological functions of organisms, and precise interpretation of the relevant biological mechanisms requires accurate measurement of biomolecules including DNA, RNA, proteins and metabolites at the single-cell level. Cellular metabolites react most rapidly to environmental and biochemical changes, such that the detection of cellular metabolites is a critical step in determining the physiological state of cells. However, their low amounts and structural diversity in single cells and the large variation in the content of different metabolites make single-cell metabolomics analysis technically challenging.

Mass spectrometry, with its high sensitivity, good selectivity, and wide dynamic range, has been widely used in single-cell analysis in recent years. The advancement of single-cell mass spectrometry is inextricably linked to the development of ionization sources, and different ionization methods have their own characteristics and can complement each other.

In this dissertation, home-built ambient ionization sources such as a dielectric barrier discharge ionization (DBDI), a hybrid ionization source combining nanoelectrospray (nanoESI) and DBDI, and a 3D-printed ionization source were used to investigate single-cell metabolomics.

In Chapter 1, some general information about single-cell mass spectrometry is introduced.

In Chapter 2, the basic principles of the methods and instruments used in this thesis are explained.

In Chapter 3, a label-free, rapid single-cell analytical method based on DBDI mass spectrometry, which can detect multiple metabolites in single cells with a throughput of 38 cells/ minute is presented. Several cell types (HEK-293T, PANC-1, CFPAC-1, H6c7, HeLa, and iBAs) were successfully differentiated. In pancreatic

cancer cells, we discovered evidence for abnormal lipid metabolism. We also checked gene expression in a cancer genome atlas dataset and found that the mRNA level of an important enzyme of lipid synthesis (ATP citrate lyase, ACLY) was upregulated in human pancreatic ductal adenocarcinoma (PDAC). Furthermore, both an ACLY chemical inhibitor and a siRNA method targeting ACLY have been shown to reduce the viability of PDAC cells. This study demonstrated that ACLY could be a potential target for treating pancreatic cancer due to a considerable reduction in lipid content in treated cells.

In Chapter 4, a nanoESI-DBDI hybrid ionization source is proposed for single-cell analysis. A capillary with a 1 μm i.d. tip was inserted into cells for sampling and then directly used as the nanoESI source for ionization of polar metabolites. A DBDI source was also used as a post-ionization source to improve the ionization of apolar metabolites in cells that are difficult to ionize using ESI. The classes of identified metabolites can be altered from mostly polar to both polar and apolar to mainly apolar by increasing the voltage of the DBDI source from 0 to 3.2 kV. This study investigated the metabolites in plant cells (onion) and human cells (PANC-1). In ESI mode (3.5 kV), 50 compounds in onion cells and 40 compounds in PANC-1 cells were detected after optimization. In ESI (3.5 kV)-DBDI (2.6 kV) hybrid mode, an additional 49 compounds in onion cells and 73 compounds in PANC-1 cells were observed. This hybrid ionization source improves the coverage, ionization efficiency, and limit of detection of metabolites with different polarities, and could help to promote the rapid development of single-cell metabolomics.

In Chapter 5, an all-in-one 3D-printed ESI source was manufactured for single-cell analysis. This 3D-printed ionization source integrates the cell introduction system, metabolite extraction and ionization source into one unit, simplifying the process of single-

cell analysis and improving the reproducibility of measurement. We were able to successfully perform a high-throughput analysis for three different cancer cell types (around 17 cells/min). We showed the potential of 3D printing for single-cell analysis by using the t-SNE algorithm to distinguish between several cell types depending on selected features. 3D-printed ionization sources are more affordable, quicker to make, and more readily available than other ionization sources.

The findings of this thesis are summarized in Chapter 6, some unresolved questions are highlighted, and suggestions are made for future development in single-cell mass spectrometry.

In the appendix, a project that used ESI to reveal high levels of hydrogen peroxide (H_2O_2) in pancreatic cancer cells is presented. As this project was conducted at the level of cell populations, it has been placed in the appendix rather than in the main text. This study revealed that the oncogenic KRAS mutation enhances the accumulation of H_2O_2 in pancreatic cancer. We also discovered that high levels of H_2O_2 impact cellular metabolites and enhance pancreatic cancer cell survival. These findings highlight the precise roles of H_2O_2 in the development of pancreatic cancer, perhaps opening up new avenues for pancreatic cancer treatment.

Zusammenfassung

Zelluläre Heterogenität ist für die physiologischen Funktionen von Organismen von grosser Bedeutung, und die genaue Interpretation der relevanten biologischen Mechanismen erfordert eine genaue Messung von Biomolekülen wie DNA, RNA, Proteinen und Metaboliten auf Einzelzellebene. Zelluläre Metaboliten reagieren am schnellsten auf Umwelt- und biochemische Veränderungen, sodass der Nachweis zellulärer Metaboliten ein entscheidender Schritt zur Bestimmung des physiologischen Zustands von Zellen ist. Die geringen Mengen und die strukturelle Vielfalt der Metaboliten in einzelnen Zellen sowie die großen Unterschiede im Gehalt der verschiedenen Metaboliten macht die Metabolomanalyse in einzelnen Zellen jedoch eine technischen Herausforderung.

Die Massenspektrometrie mit ihrer hohen Empfindlichkeit, guten Selektivität und großen dynamischen Bereich hat sich in den letzten Jahren in der Einzelzellanalyse durchgesetzt. Die Weiterentwicklung der Einzelzell-Massenspektrometrie ist untrennbar mit der Entwicklung von Ionisierungsquellen verbunden, und verschiedene Ionisierungsmethoden haben ihre eigenen Merkmale und können sich gegenseitig ergänzen.

In dieser Dissertation wurden selbstgebaute Umgebungsionisationsquellen zur Untersuchung der Einzelzellmetabolomik verwendet, wie eine dielektrische Barriereentladungsionisation (DBDI), eine hybride Ionisationsquelle, die Nanoelektrospray (nanoESI) und DBDI kombiniert, und eine 3D-gedruckte Ionisationsquelle.

In Kapitel 1 werden einige allgemeine Informationen über die Einzell-Massenspektrometrie vorgestellt.

In Kapitel 2 werden die Grundprinzipien der in dieser Arbeit verwendeten Methoden und Instrumente erläutert.

In Kapitel 3 wird eine markierungsfreie, schnelle Einzelzell-Analysemethode auf der Grundlage der Massenspektrometrie mit dielektrischer Barrierenentladung vorgestellt, mit welcher mehrere Metaboliten in Einzelzellen mit einem Durchsatz von 38 Zellen/Minute gleichzeitig nachgewiesen werden können. Mehrere Zelltypen (HEK-293T, PANC-1, CFPAC-1, H6c7, HeLa und iBAs) wurden erfolgreich differenziert. In Bauchspeicheldrüsenkrebszellen entdeckten wir Anzeichen für einen abnormalen Lipidstoffwechsel. Wir überprüften auch die Genexpression in einem Krebsgenom-Atlas-Datensatz und stellten fest, dass der mRNA-Spiegel eines wichtigen Enzyms der Lipidsynthese (ATP-Citrat-Lyase, ACLY) in menschlichen duktalen Adenokarzinomen der Bauchspeicheldrüse (PDAC) hochreguliert war. Außerdem wurde gezeigt, dass sowohl ein chemischer ACLY-Inhibitor als auch eine siRNA-Methode, die auf ACLY abzielt, die Lebensfähigkeit von PDAC-Zellen verringert. Diese Studie zeigte, dass ACLY ein potenzieller Angriffspunkt für die Behandlung von Bauchspeicheldrüsenkrebs sein könnte, da der Lipidgehalt in den behandelten Zellen erheblich reduziert wurde.

In Kapitel 4 wird eine nanoESI-DBDI-Hybridionisierungsquelle für die Einzelzellanalyse vorgeführt. Eine Kapillare mit einer 1 μm i.d. Spitze wurde zur Probenahme in die Zellen eingeführt und dann direkt als nanoESI-Quelle für die Ionisierung polarer Metaboliten verwendet. Eine DBDI-Quelle wurde auch als Nachionisierungsquelle verwendet, um die Ionisierung von apolaren Metaboliten in Zellen zu verbessern, die mit ESI nur schwer zu ionisieren sind. Die Klassen der identifizierten Metaboliten können durch Erhöhung der Spannung der DBDI-Quelle von 0 auf 3.2 kV von überwiegend polar über sowohl polar als auch apolar bis hin zu überwiegend apolar verändert werden. In dieser Studie wurden die Metaboliten in Pflanzenzellen (Zwiebel) und menschlichen Zellen (PANC-1) untersucht. Im ESI-Modus (3.5 kV) wurden nach der

Optimierung 50 Verbindungen in Zwiebelzellen und 40 Verbindungen in PANC-1-Zellen nachgewiesen. Im ESI (3.5 kV)-DBDI (2.6 kV)-Hybridmodus wurden zusätzlich 49 Verbindungen in Zwiebelzellen und 73 Verbindungen in PANC-1-Zellen beobachtet. Diese hybride Ionisierungsquelle verbessert die Abdeckung, die Ionisierungseffizienz und die Nachweisgrenze von Metaboliten mit unterschiedlichen Polaritäten und könnte dazu beitragen, die rasche Entwicklung der Einzelzell-Metabolomik zu fördern.

In Kapitel 5 wurde eine All-in-One-3D-gedruckte ESI-Quelle für die Einzelzellanalyse hergestellt. Diese 3D-gedruckte Ionisationsquelle integriert das Zelleinführungssystem, die Metabolitenextraktion und die Ionisationsquelle in einer Einheit, vereinfacht den Prozess der Einzelzellanalyse und verbessert die Reproduzierbarkeit der Messungen. Wir konnten erfolgreich eine Hochdurchsatzanalyse für drei verschiedene Krebszelltypen durchführen (etwa 17 Zellen/min). Wir zeigten das Potenzial des 3D-Drucks für die Einzelzellanalyse, indem wir den t-SNE-Algorithmus verwendeten, um zwischen verschiedenen Zelltypen anhand ausgewählter Merkmale zu unterscheiden. 3D-gedruckte Ionisierungsquellen sind preiswert, schneller herzustellen und leichter verfügbar als andere Ionisierungsquellen.

Die Ergebnisse dieser Arbeit werden in Kapitel 6 zusammengefasst, einige ungelöste Fragen werden hervorgehoben, und es werden Vorschläge für die zukünftige Entwicklung der Einzelzell-Massenspektrometrie gemacht.

Im Anhang wird ein Projekt vorgestellt, bei dem mit ESI hohe Konzentrationen von Wasserstoffperoxid (H_2O_2) in Bauchspeicheldrüsenkrebszellen nachgewiesen wurden. Da dieses Projekt auf der Ebene von Zellpopulationen durchgeführt wurde, wurde es nicht in dem Haupttext, sondern in den Anhang aufgenommen. In dieser Studie ergab sich, dass die onkogene KRAS-

Mutation die H_2O_2-Akkumulation in Bauchspeicheldrüsenkrebszellen erhöht. Wir entdeckten auch, dass hohe H_2O_2-Konzentrationen Auswirkungen auf zelluläre Metaboliten haben und das Überleben von Bauchspeicheldrüsenkrebszellen fördern. Diese Ergebnisse unterstreichen die genaue Rolle von H_2O_2 bei der Entstehung von Bauchspeicheldrüsenkrebs und eröffnen vielleicht neue Wege für die Behandlung von Bauchspeicheldrüsenkrebs.

1. Introduction

In this dissertation, single-cell metabolomics is studied by home-built ambient ionization sources, including a dielectric barrier discharge ionization (DBDI) source, a hybrid ionization source combining nanoelectrospray (nanoESI) and DBDI, and a 3D-printed ionization source. The fundamentals and motivations of single-cell analysis are introduced in Section 1.1. The research contents and difficulties in single-cell analysis are presented in Section 1.2, and we will focus on single-cell metabolomics rather than other single-cell omics. In sections 1.3 and 1.4, the difficulties in single-cell analysis and the research progress of single-cell mass spectrometry are described. The aims and outline of this thesis are summarized in Section 1.5.

1.1   Why study single cells

Cellular heterogeneity exists between individual cells due to differences in intracellular gene expression levels, cellular physiological environment, cell age, and other factors that influence the phenotype of individual cells in culture.[1] Identifying these differences can reveal critical information. Traditional population measurements obscure information on intercellular heterogeneity, which does not yield the true chemical composition and content of individual cells.[2] In addition, rare cell types such as circulating tumor cells (CTCs) or cancer stem cells play significant roles in pathogenic mechanisms and early diagnosis of tumors. However, due to their

low abundance, bulk analysis hardly provides meaningful information for the study of rare cell types.[3] Single-cell analysis, on the other hand, can deliver a wealth of information for the studies of cell physiology and pathology.

1.2   What to study at single-cell level

Various single-cell "omics" approaches have been developed, including single-cell genomics, transcriptomics, proteomics and metabolomics.[4-6] Compared to other single-cell "omics" methodologies, metabolomics provides the most rapid and dynamic information on cellular functions, owing to the dynamic response of the metabolome to the environment on a short time scale (seconds or less), its structural diversity, and the large dynamic range of metabolites.[7-9] Single-cell metabolomics focuses on the determination of small-molecule metabolites with molecular weights less than ~2 kD in specific cells, organs, and organisms, mainly including endogenous and exogenous small molecules (e.g., lactate, sugars, AMP, ADP, ATP, drugs and their metabolites and lipids).[1]

1.3   Difficulties in single-cell analysis

However, single-cell metabolomics is challenging because of the low amounts of single-cell metabolites; for example, the volume of a single *E. coli* cell is around 1 fL, and the intracellular metabolite content is at the fg level, even for metabolites of the central metabolism that are present in high concentrations.[10] Furthermore, intracellular metabolites cannot be amplified and then detected, as is possible for intracellular DNA. Therefore, single-cell metabolomics

2

requires highly sensitive and selective analytical techniques. In addition, in order to increase the coverage of single-cell metabolomics analyses, quantitative or semi-quantitative analysis of as many cellular metabolites as possible is desirable.

1.4 Development of single-cell mass spectrometry

The emergence of diverse single-cell analysis techniques has greatly promoted the development of single-cell research. The main techniques currently used for single-cell analysis include electrochemistry,[11-13] fluorescence microscopy,[14-16] vibrational spectroscopy,[17-19] capillary electrophoresis,[20-21] mass spectrometry[22-26] and so on.

Mass spectrometry is a well-suited assay for single-cell analysis, with high versatility, good sensitivity, fast analysis speed, wide dynamic range, and the ability to analyze thousands of compounds simultaneously. Since mass spectrometry detects the molecular weight of each compound, mass spectrometry-based single-cell analysis methods are universal and do not require fluorescent labeling or derivatization, and they are extensively used in single-cell metabolomics.

Currently, single-cell mass spectrometry methods based on different ionization techniques have been developed for single-cell metabolomics, including nanoelectrospray ionization (nanoESI)-based methods,[24,27-28] matrix-assisted laser desorption/ionization (MALDI)-based methods,[29-31] secondary ionization mass spectrometry (SIMS)-based methods,[26,32-33] and dielectric barrier ionization discharge (DBDI)-based methods.[34-35] These ionization methods have their own characteristics and can complement each other. Below, the corresponding mass spectrometric single-cell

analysis methods are described for each of these four ionization techniques.

1.4.1 ESI-based methods

ESI is a "soft" ionization source with high ionization efficiency and has a wide range of applications in the life sciences.[36] NanoESI offers higher ionization efficiency and sample utilization compared to traditional ESI technology. NanoESI-based single-cell analysis methods generally use a probe or laser for sampling.[24,37]

Some very interesting methods are based on direct aspiration of liquid from certain parts of living cells by a microcapillary that can be moved with a manipulator in 3D with real-time observation under a microscope. After sampling, direct ionization can be performed by nanoESI. Masujima and co-workers have done pioneering work in this field, [24,38-40] developing a "live single-cell MS" (live MS) method and applying it to analyze differences in the distribution of subcellular metabolites in RBL-2H3 (rat leukemia cell line) (Figure 1.1a).[24] Subsequently, they have successfully applied live MS for the analysis of metabolites in plant cells[39,41] and CTCs.[38] This early research using live single-cell MS has inspired many subsequent studies. For example, Yang and co-workers developed a single-probe-based nanoESI source to enable real-time, *in-situ* single-cell metabolomics analysis. They successfully detected several cellular metabolites and low MW anti-cancer molecules, including paclitaxel, doxorubicin, and OSW-1 in single HeLa cells.[42] To achieve real-time analysis of suspended live single cells, they further developed a T-shaped probe and realized the analysis of single colon cancer cells (HCT-116) in suspension.[43] Using this approach, it was possible to track how the metabolites in HCT-116 cells changed after treatment with anticancer drugs. To analyze

metabolites at the subcellular level, Zhang and co-workers used a tungsten probe as a solid-phase microextraction (SPME) probe to directly sample and enrich metabolites in living cells followed by desorbeing/ionizing the enriched metabolites from the tip of the tungsten probe for MS detection.[44] They successfully detected different types of metabolites, including 6 fructans, 4 lipids, and 8 flavone derivatives in single *Allium cepa* cells. To demonstrate the subcellular detection capability of this method, they used a nucleus dye (methylene blue) to stain onion epidermal cells. The stained nuclei and cytoplasm were then sampled and measured separately by ESI-MS, and it was found that the signal intensity of methylene blue in the nucleus was approximately 20x higher than that in the cytoplasm. In general, probe-based sampling methods are direct and can be performed *in situ*, but the complicated sampling operation limits the throughput and reproducibility of this method, and only some metabolites can be detected in individual cells.

Due to the complexity of the intracellular metabolome, nanoESI has also been coupled with separation techniques to reduce interferences between different compounds and improve detection sensitivity and coverage. Capillary electrophoresis (CE) is particularly well suited because only very small injection volumes of liquid sample are required.[45-48] Nemes and co-workers applied CE-ESI-MS to the metabolomic analysis in single cells in developing *Xenopus laevis* embryos (Figure 1.1b),[49] obtaining a limit of detection of ~5-10 nM (50-100 amol) for dual cationic–anionic analysis.[50] More recently, they achieved both single-cell proteomic and metabolomic analysis in *Xenopus laevis* embryos by CE-ESI-HRMS. After *in-situ* microprobe sampling, they tested the embryos' viability and found that they can still develop freely into visually normally behaving tadpoles.[51] Although still on the slow side in terms of throughput, CE-ESI-MS reveals a wealth of metabolite information in

single cells, paving the way for a better understanding of cell metabolism.

In addition to probe-based sampling methods, laser-based sampling approaches have been developed for nanoESI-based single-cell analysis. For example, laser ablation electrospray ionization (LAESI) is a typical laser-based method that utilizes an IR laser with a specific wavelength for desorption and ESI for post-ionization. Vertes and co-workers proposed *in-situ* analysis of individual cells by LAESI-MS at atmospheric pressure.[37,52-53] For example, they analyzed the metabolites in *Allium cepa*, *Narcissus pseudonarcissus* bulbs and *Lytechinus pictus* at the single-cell level, and also analyzed individual epidermal cells from different scale leaves in *A. cepa* bulbs simultaneously, to study metabolic differences.[37] Generally, LAESI uses an optical fiber to deliver the laser beam and is able to analyze large, single cells with an average volume of ~1 nL. However, only a small fraction of the samples is ionized due to the expansion of laser-ablated gaseous samples in three dimensions, which becomes very challenging for the analysis of small cells. Vertes and coworkers thus utilized a capillary to limit the expansion of the ablation plume, improving its overlap with the electrospray plume, which achieved higher ionization efficiency and lower detection limits when compared to conventional LAESI (Figure 1.1c).[52] Using this method, they measured hexose, disaccharide and a trisaccharide in single buccal epithelial cells (with diameters of 30-50 μm, volumes of 14-65 pL/cell), and glycine, trimethylamine dimer, and lipids in individual sea urchin eggs (with diameters of 90-100 μm, volumes of 400-500 pL/cell). These cells are larger than typical animal cells (with diameters of typically 10-30 μm), i.e., LAESI still needs to be improved in terms of sensitivity for single-cell detection.

An isolated measurement of a single cell or low-throughput measurements of several cells may have less biological significance, as hundreds or thousands of measurements are frequently required to generate statistically significant data in biology. Microfluidics-based methods are effective techniques for studying complex biological systems because of their low sample consumption, outstanding performance to handle trace liquids, and high throughput.[54] The channel size of a typical microfluidic device is around 10~100 μm, which is close to the size of cells, and thus the range of operations and processes at the single-cell level can be performed efficiently in microfluidic chips.[55] To enable high-throughput analysis and to obtain biologically meaningful data, microfluidic techniques have been combined with nanoESI for single-cell analysis.[56-60] For example, Zhang and co-workers proposed a capillary microfluidics platform-based flow cytometry ESI-MS (CyESI-MS) technique to achieve high-throughput single-cell analysis (38 cells/min), cell type discrimination, and biomarker screening (Figure 1.1d).[57-58] Liu and co-workers combined nanoESI with microfluidic chips to identify 100 metabolites and 6 protein biomarkers in single cancer cells with a high throughput of 40 cells/min, and they successfully distinguished different cell types based on the information of simultaneously detected proteins and metabolites.[59] These methods open the door for higher throughput single-cell analyses, to obtain statistically significant data.
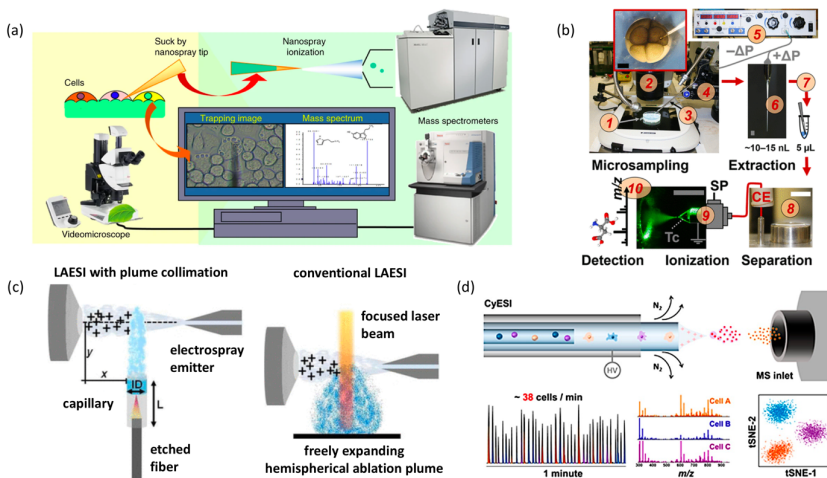
Figure 1.1. Examples of ESI-based single-cell mass spectrometry. (a) Schematic of live plant single-cell MS. Reprinted with permission from ref. 24 Copyright 2015 Springer Nature. (b) Microprobe single-cell CE-ESI-MS enabling *in-situ* metabolic characterization of live Xenopus laevis embryos. Reprinted with permission from ref. 49. Copyright 2017 American Chemical Society. (c) Schematic of LAESI (top view) with plume collimation (left) and side view of conventional LAESI (right). Reprinted with permission from ref. 52. Copyright 2013 American Chemical Society. (d) Schematic of a CyESI-MS detection system. Reprinted with permission from ref. 57. Copyright 2019 American Chemical Society.

1.4.2 MALDI-based methods

Matrix-assisted laser desorption/ionization source (MALDI) is a soft ionization method used for investigating large molecules. MALDI-MS measurements require mixing the sample with a matrix and then irradiating the sample with a UV laser beam, usually in high vacuum. The analytes are then desorbed and ionized, and enter the mass spectrometer for detection. MALDI has been widely used in the field of single-cell analysis due to its high spatial resolution and sensitivity.[25-26,29,32,61-64] It is sensitive, fast, and is able to provide

simple mass spectra of the analytes even from complex mixtures. MALDI is a particularly powerful tool for lipid analysis.

Sweedler and co-workers used MALDI Fourier-transform ion cyclotron resonance (FTICR)-MS, to analyze over 30,000 individual rat cerebellar cells, and t-distributed stochastic neighbor embedding (t-SNE) to distinguish different subtypes of cells (Figure 1.2a).[65] In this work, FTICR-MS provided high mass resolution and mass accuracy, allowing 500 brain lipids to be assigned without the need for performing MS/MS. This is probably one of the largest numbers of cells analyzed in a single-cell MS experiment. In addition, they combined MALDI-MS and immunocytochemistry (ICC) to analyze lipids in astrocytes and neurons, revealing the lipid heterogeneity between these two cell types.[63] Although MALDI-MS enables high-throughput analysis of lipids for a variety of cells, it is usually not quantitative, and many low-molecular-weight metabolites are not detected due to interferences from the MALDI matrix. Sweedler *et al.* therefore coupled MALDI with CE-ESI-MS to effectively increase the throughput of single-cell analysis and improve the coverage of metabolites.[61]

To simplify the sample preparation process and improve the throughput of single-cell analysis, our group developed a high-density micro-array for mass spectrometry (MAMS) chips that can automatically generate pL aliquots that contain single cells from a cell suspension with the appropriate density (Figure 1.2b).[66-68] For example, we studied the ATP metabolism and glycolytic metabolic pathway in single yeast cells with MAMS-MALDI-MS, and also compared the results of single-cell analysis with those from population measurements.[67-68] Although the trends were consistent, there was a significantly higher variability in the results of the single-cell analysis that was not found in the population measurements, exactly as expected. In order to obtain multi-level information on

single cells, we also combined MALDI-MS with Raman and fluorescence microspectroscopy to monitor the growth of single cells of green algae.[62,69] These three methods applied to the same cells yielded complementary information and successfully identified metabolites such as ATP, ADP, astaxanthin, chlorophyll and β-carotene.

Mass spectrometry imaging (MSI) is a powerful and label-free technique for the untargeted investigating the spatial distribution of metabolites in single cells, and MALDI is the most useful and widespread ionization source type for MSI.[70-73] Although MALDI-MSI is a promising technique for chemical imaging of cell membranes, the ionization efficiency of MALDI is low. To address this problem, Dreisewerd and colleagues developed MALDI-2 to enhance the signal for membrane components other than some highly concentrated lipids via a postionization strategy (Figure 1.2c).[70] In contrast to prior photoionization investigations that were performed in high vacuum ($p \leq 10^{-6}$ mbar),[71-72] MALDI-2 uses a pulsed ultraviolet (UV) laser beam that intercept the expanding particle plume in an N_2 cooling gas environment.[73-74] By beam shaping and placing the focusing lens inside the MALDI ion source, the effective diameter of the primary laser beam reached 5 μm. The technology has improved the sensitivity of some molecules such as drug compounds[75] and lipids,[76] and it recently achieved a pixel size of 600 nm with brain tissue by employing transmission-mode MALDI-2 MSI.[64] This technique could be a valuable new tool for cell biology and biomedical research.
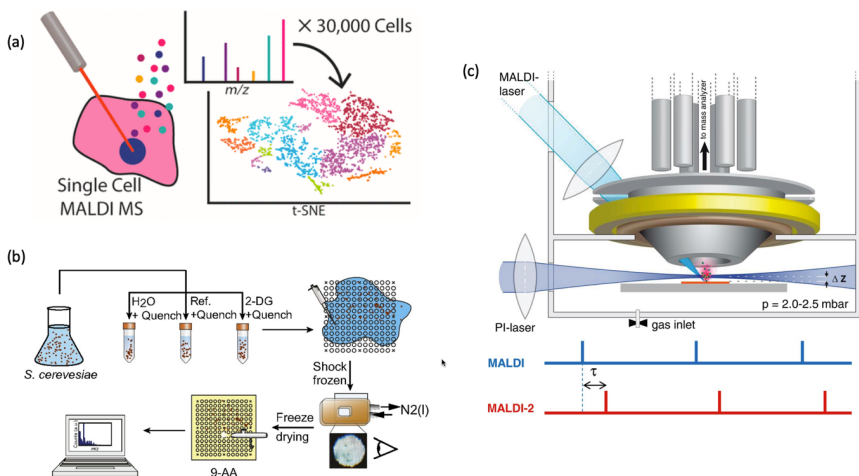
Figure 1.2. Examples of MALDI-based single-cell mass spectrometry. (a) Single-cell MALDI-MS for lipid analysis. Reprinted with permission from ref. 65. Copyright 2019 American Chemical Society. (b) Graphical summary of the workflow used to prepare samples for single-cell MALDI-MS analysis. Reprinted with permission from ref. 68. Copyright 2013 National Academy of Science. (c) Schematics of MALDI-2 ion source. Reprinted with permission from ref. 70. Copyright 2015 The American Association for the Advancement of Science.

1.4.3 SIMS-based methods

Secondary-ion mass spectrometry (SIMS) is a surface analysis technique with high sensitivity and spatial resolution, which usually uses a high-energy primary ion beam to bombard the sample surface and sputter molecules off the sample surface to generate secondary ions that are characteristic for the chemical composition of the sample (Figure 1.3a).[77-78] Although SIMS is a relatively "hard" ionization source compared to MALDI and ESI, the greatest advantage of SIMS over other ionization sources is its extremely high spatial resolution, which can reach down to a few 10s of nm. SIMS is capable of analyzing small molecules such as metabolites, lipids, and

peptide fragments. Therefore, SIMS has been widely used for subcellular analysis and mass spectrometry imaging.[26,32-33] For example, the Ewing group has pioneered many SIMS imaging approaches for subcellular analysis. They used TOF-SIMS imaging to investigate changes in membrane structure driving the formation of lipid structural domains in mating *Tetrahymena thermophila*,[79-80] and the high sensitivity and resolution of SIMS contributed to the understanding of domains in cell membranes. In addition, they applied SIMS to image the fly brain and demonstrate that the drug methylphenidate alters the lipid composition. In order to find a correlation between the chemical and morphological structure of the brain, they used scanning electron microscopy (SEM) imaging along with SIMS imaging.[81] This discovery helped to clarify the relationship between biomolecular distribution and brain function. They also combined nanoSIMS with transmission electron microscopy (TEM) to visualize subvesicular compartmentalization and used it to identify the absolute concentration of dopamine in discrete vesicular compartments and whole vesicles.[82] This technique increases the possibility of absolute quantification and direct measurement of the specific contents of nanometer-scale organelles.

Although TOF-SIMS has a high spatial resolution for imaging single cells, it typically lacks the very high mass-resolving power, mass accuracy, and MS/MS capability necessary for the identification of biomolecules. Gilmore and co-workers have developed a 3D OrbiSIMS that combines a TOF-SIMS and an Orbitrap mass analyzer to achieve high-speed imaging, good resolution, and excellent sensitivity (Figure 1.3b).[83] The 3D OrbiSIMS is capable of visualizing exogenous and endogenous metabolites in 3D with subcellular resolution; for example, they imaged the distribution of neurotransmitters—gamma-aminobutyric acid (GABA), dopamine

and serotonin—in the mouse hippocampus (Figure 1.3c). They also putatively identified and mapped the subcellular distribution of 45 glycerophospholipids and 29 sulfoglycosphingolipids, and used tandem mass spectrometry to confirm the lipid identities. This technique captured hundreds of metabolites at subcellular resolution in a single measurement, resulting in a rich, multiplexed data set. It has the potential to shed light on basic biological processes.
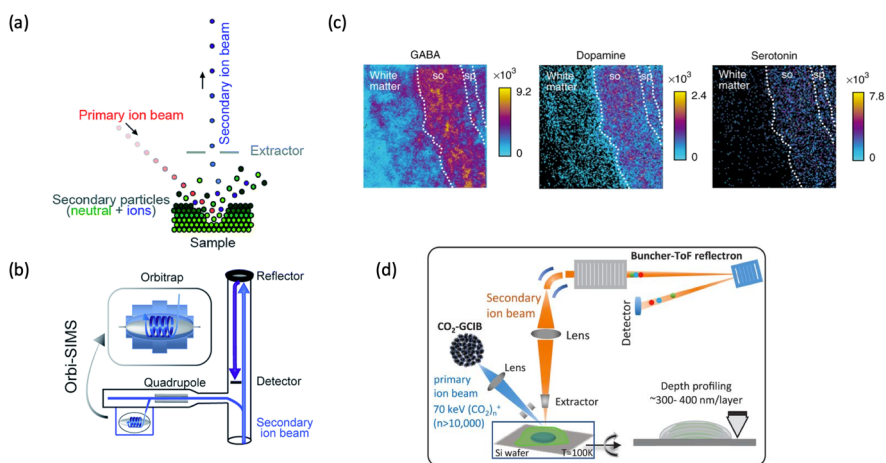
Figure 1.3. Examples of SIMS-based single-cell mass spectrometry. (a) Principle of a SIMS measurement. A primary ion beam sputters the sample surface to generate secondary particles, including neutral particles and ions. The secondary ions are then extracted into the mass spectrometer. Reprinted with permission from ref. 77. Copyright 2019, The Royal Society of Chemistry. (b) Schematic of the 3D OrbiSIMS. Reprinted with permission from ref. 77. Copyright 2019, The Royal Society of Chemistry. (c) 3D OrbiSIMS mapping of GABA, dopamine, and serotonin in the cornu ammonis region of the mouse hippocampus. Reprinted with permission from ref. 83. Copyright 2017, Springer Nature. (d) Schematic of GCIB-SIMS imaging of HeLa cells. Reprinted with permission from ref. 85. Copyright 2020, The American Association for the Advancement of Science.

Another limitation of SIMS is that its analysis of biological samples produces obvious fragmentation, so molecules are hardly desorbed and measured intact. Gas cluster ion beams (GCIBs) have been used for SIMS-based MSI, because they produce less fragmentation than liquid metal ion guns but still provide excellent spatial resolution (<3 µm).[78,84] For example, Benkovic and co-workers performed low-chemical-damage, *in-situ,* three-dimensional chemical imaging analyses of intact molecular ions of metabolites using GCIB-SIMS (Figure 1.3d), such as their analysis of the de novo purine biosynthesis in single HeLa cells.[85]

1.4.4 plasma-based methods

The low-temperature plasma (LTP)-based ionization source is highly efficient, easy to operate, and low cost. It is responsive to both polar and non-polar compounds, due to the presence of various reactive species in a plasma, such as electrons, ions, neutral atoms, excited states, radicals, and photons.[86-89]

The DBDI source, a type of LTP source, has been widely used in the field of mass spectrometry.[90-93] Our lab developed an active capillary plasma ionization based on the DBDI source, which guarantees almost 100% ion transport efficiency due to its direct connection to the inlet capillary of the mass spectrometer.[94-102] Since DBDI does not require a vacuum working environment and the associated complex sample preparation process, and its ionization process is soft, we have recently applied the DBDI source to the field of single-cell metabolomics.[34-35] We developed a high-throughput (~38 cells/min), label-free DBDI-MS-based single-cell analytical method. Based on the measured metabolites, we were able to distinguish multiple cell types, including HEK-293T, PANC-1, CFPAC-1, H6c7, HeLa and iBAs (Figure 1.4a). In addition, we observed an

abnormal lipid metabolism in pancreatic cancer cells by DBDI-MS, and then proposed and validated that it was caused by the dysregulation of ATP citrate lyase (ACLY). Therefore, ACLY was proposed to be a potential biomarker of pancreatic cancer.[34]

Metabolites in cells are diverse and vary in polarity. ESI is a powerful tool for the detection of polar metabolites, but it is not easy to ionize non-polar metabolites in single cells by ESI alone. Without information on non-polar metabolites, some important information may be overlooked in the study of single-cell metabolomics. In order to enhance the coverage of metabolites of different polarity in single cells, our lab reported a hybrid ionization source that combines ESI source and DBDI source to improve analyte coverage in single cells, mainly targeting non-polar metabolites (Figure 1.4b). In brief, the hybrid ionization source can operate in both ESI mode and ESI-DBDI hybrid mode. The ESI mode is mainly used to ionize polar metabolites, and nonpolar or less polar metabolites can be well ionized in the hybrid mode (Figure 1.4c). The classes of measured metabolites can be shifted from largely polar, to both polar and nonpolar, to mostly nonpolar by increasing the voltage of the DBDI source from 0 to 3.2 kV. In this work, we demonstrated the capability of the ESI-DBDI combination on human cells (PANC-1) and plant cells (onion). The method significantly increased the number of analytes detected from a single cell. Specifically, 40 metabolites in PANC-1 cells and 50 metabolites in onion cells were measured in ESI mode (3.5 kV). In hybrid mode, an additional 73 metabolites in PANC-1 and 49 metabolites in onion cells were detected.[35]

Although currently only a few groups use DBDI to analyze single cells, we believe it has the potential to be a very useful tool for single-cell metabolomics, due to its powerful ability to detect a wide range of various metabolites in cells.
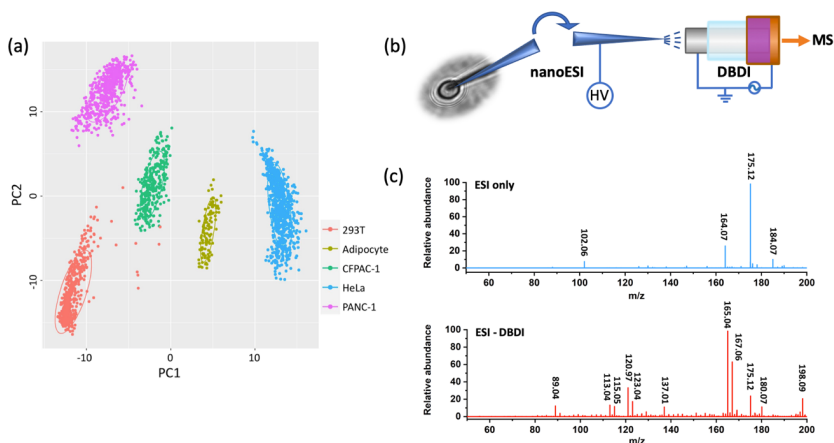
Figure 1.4. Examples of plasma-based single-cell mass spectrometry. (a) Principal component analysis (PCA) of HEK-293T, PANC-1, CFPAC-1, H6c7, HeLa and iBAs cells measured by DBDI-MS. Reprinted with permission from ref. 34. Copyright 2021, John Wiley & Sons. (b) Schematic of the nanoESI-DBDI ionization source. Reprinted with permission from ref. 35. Copyright 2022, American Chemical Society. (c) Mass spectra of onion cells acquired in the ESI (3.5 kV) mode and ESI (3.5 kV)–DBDI (2.6 kV) hybrid mode. Reprinted with permission from ref. 35. Copyright 2022, American Chemical Society.

1.5   Aims and Outline of this Thesis

The study of metabolic heterogeneity in cells is essential to understanding the physiological functions of cells and the pathogenesis of diseases. Therefore, it is necessary to investigate single-cell metabolomics. In this dissertation, we applied home-built ambient ionization sources, including a DBDI source, a nanoESI-DBDI hybrid source and a 3D-printed ionization source, to investigate single-cell metabolomics.

In Chapter 1, some general information of single-cell mass spectrometry, focusing on the ESI-based methods, MALDI-based

methods, SIMS-based methods and plasma-based methods, are introduced.

The methods and instruments used in this thesis are described and explained in Chapter 2. Amongst them are a DBDI source, a nanoESI-DBDI hybrid source, a 3D-printed ionization source, as well as a cell introduction system and mass spectrometry in general.

In Chapter 3, a high-throughput, label-free and sensitive DBDI-MS platform was developed for the analysis of single-cell metabolites, with a throughput of approximately 38 cells per minute. Several cell types were successfully differentiated (HEK-293T, PANC-1, CFPAC-1, H6c7, HeLa, and iBAs) by the DBDI-MS platform. The abnormal lipid metabolism occurring in pancreatic cancer cells was investigated using the DBDI-MS platform.

In Chapter 4, a hybrid ESI + DBDI ionization source for single-cell analysis is proposed. Both ESI and hybrid modes can be used to operate the hybrid source. Polar metabolites are effectively ionized in ESI mode. Nonpolar or less polar metabolites show good ionization efficiency in hybrid mode. The classes of ionized metabolites in cells can be shifted from mainly polar to both polar and apolar to mostly apolar by gradually raising the DBDI voltage from 0 to 3.2 kV. Using this source, metabolites in human (PANC-1) and plant cells (onion) were investigated.

In Chapter 5, an all-in-one 3D-printed ESI source for single-cell analysis was developed. Using this 3D-printed ionization source, we performed a high-throughput analysis on three types of cancer cells (at a throughput of around 17 cells/min). We used the t-SNE algorithm to differentiate different cell types based on measured metabolites.

The conclusions of this thesis are given in Chapter 6, along with an outlook on the future trends of single-cell analysis.

The appendix contains a description of another project that did not use single cell mass spectrometry. The effect of high levels of

hydrogen peroxide (H_2O_2) in pancreatic cancer cells was investigated by ESI-MS. This study revealed that the oncogenic KRAS mutation enhances the accumulation of H_2O_2 in pancreatic cancer. We also discovered that high levels of H_2O_2 affect cellular metabolites and enhances pancreatic cancer cell survival.

Methods and Instrumentation

This chapter explains the basic principles of the methods and instruments used in this thesis.

2.1 DBDI-MS platform

The setup of DBDI-MS platform used in Chapter 3 includes a cell introduction system followed by the dielectric barrier discharge ionization source and a mass analyzer (Figure 2.1). The cell introduction system and the DBDI source are described in detail in the following sections.
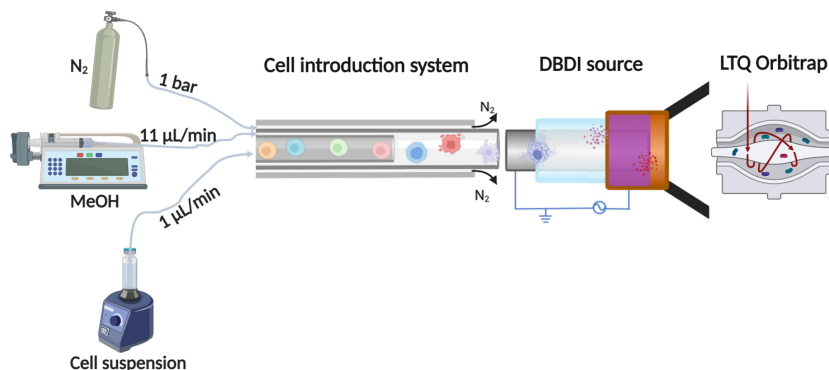
Figure 2.1. The specific configuration and operation details of DBDI-MS platform, including: cell introduction system, a DBDI source, and an LTQ Orbitrap. Reprinted with permission from ref. 34. Copyright 2021, John Wiley & Sons.

2.1.1 DBDI source

The home-built DBDI source from our lab has two electrodes (Figure 2.2), an inner electrode (grounded, stainless steel, ID: 0.6 mm and OD: 1.0 mm) and an outer electrode (high voltage, copper, ID: 1.55 mm, around a glass capillary). They are isolated by a glass capillary that acts as a dielectric barrier. A plasma is ignited inside the capillary when a high alternating current (AC) voltage is applied to the outer electrode. The ignition voltage of the plasma is around 2.0 kVpp. The operating AC voltage of the DBDI source is 2.2–3.2 kVpp. The discharge gas can be nitrogen, oxygen, carbon dioxide or air. The DBDI source is directly connected to the inlet capillary of the mass spectrometer, resulting in almost 100% ion transmission efficiency. The performance of the plasma source is affected by various operating parameters, including the applied high-voltage, discharge gas, frequency, and humidity.
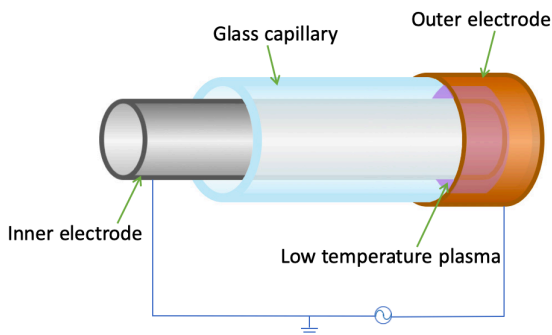
Figure 2.2. The specific configuration of the home-built DBDI source.

2.1.2 Cell introduction system

The cell introduction setup was placed 2 mm in front of the DBDI source. As shown in Figure 2.1, the main parts of the cell introduction setup were 3 coaxial capillaries, two of which are fused silica

capillaries and one is a metal capillary. The inner capillary (193 μm O.D., 75 μm I.D.) was used to introduce a cell suspension from a sample vial. The intermediate capillary (350 μm O.D., 250 μm I.D.) was used to deliver MeOH which worked as extraction fluid. The exit end of the inner capillary was 4 mm shorter than that of the intermediate one (after optimization, Figure S3.3). When cells flowed out of the inner capillary and contacted with MeOH in the intermediate capillary, they were lysed and metabolites of the cells were extracted online by MeOH. Nitrogen, flowing through the outer metal capillary, was used as an auxiliary gas to help the solvent evaporate and cells fly into the DBDI.

2.1.3 Procedure for DBDI-MS Single Cell Analysis

The DBDI-MS platform was composed of three main parts, including a cell introduction system, a DBDI source, and an LTQ Orbitrap (Figure 2.1). Before cell introduction, the inner capillary was thoroughly rinsed with a 140 mM NH_4COOH aqueous solution, and the intermediate capillary was thoroughly rinsed with MeOH until the background total ion chromatogram (TIC) is stable. As shown in Figure 2.1, the freshly prepared cell suspension was introduced into the inner capillary at a flow rate of 1 μL/min, MeOH was introduced into the intermediate capillary at a flow rate of 11 μL/min, the contact time between MeOH and cell suspension was less than 1s. Then the cell contents were ionized by DBDI and detected by a high-resolution Orbitrap mass spectrometer. After each measurement, all capillaries should be flushed with MeOH for 10 minutes at a flow rate of 7 μL/min. The effects of lysis/extraction fluid on single-cell analysis and MeOH flow rate have been optimized (Figure S3.5 and Figure S3.6).

2.2 Hybrid nanoESI-DBDI source

The hybrid ionization source used in chapter 4 includes an electrospray ionization source followed by a home-built DBDI source (described in section 2.1.1) for post-ionization (Figure 2.3). The hybrid source has two modes: an "ESI mode" and a "hybrid mode" to detect intracellular metabolites with different polarities.
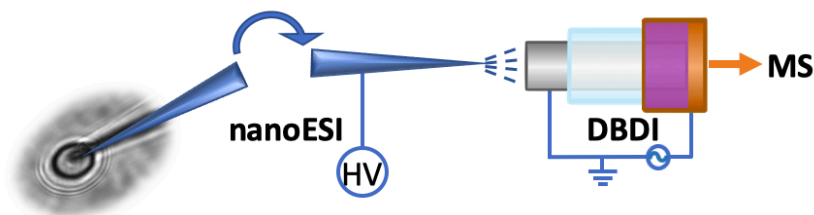
Figure 2.3. The specific configuration of hybrid ionization source. Reprinted with permission from ref. 35. Copyright 2022, American Chemical Society.

2.2.1 Home-built nanoESI source

A micropipette puller (P-1000, Sutter Instruments) was used to fabricate capillaries with a 1 μm ± 10% tip ((B100-75-10, Sutter Instruments, California). The pulled capillaries were used as nanospray emitters. After the cell sampling, the tip of the pulled capillary was backfilled with 2 μL of an assistant solvent. A platinum wire of 200 μm in diameter and 4 cm in length was inserted into the pulled capillary to provide an electrical connection to the assistant solution close to the tip of the capillary, and a high direct current (DC) voltage (3.5 kV) was then applied to the electrode to generate an electrospray.

2.2.2 Single-Cell Sampling

In this work, the metabolites in human (PANC-1) and plant cells (onion) were investigated.

The epidermal cell layer of yellow onion bulbs was freshly peeled and placed on a glass slide, which was then placed on the platform of an inverted microscope (Nikon Eclipse Ti Light Microscope). Next, the pulled capillary was inserted into a capillary holder installed on a home-built manipulator. By adjusting the angle and distance between the tip of the capillary and the cell, the capillary was carefully inserted into the cell. The sampling process was observed by optical microscopy (as shown in Figure 2.4b). Around 30% of the cytoplasmatic cell content was extracted by applying a negative pressure (-0.1 bar) applied by the syringe on the back of the capillary holder. After the cell sampling, the tip of the pulled capillary was backfilled with 2 μL of an assistant solvent.

The subsequent single PANC-1 cell sampling method was the same as for single onion cells. Sampling images of PANC-1 cell and onion cell are shown in Figure 2.4a.
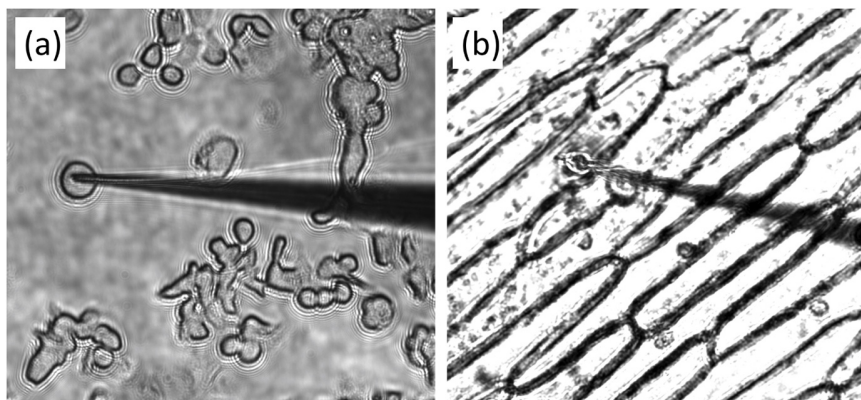
Figure 2.4. Sampling images of (a) PANC-1 cell and (b) onion cell. Reprinted with permission from ref. 35. Copyright 2022, American Chemical Society.

2.3 3D-printed ionization source

The 3D-printed ionization source used in chapter 5 was designed by Autodesk Inventor Professional 2021 (California, USA) and printed using "VisiJet M2R-CL" material (3D Systems, California, USA) by a professional 3D printer (ProJet MJP 2500, 3D Systems, California, USA). After printing, the 3D-printed ionization source was cleaned with steam and isopropanol, then dried for 24 hours in an oven before use. The technical drawing in Figure 2.5 outlines the details of the 3D-printed ionization design. In a nutshell, Figure 2.5 displays the three channels that make up the all-in-one 3D-printed ESI source. The external channel (1 mm I.D.) was used for gas introduction. MeOH was introduced as an extraction solution from the intermediate channel (300 m I.D.). The internal channel (200 m I.D.) of the 3D-printed ionization source was used to insert a fused silica capillary (193 m O.D., 75 m I.D.) to deliver cell suspensions.

Before cell introduction, the intermediate channel was carefully washed with MeOH, and the inner capillary was thoroughly rinsed with a 140 mM NH_4COOH aqueous solution until the background total ion chromatogram (TIC) remained stable. After optimization, the freshly prepared cell suspension was injected into the inner capillary at a flow rate of 1 μL/min, while MeOH was introduced into the intermediate channel at a flow rate of 10 μL/min. A DC voltage of 5.0 kV was applied to the MeOH through an electrode, creating a stable electrospray at the tip of the intermediate channel. As shown in Figure 2.5, the outlet end of the intermediate channel was 4 mm longer than the outlet end of the inner capillary. When the cell suspension exits the inner capillary and comes into contact with MeOH in the intermediate channel, the cells are lysed and metabolites in the cells are extracted into MeOH and nebulized into the mass spectrometer with the assistance of a flow of nitrogen sheath gas in the external channel. All channels were flushed with

MeOH for 10 minutes at a flow rate of 7 L/min following each measurement.
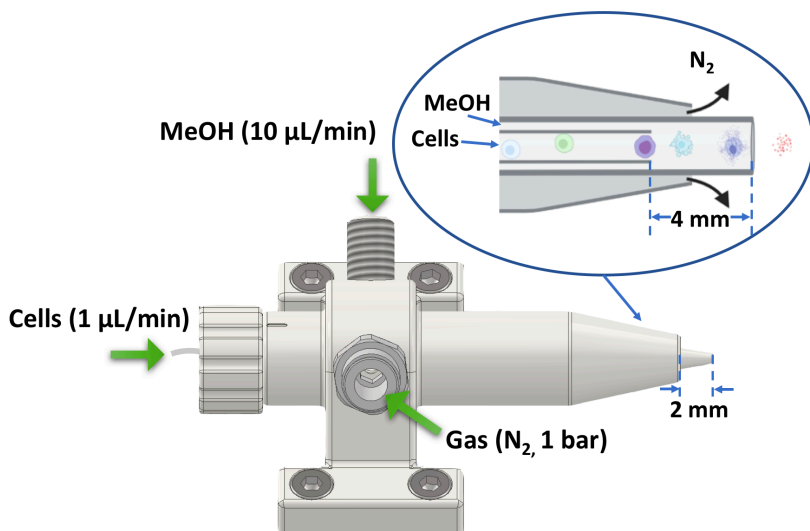
Figure 2.5. Schematic diagram of the 3D-printed ionization source.

2.4 Mass Spectrometer

The concept of separating ions and detecting them by mass-to-charge ratio (m/z) is the foundation of mass spectrometry-based techniques. The separation of ions is accomplished using a magnetic, electric or field-free region, depending on the type of mass spectrometer being used. Different mass spectrometers have different strengths and weaknesses, and the choice of mass spectrometer can be made based on the application.

In this thesis, we used an LTQ Orbitrap mass spectrometer (Thermo Fisher Scientific, San Jose) for all the single-cell measurements. The LTQ Orbitrap is a hybrid mass spectrometer composed of a linear quadrupole ion trap (LTQ) and a high-

resolution Orbitrap. The basic principle of these two mass analyzers is thoroughly introduced in the following sections.

2.4.1 Linear Quadrupole Ion Trap

Ions can be stored, isolated, dissociated, and ejected using a linear quadrupole ion trap. It is made up of four hyperbolic rods that are separated into three sections (Figure 2.6). The ions are contained axially by applying various direct current (DC) voltages to the three sections on each rod and radially by applying radio frequency (RF) voltage to the opposing rod pairs. Through the exit rods, the ions can be radially ejected into the detector (slot in the center rods). The ions are ejected due to m/z selective instability caused by ramping up the RF voltage and applying additional AC voltage to the exit rods.[103]
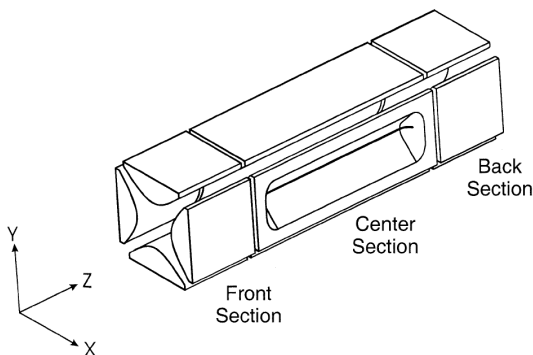
Figure 2.6 Basic design of the two-dimensional linear ion trap. Reprinted with permission from ref. 103. Copyright 2002, Elsevier.

The main benefit of a linear quadrupole ion trap is that it can confine a larger number of ions than a three-dimensional quadrupole ion trap can due to its physical size. As a result, the trapping device experiences the onset of space charge repulsion and

accompanying loss of mass resolution and change in mass assignment only with higher ion loading. The linear quadrupole ion trap retains nearly all of the useful operating characteristics of the three-dimensional quadrupole ion trap, including collisional focusing, resonant excitation and ejection, multiple stages of mass selectivity for tandem mass spectrometry (MS^n), axial modulation, and mass resolution variation as a function of mass-selective ion ejection scanning rate.

The linear quadrupole ion trap from Thermo Fisher is known as the LTQ. The schematic diagram of the LTQ mass spectrometer has been shown in Figure 2.7. In short, the mass analyzer is kept free of big droplets and particles by the ion sweep cone. By adding a mass-dependent potential to the tube lens, the heated ion transfer capillary further desolvates the ions before focusing them on the skimmer. The lower-pressure ion guidance zone is separated from the high-pressure ion source interface (1 Torr) by the skimmer (50 mTorr). Three distinct ion guides (Q00, Q0, and Q1 lenses) focus on the ions such that they are directed toward the linear quadrupole ion trap. The conversion dynode and channel electron multiplier, which are off-axis to the mass analyzer, are where the ions are detected. To improve the mass resolution and sensitivity, helium is employed as the dumping gas in the mass analyzer cavity. This is due to ion collisions with helium, which decreases the kinetic energy of the ions, resulting in enhanced focus on the axis. Helium is also used as a collision gas for collision-induced dissociation.
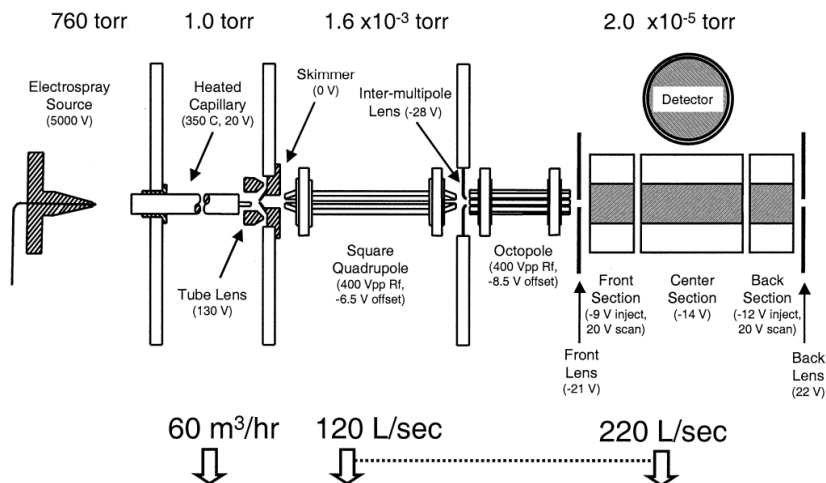
Figure 2.7 The schematic diagram of the LTQ mass spectrometer with typical operating voltages and pressures. Reprinted with permission from ref. 103. Copyright 2002, Elsevier.

2.4.2 Orbitrap

The high-resolution Orbitrap consists of a central electrode (spindle-shaped) surrounded by two outer electrodes (Figure 2.8). Ions are injected tangentially into the Orbitrap and rotate around the central electrode, along with radial and axial (along with the z-axis) harmonic oscillations. The oscillating ions generate image currents, which are detected by two external electrodes and converted to a spectrum of axial oscillations by the Fourier transform.[104] The standout characteristics of the Orbitrap are high resolving power and precise mass. The degree of each varies on the precise Orbitrap type and mode of operation. Mass precision is typically in the range of 0.5-3 ppm, and spectra are typically obtained at a resolving power of R = 20,000-200,000.
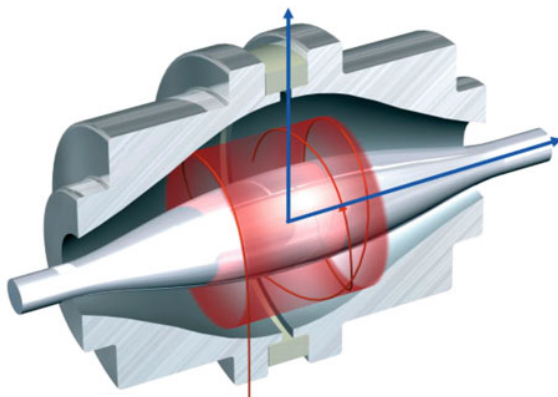
Figure 2.8 A cut-away view of the Thermo Fisher Orbitrap™ mass analyzer. Ions are moving in spirals around a spindle-like-shaped central electrode (a) that creates an axial field gradient. An outer electrode (b) is split in half by an insulating ceramic ring (c). An image current induced by moving ions is detected via a differential amplifier between the two halves of the outer Orbitrap electrode. The m/z of different ions in the Orbitrap can be determined from respective frequencies of oscillation after a Fourier transform. Reprinted with permission from ref. 104. Copyright 2006, John Wiley & Sons.

2.4.3 LTQ-Orbitrap

In this thesis, a commercially available hybrid instrument, the LTQ Orbitrap from Thermo Fisher was used (Figure 2.9).[105] An atmospheric pressure ionization source, a linear quadrupole ion trap, a c-trap, and an Orbitrap comprise the LTQ Orbitrap. The C-trap is a bent RF quadrupole that captures and heats the ions before injecting them into the Orbitrap. Differential pumping is used along the LTQ and after the C-trap to achieve a vacuum in the Orbitrap of roughly 10^{-10} mbar. The hybrid of LTQ and Orbitrap enables for simultaneous MS and MS^n investigations, such as MS in the ion trap and MS^2 in the Orbitrap, as well as reverse. The low mass range is covered by the

LTQ, whereas the Orbitrap provide a high mass resolution and accuracy.
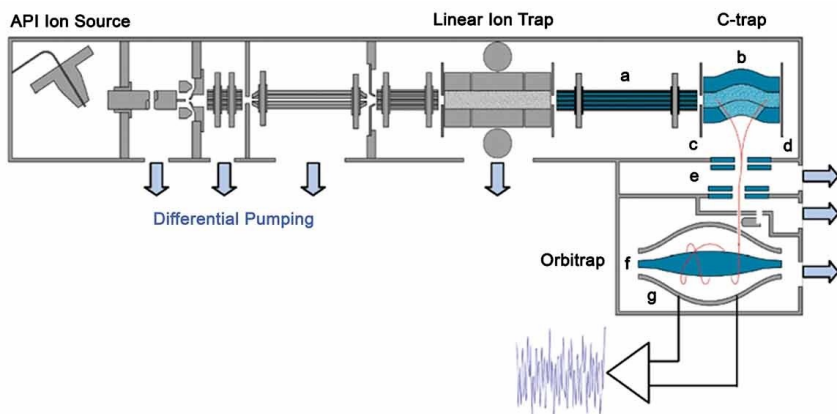
Figure 2.9 Schematic diagram of the LTQ orbitrap hybrid mass spectrometer. The linear ion trap is followed by (a) a transfer octapole, (b) C-trap, (c) gate electrode, (d) trap electrode, (e) ion optics, to the (f) inner Orbitrap electrode, (g) outer Orbitrap electrode. Reprinted with permission from ref. 105. copyright 2006, American Chemical Society

High-Throughput Single-Cell Mass Spectrometry Reveals Abnormal Lipid Metabolism in Pancreatic Ductal Adenocarcinoma

Even populations of clonal cells are heterogeneous, which requires high-throughput analysis methods with single-cell sensitivity. Here, we propose a rapid, label-free single-cell analytical method based on active capillary dielectric barrier discharge ionization mass spectrometry, which can analyze multiple metabolites in single cells at a rate of 38 cells/min. Multiple cell types (HEK-293T, PANC-1, CFPAC-1, H6c7, HeLa and iBAs) were discriminated successfully. We found evidence for abnormal lipid metabolism in pancreatic cancer cells. We also analyzed gene expression in a cancer genome atlas dataset and found that the mRNA level of a critical enzyme of lipid synthesis (ATP citrate lyase, ACLY) was upregulated in human pancreatic ductal adenocarcinoma (PDAC). Moreover, both an ACLY chemical inhibitor and a siRNA approach targeting ACLY could suppress the viability of PDAC cells. A significant reduction in lipid content in treated cells indicates that ACLY could be a potential target for treating pancreatic cancer.

3.1 Introduction

There are differences between individual cells, and even in the same cell population, cell heterogeneity exists.[106] Among the reasons are genetic differences and stochastic processes that occur in the cellular metabolism.[1] Since population measurements conceals information about the heterogeneity between cells, it is important to have sensitive analytical methods that afford the accurate chemical composition and contents of single cells. In addition, rare cell types including circulating tumor cells, cancer stem cells, invariant natural killer T cells, antigen-specific T cells, etc., play significant roles in pathogenic mechanisms, early diagnosis of tumor, and angiogenesis in cancer and other diseases.[107-108] In order to understand the results of these genetic differences and stochastic processes in individual cells more deeply and faithfully reflect the role that cells play in the regular operation of biological systems in terms of structure and function, it is necessary to analyze and study the composition and chemical content of cells at the single-cell level.

The concept of single-cell analysis has received widespread attention in recent years and has important applications.[109-111] Various single-cell omics technologies have emerged, including single-cell genomics, transcriptomics, proteomics and metabolomics. Also, Single-cell omics technologies have been applied to reveal metabolic heterogeneity of cells.[112] Compared to single-cell genomics, transcriptomics, and proteomics, single-cell metabolomics provides more rapid and dynamic information of cell function. For example, a deregulated metabolism is a hallmark of cancer cells.[113] Specifically, a dramatic increase of the de novo biosynthesis of fatty acids is generally observed in tumor cells. The increased capacity for generating lipids not only facilitates the formation of lipid bilayers but also enables the tumor cells to modulate their specific signaling transduction and cope with

oxidative stress.[114] For example, pancreatic ductal adenocarcinoma (PDAC) is one of the most lethal cancers with only around 9 % 5-year survival rate.[115] Accumulation of fatty acids was reported to correlate with PDAC initiation and metastasis in a PDAC mouse model,[116] indicating that lipid metabolism may be dysregulated in PDAC. Cancer cells are highly heterogeneous and exhibit phenotypic diversity, and the heterogeneity of cancer is closely related to the pathogenesis of cancer.[117] Single-cell analysis can accurately characterize the heterogeneity of cancer, thereby providing cancer treatment strategies.[118]

Single-cell analysis is challenging because intracellular biochemical reaction rates are fast, intracellular composition is very complex, the sample size is very small, some compounds are present only at the trace level, may have poor stability, and may be structurally similar. Studying the biological properties of single cells requires analytical techniques with high sensitivity, the ability to analyze ultra-small samples, good selectivity, and fast response. Since mass spectrometry has high sensitivity and selectivity, it holds great promise as an effective technique for single-cell metabolomics analysis. Numerous mass spectrometric techniques have been developed to elucidate the molecular profiles at the cellular level, including secondary ion mass spectrometry (SIMS),[26,32,119] matrix-assisted laser desorption/ionization mass spectrometry (MALDI-MS)[63,120-121] and electrospray ionization mass spectrometry (ESI-MS).[41,122-123] There are many ESI-based single-cell analytical methods, such as laser ablation-ESI-MS,[53] single probe ESI,[123] and T-probe ESI,[124] capillary electrophoresis-ESI-MS[125-126] and so on, however, most of them are low-throughput. Mass Cytometry (CyTOF) is a powerful plasma-based single-cell analysis tool that combines inductively coupled plasma mass spectrometry and flow cytometry.[127-128] CyTOF can simultaneously detect multiple cell surface protein markers at the single-cell level, but does not detect

low molecular weight metabolites. Recently, ESI-MS has been used as a flow cytometry detector to achieve high-throughput analysis of single-cell metabolites.[57,59] To widen the metabolome coverage, alternative ionization methods are useful.

Here we therefore explore the use of dielectric barrier discharge ionization (DBDI) for single-cell metabolomics. DBDI operates without auxiliary reagents and at atmospheric pressure, is easy to miniaturize, easy to operate, cheap and efficient, and has been used for the ionization of small molecular weight metabolites in recent years.[86,129-130] The DBDI-MS method introduced here has similar performance in terms of throughput, sensitivity, and the ability to distinguish cell types than the recently reported CyESI-MS methodology.[57,59] However, compared to other ionization methods, DBDI has some unique properties, for example, it is less affected by matrix effects and ion suppression than ESI,[92,131] it can analyze polar and nonpolar compounds simultaneously, and does not need vacuum condition.[86,132] Very recently, we have applied an ESI—DBDI combination source to single plant cell analysis.[35] Compared to ESI, a 2-fold increase in the number of visible metabolites was observed in the combination source.

In this work, we propose a high-throughput and label-free single-cell analytical method based on an active capillary DBDI source,[133] where the ionization takes place inside a capillary that is directly connected to the MS inlet. This dramatically increases robustness and ion transmission into the MS. The DBDI-MS platform (Figure 3.1) used in this work can analyze multiple metabolites in a single cell at the same time, including organic acids, carbonyl compounds, heterocyclic organic compounds and lipids, and can detect around 38 cells per minute. The proposed DBDI-MS platform was able to discriminate multiple cell types (293T, PANC-1, CFPAC-1, HeLa and iBAs) based on their metabolic profile. Moreover, the abnormal lipid

metabolism in pancreatic cancer cells was observed by using the DBDI-MS platform. As one of the major components involved in fatty acyl chain biosynthesis, the enzyme ATP citrate lyase (ACLY) is frequently upregulated in tumor cells.[134] Recently, it has been shown that ACLY is critical for the initiation of PDAC in pancreatic cancer animal model, as ACLY ablation attenuated the acinar-to-ductal metaplasia (ADM).[135] However, the expression levels and potential role of ACLY were not fully elucidated in established PDAC. Here, we propose that the expression levels of ACLY are related to the abnormal lipid metabolism in established PDAC. The DBDI-MS platform specifically detected the redistribution of lipids in PDAC cells after treating them with different dosages of specific ACLY inhibitor but not in PDAC cells treated with a canonical anticancer drug (gemcitabine) or DMSO. Furthermore, both specific chemical inhibitor or siRNA approach targeting ACLY could reduce the cell viability in PDAC cells, indicating the tumor-promoting effect of ACLY in established PDAC cells.
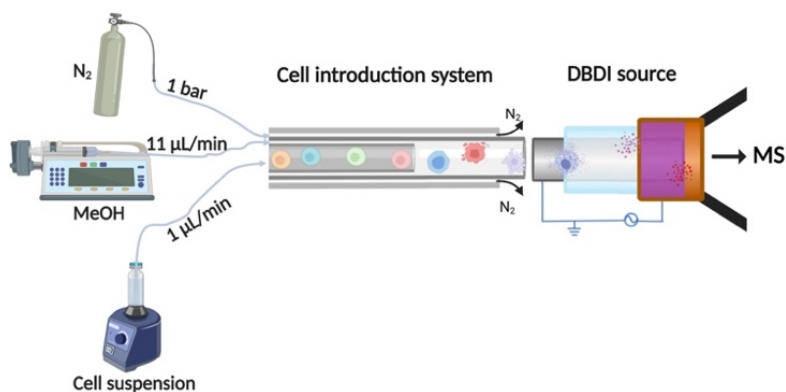
Figure 3.1. Schematic of the DBDI-MS platform. Cells are lysed by MeOH in the cell introduction system, and the metabolites in the cells are ionized by DBDI source.

3.2 Experimental Section

3.2.1 Chemicals, Materials and cells

Methanol (99.9%), ammonium acetate, ammonium formate (>99.0%), gemcitabine, SB204990 and dimethylsulfoxide (DMSO) were purchased from Sigma-Aldrich Chemie GmbH (Buchs, Switzerland). Phosphate Buffer Saline (PBS) were purchased from Thermo Fisher Scientific (Buchs, Switzerland). Fused silica capillary tubes were purchased from Polymicro Technologies (BGB Analytik AG, Switzerland). HEK-293T, HeLa, PANC-1, CFPAC-1 and preadipocyte were purchased from ATCC. H6c7 was purchased from Kerafast.

3.2.2 Cell culture

CFPAC-1 was maintained in RPMI-1640 medium supplemented with 10% (v/v) fetal bovine serum and 1% Penicillin-Streptomycin (P/S). PANC-1, HEK-293T and HeLa were grown in DMEM with 10% (v/v) fetal bovine serum and 1% Penicillin-Streptomycin (P/S). H6c7 was maintained in a keratinocyte serum-free medium following the manufacturer's instructions. Immortalized brown adipocytes(iBAs) were derived from the differentiation of preadipocytes. Preadipocytes were cultured in DMEM with 10% fetal calf serum (FCS) and 1% P/S. In order to induce adipogenic differentiation, preadipocytes were grown to confluence on collagen-coated tissue culture plates and maintained for another 2 days. By adding 0.25 mM IBMX, 0.5 μM dexamethasone, 10 nM insulin, 62.5 μM indomethacin, and 0.5 nM T3 in full medium, preadipocytes were induced to differentiate into immortalized brown preadipocytes. After 24 h, the medium was exchanged for full medium plus 20 nM insulin and 1 nM T3. This medium was changed

every 2 days. Cells were analysis after 5 days of induction of differentiation. All cells were grown at 37°C in the humidified incubator (Thermo Fisher Scientific) with 5% CO_2.

3.2.3 Drug treatment of PANC-1 and CFPAC-1 cells

PANC-1 and CFPAC-1 cells plated in a culture dish and maintained with normal full medium until the cell confluent reaches 80%. Gemcitabine (sigma, cat# G6423) and SB204990 (sigma, cat# SML2829) were dissolved in DMSO (Sigma, cat# D4540), diluted into full medium at the indicated concentration and then incubated with PDAC cells for 48 hours.

3.2.4 Cancer Genome Atlas (TCGA) dataset analysis

ACLY expression data of normal pancreatic tissues (GTEx; n = 167) and pancreatic ductal adenocarcinoma (TCGA-PDCA; n = 178) were downloaded from UNSC Xena (https://xena.ucsc.edu/). Differential expression analysis was performed using DESeq2. Gene Set Enrichment Analysis (GSEA v3.0) of GO biological processes was performed on normalized counts (PMID: 16199517).

3.2.5 qPCR

Total RNA was isolated with Trizol following the manufacturer's protocol (Sigma, Cat# T9424). The resulting RNA was treated with DNase I (Thermofisher Scientific, Cat# AM1906). Then the RNA was reverse transcribed using High-Capacity cDNA Reverse Transcription Kit (Thermo Fisher Scientific, Cat# 4368813) by using random primers. Quantitative PCR was performed by KAPA SYBR FAST qPCR assay (Sigma, Cat# KK4611) in an LC480 II Lightcycler

(Roche). Results were normalized to human *36B4* mRNA levels. Primers: human ACLY forward (5'-3'): GATTTTGCGGGGTTCGTCG, human ACLY reverse (5'-3'): GCTTGACTACCAAGTTCTGGC. Human *36B4* forward (5'-3'): GGCGCCTACTTCTTCTCCTT. Human *36B4* reverse (5'-3'): TCGTAAATCATGGCCTGCAC.

3.2.6 Immunoblot (IB)

PDAC or H6c7 cells were lysed in RIPA buffer (150 mM sodium chloride, 50 mM Tris-HCl pH=7.4, 0.1% SDS, 1 mM EDTA, 1% NP-40, 0.5% sodium deoxycholate) freshly supplied with protease inhibitors cocktail (Roche, cat#11873580001) and PhosSTOP (Roche, cat# 04906837001). The protein concentration was determined using the bradford protein assay (abcam, cat# bfu05l). The same amount of proteins was subjected to 10% SDS-PAGE analysis. The immune complex was detected by the ECL kit (Thermo Scientific). Phos-AKT (S473, cell signalling, cat#4060S), total AKT (Cell signalling, cat# 9272S), phos-p70 S6K (T389, Cell signalling, cat#9206S), total p70 S6K (Cell signalling, cat#9202S) and GAPDH (sigma, cat# G9545) were diluted at 1:1000 in 1x TBS buffer (pH:7.6). The amounts of protein were quantified by Image J software.

3.2.7 Determination of cell viability by MTT assay

Cell viability was determined by MTT [3-(4,5-dimethyl-2-thiazolyl)-2,5-diphenyl-2H-tetrazoliumbromid] (Sigma, Cat# M5655) assay after transfecting cells with siRNA control (Horizon, cat# D-001810-10-05) or siRNA-ACLY (Horizon, cat# L-004915-00-0005) for 72 hours. Briefly, MTT solution in 1x PBS was added to each well of 96 well-plate at the final concentration of 0.5 mg/mL.

The plate was protected from light and incubated for 3 hours at 37 °C. The medium was then aspirated and the dark-blue formazan was dissolved with DMSO. Optical density was measured with a spectrometer at 490 nm. The raw luminescence data were normalized to the siRNA control.

3.2.8 Preparation of Cell Suspensions

Before starting the experiment, DMEM was removed by centrifugation (1000 rpm, 4 minutes), and the cells were resuspended in PBS. Then the cells were centrifuged again (1000 rpm, 4 minutes) to remove PBS, and resuspended in 140 mM NH_4COOH solution. The effect of solvent of cells has been optimized (Figure S3.2).

3.2.9 Cell Introduction System

The cell introduction setup was placed 2 mm in front of the DBDI source. As shown in Figure S3.1, the main parts of the cell introduction setup were 3 coaxial capillaries, two of which are fused silica capillaries and one is a metal capillary. The inner capillary (193 μm O.D., 75 μm I.D.) was used to introduce cell suspension from a sample vial. The intermediate capillary (350 μm O.D., 250 μm I.D.) was used to transport MeOH which worked as extract fluid. The exit end of the inner capillary was 4 mm shorter than the intermediate one (after optimization, Figure S3.3). When cells flowed out of the inner capillary and contacted with MeOH in the intermediate capillary, the cell was lysed and metabolites of the cells were extracted by MeOH online. Nitrogen, carried in the outer metal capillary, was used as auxiliary gas to help solvent evaporate and cells fly into the DBDI.

3.2.10 Ionization Source

An active capillary plasma ionization source (based on a dielectric barrier discharge ionization) was used to ionize single cells in this study.[133] As shown in Figure S3.1, the DBDI has two electrodes, an outer electrode (high voltage, copper, ID: 1.55 mm, surrounding the glass capillary) and an inner electrode (ground, stainless steel, ID: 0.6 mm and OD: 1.0 mm). They are separated by a glass capillary which is the dielectric barrier. When a high AC voltage (2.6 kVpp, 47 kHz) is applied to the outer electrode, the plasma will be ignited inside the capillary. The voltage of DBDI has been optimized (Figure S3.4).

3.2.11 Procedure for DBDI-MS Single Cell Analysis

The DBDI-MS was composed of three main parts, including a cell introduction system, a DBDI source, and an LTQ Orbitrap (Figure S3.1). Before cell introduction, the inner capillary was thoroughly rinsed with a 140 mM NH_4COOH aqueous solution, and the intermediate capillary was thoroughly rinsed with MeOH until the background total ion chromatogram (TIC) is stable. The freshly prepared cell suspension was introduced into the inner capillary at a flow rate of 1 µL/min, MeOH was introduced into the intermediate capillary at a flow rate of 11 µL/min. Then the cell contents were ionized by DBDI and detected by a high-resolution Orbitrap mass spectrometer. After each measurement, all capillaries should be flushed with MeOH for 10 minutes at a flow rate of 7 µL/min. The effects of lysis/extraction fluid on single-cell analysis and MeOH flow rate have been optimized (Figure S3.5 and Figure S3.6).

3.2.12 Mass Spectrometry

Mass spectra were acquired in positive ion mode, with an LTQ Orbitrap mass spectrometer (Thermo Fischer Scientific, San Jose, U.S.A.), in fullscan mode at a resolution of 30,000 FWHM (at m/z 400) with a mass tolerance specified to be < 10 ppm. The mass-to-charge range was set to 100–1000, capillary voltage is 50 V, tube lens voltage is 120 V, capillary temperature is 320°C, AGC target = 10^6. Mass spectra were acquired using 1 microscans and a maximum injection time of 10 ms.

3.2.13 Data analysis

The MS raw data generated from the mass spectrometer was recorded with Xcalibur™ version 2.2 software (Thermo Fisher Scientific, San Jose, U.S.A.). The MSConvert software (ProteoWizard, v3.0)[136] was used to convert MS raw data (.raw) to mzXML format. The converted mzXML format file is imported into Matlab (R2019b version, MathWorks, Natick, MA), and preprocessed using self-developed Matlab code. In short, the peaks were selected from the overall averaged spectrum of the spectra obtained during the measurement. The picked peaks were used to centroid the collected data, and then a .csv file containing the peak intensity of each scan was generated for each collected MS data set.

PC(34:1) and PC(32:1) were selected as the markers for the successful detection of single cells, thereby extracting all ion signals related to single cells. Ion signals related to single cells with a signal-to-noise ratio (S/N ratio) greater than 3 and occurrence frequency greater than 30% in all cells were kept for further analysis. These selected target ions and their intensity in each pulse peak represented the metabolic profile of each single cell. Statistical analysis was conduction using R (v4.0.2). Signal intensities were

normalized against total ion count and then log 2 transformed. Based on the acquired metabolites information, principal component analysis (PCA) analysis and t-distributed stochastic neighbor embedding (t-SNE) were used for the visualization of single cells, heat maps were used to show the expression levels of metabolites in different cells. The two-tailed student's t-test was used to evaluate the statistical significance level (P-value) of single-cell metabolism information between different cell lines, which was displayed in the volcano plots. Violin plots were used to show the changes in lipids distribution of cells after different treatments.

The peak assignments were done by comparing the observed mass with the theoretical mass in the online databases, including Human Metabolome Database (http://www.hmdb.ca/), LIPID MAPS (http://www.lipidmaps.org) and METLIN metabolite database (https://metlin.scripps.edu/).

3.3 Results and Discussion

3.3.1 Feasibility of single cell DBDI-MS

Since DBDI-MS has not previously been used for single-cell analysis, we conducted preliminary experiments to demonstrate its feasibility. A PANC-1 cell suspension (at a flow rate of 1 µL/min) and MeOH (at a flow rate of 11 µL/min) were introduced into the DBDI source via a home-built cell introduction system (Figure S3.1). As presented in Figure 3.2a, signal pulses appeared in the total ion chromatogram (TIC) when the DBDI source was on, but when it was off, even if the cell suspension was introduced into the DBDI source, there was no signal in the TIC. In order to demonstrate that the detected signals came from cells rather than from other substances, the peaks at m/z 760.5851 (assigned to glycerophosphocholine (PC)

34:1) and m/z 732.5538 (assigned to PC 32:1), which are components of cell membranes, were chosen as markers of cells passing through the DBDI. It can be seen from Figures 3.2b and c that the positions and frequency of m/z 760.5851 and m/z 732.5538 peaks matched with the TIC. Figures 3.2d and 3.2e display that with the DBDI switched on, there were obvious lipid peaks in the m/z 700-m/z 900 region, but there were no lipid peaks when the DBDI was turned off. The results suggest that DBDI-MS is able to detect single cells.
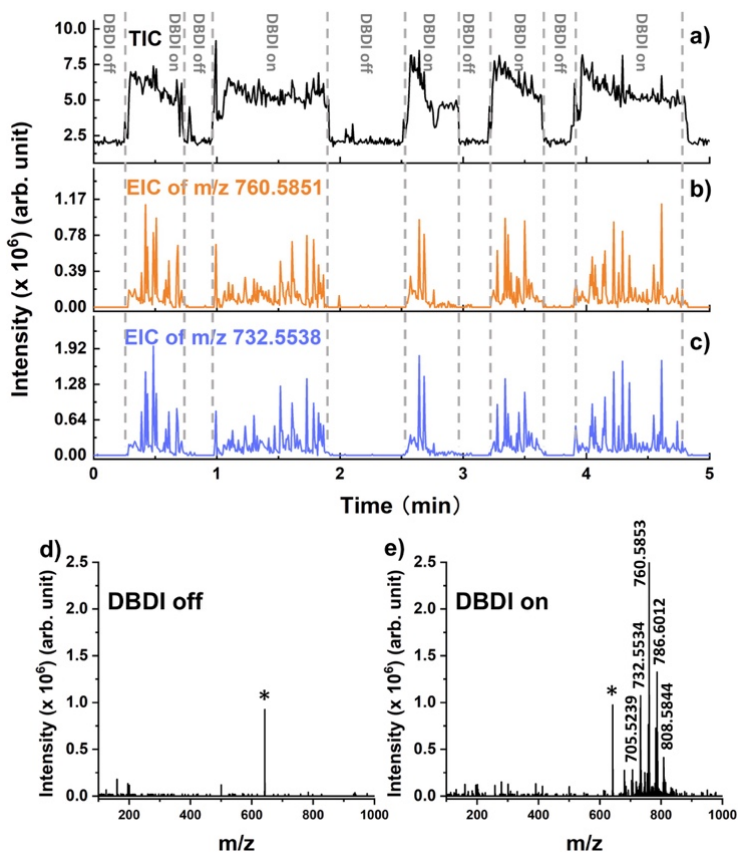
Figure 3.2. PANC-1 cell analyzed by DBDI-MS. (a) Total ion chromatogram (TIC), (b) extracted ion chromatogram (EIC) of m/z 760.5851 and (c) EIC of m/z 732.5538 acquired in DBDI on and off modes. (d) mass spectrum in DBDI off mode, and (e) mass spectrum in DBDI on mode. The asterisk (*) indicates electronic noise in the spectra.

The optimization of experimental conditions for single-cell analysis are described in detail in section 2 of the SI (Figures S3.2-S3.6).

To further evaluate the performance of DBDI-MS, analysis of different cell suspensions was carried out (in section 3 of the SI, Figures S3.7-S3.9), including PANC-1 cells, CFPAC-1 and H6c7 cells. In order to further prove that the results obtained were from single cells instead of cell clusters, the cell suspension was sequentially diluted with ammonium formate to 5×10^3, 1×10^4, 2×10^4, 3×10^4, 4×10^4, 5×10^4 cells/mL and then measured by DBDI-MS. To facilitate the calculation of cell concentration, the flow rate of the cell suspension during the entire experiment was set to 1 μL/min. The results are summarized in Table 3.1, Table S3.1 and Table S3.2. As shown in Table 3.1, Table S3.1 and Table S3.2, the number of peaks per minute matched well with the cell concentration, and the number of detected cells were essentially the same as the calculated number of cells, which indicates that most cells were monodisperse and detected separately. However, when the cell concentration was $\geq 5 \times 10^4$ cells/mL, we found that there were overlaps between the pulsed signals, and even the capillary used to introduce the cells was sometimes blocked. Therefore, the cell concentration used during the entire experiment was controlled to <5×10^4 cells/mL. The above results prove that our method is high-throughput and able to detect metabolites with single-cell resolution.

44

Table 3.1. Comparison between the calculated and the detected number of PANC-1 cells at different densities of the cell suspension.

Cell density, cells mL^{-1}	Calculated cell number [min]	Detected cell number [min]					Average detected cell number [min]
5 x 10^3	5	3	6	6	4	4	4.6
1 x 10^4	10	8	8	9	9	11	9
2 x 10^4	20	19	23	19	18	17	19.2
3 x 10^4	30	29	30	26	27	24	27.2
4 x 10^4	40	39	37	38	36	38	37.6

3.3.2 Metabolite Profiling and Discrimination of Cell Type.

In positive ion mode, approximately 179 peaks indicating metabolites in the m/z range between 100–1000 were detect in PANC-1 cells. These metabolites can be classified as organic acids, carbonyl compounds, heterocyclic organic compounds and lipids.

The details of the detected metabolite classification are shown in Table S3.3. Because there is only limited cell lysis during the brief contact with the MeOH flow (see Figure S3.1), the extracted metabolites originate mainly from the cell membranes, i.e., most of them are lipids. Since there are lots of reactive species in the plasma, different product ions were generated. In addition to common product ions such as $[M+H]^+$, $[M+Na]^+$, there were also $[M+H-H_2O]^+$, $[M+H-2\,H_2O]^+$ and $[M+NH_4]^+$ produced. The tandem MS information can be found in Figure S3.10.

Cell metabolites are potential biomarkers to distinguish cells. To test if our DBDI-MS could be applied to profile cell types, we measured five different kinds of cells, 293T, PANC-1, CFPAC-1, HeLa and iBAs by DBDI-MS. After obtaining metabolic information,

principal component analysis (PCA) (Figure 3.3a) and t-distributed stochastic neighbor embedding (t-SNE) (Figure S3.11) were used to separate cell types, which showed that single-cell metabolite information could successfully distinguish cell types. The specific details of the analysis for the metabolic profiles are described in section 1 of the SI. The heat map (Figure 3.3b) shows the relative intensities of metabolite ions from each cell. This information indicates that the types of single-cell metabolite profiles between different cells are significantly different, and single-cell metabolic information is adequate for cell discrimination.

All the above results showed that the DBDI-MS platform is sensitive, accurate and specific to detect a variety of metabolites.
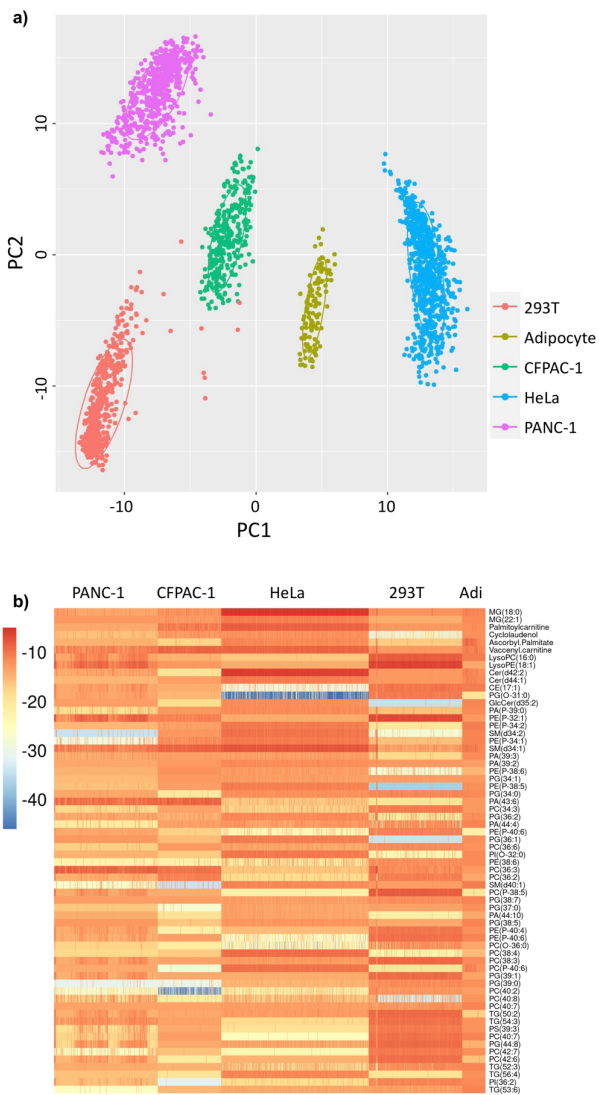
Figure 3.3. Discrimination of cells by DBDI-MS platform. (a) Principal component analysis (PCA) of five cell types. (b) Heatmap of the single-cell metabolite in five cell types.

3.3.3 Single-Cell DBDI-MS Metabolic Profile Identify Deregulated Lipid Metabolism in PDAC Cells

Lipid metabolism is critical for cancer development, but the study on the level of lipid metabolism in PDAC cells is still very limited. Thus, we compared the metabolites of PDAC cells and ductal epithelial cells H6c7. By comparing the mass spectral profiles of PANC-1, CFPAC-1 and H6c7 (Figures 3.4a, b and c), we found that most of the detected compounds are phospholipids. Phospholipids are the main components of cell membranes, and their content in cells is high. In the lower mass range ($m/z<400$), PANC-1 and CFPAC-1 contained hexanoylcarnitine, which was not detectable in H6c7. In the higher mass range ($m/z>400$), the most abundant lipids in PANC-1, CFPAC-1 and H6c7 were PC(32:1), PC(34:1), PC(36:2) and PC(38:5), but their distribution was slightly different. As shown in Figures 3.4a, b, c and S4.12, in PANC-1 and CFPAC-1, PC (34:1) is the most abundant lipid, its intensity at m/z 760.58 being higher than that of PC (36:2) (m/z 786.60). However, in H6c7, PC (36:2) is the most abundant lipid, with an intensity of PC (34:1) (m/z 760.58) lower than that of PC (36:2) (m/z 786.60). As shown in Figures 3d, e, f and g, the content of PC(32:1), PC(34:1), PC(36:2) and PC(38:5) is higher in pancreatic cancer cell types (PANC-1 and CFPAC-1) than that in pancreatic ductal epithelial cells (H6c7). In addition to these lipids that occur in all three types, each of the cell also contained some unique lipids. For example, PC (O-36:1) and PS (40:3) were only detected in CFPAC-1, and TG (48:2) was only detected in H6c7.

The heat map in Figure S3.13 shows the normalized intensities of assigned metabolites from each cell, and significant differences are seen for some metabolites. In the volcano plots, differentially expressed features in the two pancreatic cancer cell lines (PANC-1, CFPAC-1) and the corresponding normal cell line (H6c7) are visualized. According to Figure 3.4h, several amino acids and lipids,

for example, *N*-lactoyl-methionine (m/z 239.1061, [M+NH$_4$]$^+$), hexanoylcarnitine (m/z 260.1856, [*M*+H]$^+$), MG(18:0) (m/z 381.2981, [M+Na]$^+$) and PS(30:2) (m/z 686.4395, [M+H−H$_2$O]$^+$) exhibited clear statistical differences between PANC-1 and H6c7 cells. As shown in Figure 3.4i, the metabolites with statistical differences between CFPAC-1 and H6c7 cells were also amino acids and lipids, for example, PC (34:1) (m/z 782.5660, [M+Na]$^+$), *N*-lactoyl-methionine (m/z 239.1061, [M+NH$_4$]$^+$) and hexanoylcarnitine (m/z 260.1856, [*M*+H]$^+$).

To further estimate the potential of DBDI-MS in clinical applications, we carried out an analysis of a mixed cell suspension composed of PANC-1, CFPAC-1 and H6c7 cells, to simulate potentially cancerous tissues of PDAC patients. Based on their characteristic single-cell metabolite profiles acquired by DBDI-MS, DBDI-MS can specifically and high-throughput identify different cell types in a cell mixture (Figure 3.4j) PANC-1 cells, CFPAC-1 cells, H6c7 cells and the cell mixture can be separated by t-SNE (Figure 3.4k), and cells from the mixture each fall into a specific group, which makes it possible to blindly identify cells from a mixture.

It can be seen that the types, content and distribution of lipids in pancreatic cancer cells and normal ductal cells are different, and that the abnormal lipid metabolism in pancreatic cancer cells can be clearly observed by DBDI-MS.
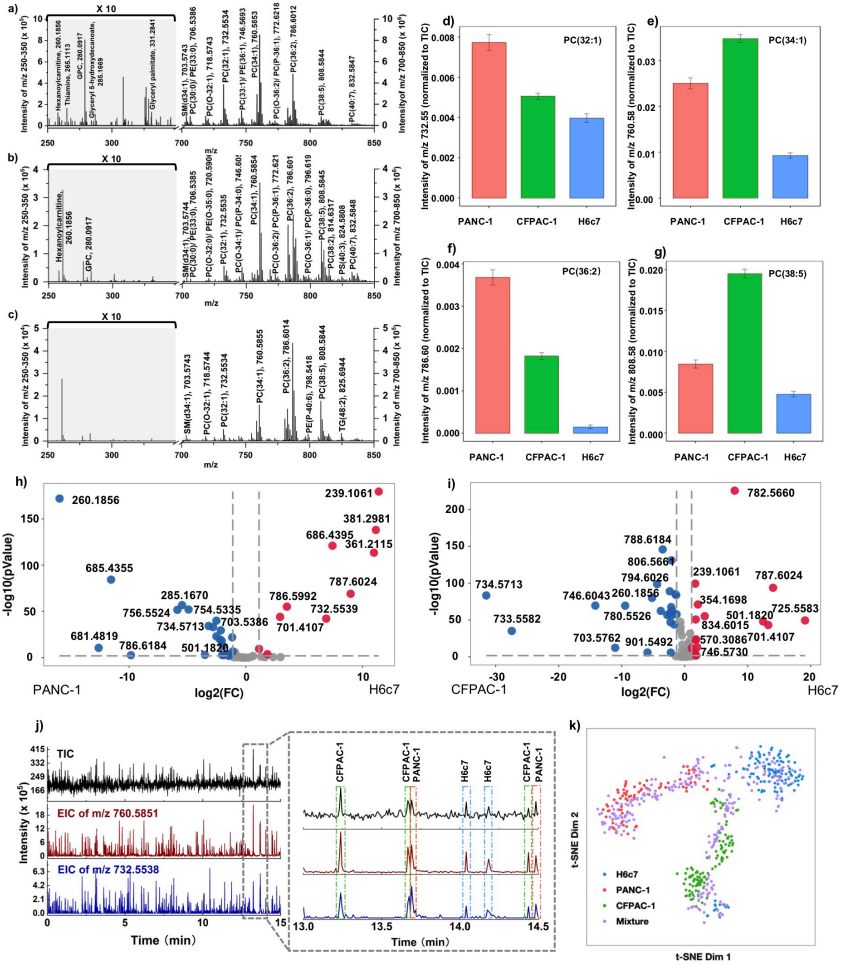
Figure 3.4. Assignment of cellular metabolites and discrimination of PDAC and H6c7 cells. (a) Typical PANC-1 single-cell mass spectrum. (b) Typical CFPAC-1 single-cell mass spectrum. (c) Typical H6c7 single-cell mass spectrum. (d-g) Normalized intensity of PC(32:1), PC(34:1), PC(36:2) and PC(38:5) in PANC-1, CFPAC-1 and H6c7 cells. (h) Volcano plot of the correlations between the P-values and fold changes (FD) for the metabolite signals in PANC-1 and H6c7 cells. (i) Volcano plot of the correlations between the P-values and fold changes (FD) for the metabolite signals in CFPAC-1 and H6c7 cells. (j) Total ion chromatogram (TIC),

extracted ion chromatogram (EIC) of m/z 760.5851 and EIC of m/z 732.5538 of mixed cell suspension (1 × 104 cells/mL) composed of PANC-1, CFPAC-1 and H6c7. (k) Distributed stochastic neighbor embedding (t-SNE) analysis of PANC-1, CFPAC-1, H6c7 and mixed cell suspension composed of PANC-1, CFPAC-1 and H6c7.

3.3.4 Deregulated ACLY Levels in PDAC

In order to investigate why lipid metabolism was abnormal in PDAC cells, we monitored the expression levels of ACLY which is the critical rate-limiting enzyme for lipid synthesis, in one human TCGA dataset consists of 167 normal and 179 PDAC patients.[137] The mRNA level of ACLY increased around 1.4 fold in PDAC (Figure 3.5a). We further confirmed the upregulated ACLY mRNA levels in PDAC cells by qPCR (Figure 3.5b). Since ACLY is one of the critical enzymes for acetyl-CoA and lipid acids synthesis, we also analyzed the acetyl-CoA and lipid metabolism biological pathways in the same TCGA dataset by Gene set Enrichment Analysis (GSEA). Interestingly, we found that the genes involved in the acetyl-CoA metabolic process and lipid homeostasis were enriched in human PDAC samples (Figures S3.14a and b). Combined with our in vitro data (Figure 3.4), we conclude that the ACLY levels and lipid metabolism is deregulated in human PDAC. Recent studies revealed that PI3K-AKT and mTORC1 signaling pathways control the level of ACLY.[135,138] We thus hypothesized that the upregulated ACLY in PDAC cells may due to the deregulated PI3K-AKT and mTORC1 pathways. To this end, we monitored the protein levels of the key members of both signalling pathways including: activated form of AKT (phosphorlation of AKT at ser473 site), total AKT, activated p70 S6K (phosphorlation of p70 S6K at T389 site) and total p70 S6K in PDAC and H6C7 cells by immunoblotting. Indeed, we found both signalling pathways are activated in PDAC cells evidenced by the upregulation of phos-AKT(Ser473)/total AKT and phos-p70 S6K(T389)/total p70 S6K

levels compared to H6C7 cells (Figures 3.5c–e), indicating that the deregulated PI3K/AKT and mTORC1 pathways may contribute to the high levels of ACLY in PDAC cells.
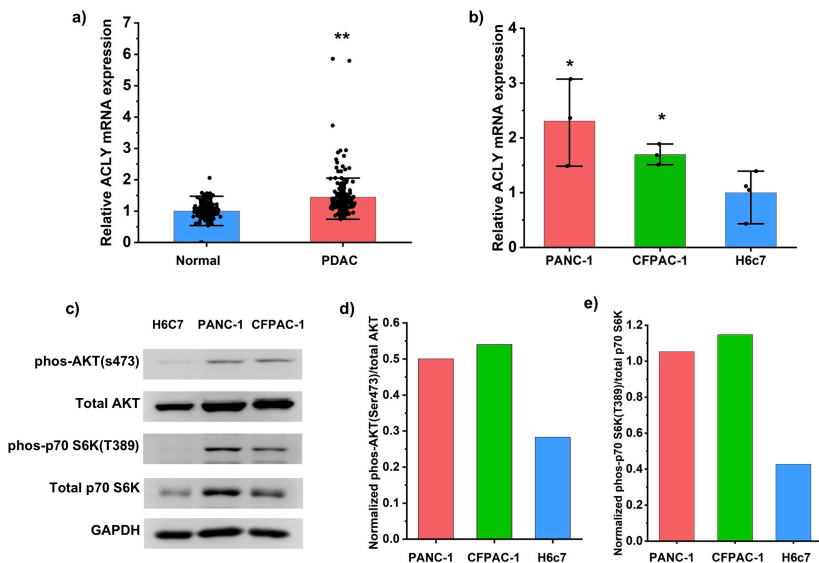
Figure 3.5. Deregulated ACLY levels in PDAC. (a) Relative ACLY mRNA levels in human normal and PDAC pancreatic samples. Mean ± SD (n=167 in normal and n=179 in PDAC). **, p<0.01. (b) Relative ACLY mRNA levels in PANC-1, CFPAC-1 and H6c7 cells. Mean ± SD (n=3). *, p<0.05. (c) Immunoblot (IB) analysis of the total cell lysate derived from PANC-1, CFPAC-1 and H6c7 cells. GAPDH was used as protein loading control. (d-e) Bar plots represent of the quantification of IB described in (c). qPCR and Immunoblot analysis were performed at the cell population level.

3.3.5 ACLY Inhibition-Induced Lipid Redistribution Was Specifically Detected by the DBDI-MS Platform

Since the biological evidence demonstrates that ACLY is abundant in human PDAC samples, we investigated the effect of an ACLY

chemical inhibitor on pancreatic cancer cells using the DBDI-MS platform. As shown in Figures 3.6a–g and S3.15a–g, PC(32:1), PC(34:1) and PC(36:2) are the three predominant lipids in PANC-1 and CFPAC-1. When PANC-1 and CFPAC-1 were treated with gemcitabine or DMSO, the intensity of PC(36:2) is higher than the intensity of PC(32:1), and the intensity ratio of PC(32:1)/PC(36:2) (m/z 732.55/786.60) is similar. However, when PANC-1 and CFPAC-1 were treated with SB-204990, the intensity of PC(36:2) became lower than intensity of PC(32:1), and the intensity ratio of PC(32:1)/PC(36:2) (m/z 732.55/786.60) was increased. Figures 3.6f and S3.15f show that compared with PANC-1 and CFPAC-1 cells treated with DMSO, the contents of PC(32:1), PC(34:1) and PC(36:2) in the cells treated with different concentrations of gemcitabine did not change significantly, but the contents of PC(32:1), PC(34:1) and PC(36:2) in PANC-1 and CFPAC-1 treated with different concentration of SB-204990 were significantly reduced, when the concentration of SB-204990 increased, the contents of PC(32:1), PC(34:1) and PC(36:2) decreased. The t-SNE clustering results in Figures 3.6h and S3.15h show heterogeneity of PANC-1 and CFPAC-1 after different treatments can be observed. PANC-1 and CFPAC-1 treated with SB-204990 were separated more significantly than PANC-1 and CFPAC-1 treated with gemcitabine or DMSO.
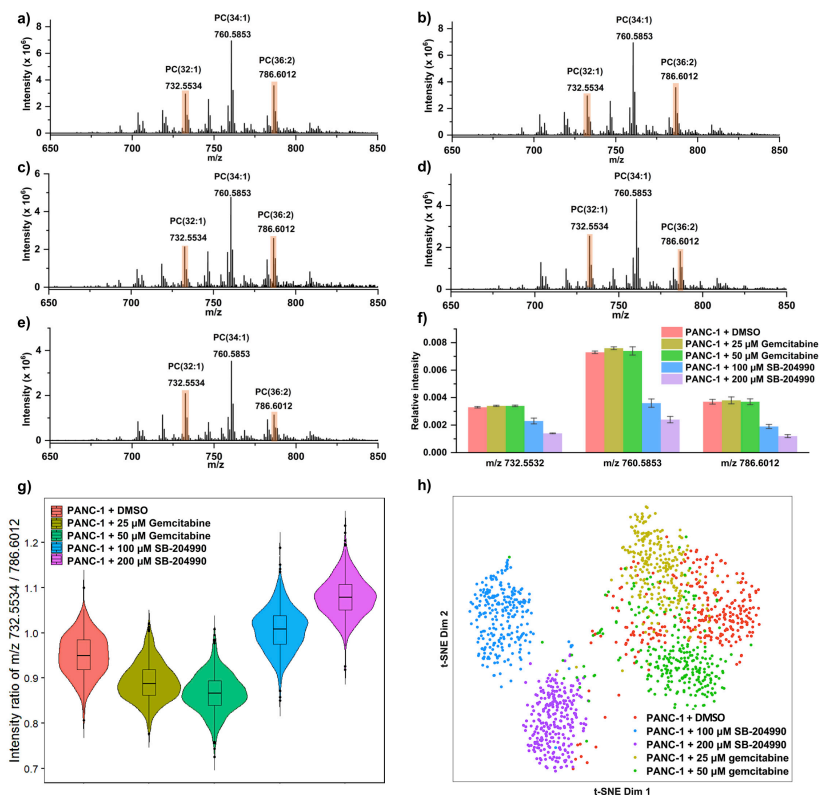
Figure 3.6. PANC-1 with different treatments. (a) Representative mass spectrum of PANC-1 treated with DMSO. (b) Representative mass spectrum of PANC-1 treated with 25 μM Gemcitabine. (c) Representative mass spectrum of PANC-1 treated with 50 μM Gemcitabine. (d) Representative mass spectrum of PANC-1 treated with 100 μM SB-204990. (e) Representative mass spectrum of PANC-1 treated with 200 μM SB-204990. (f) Bar plots for the changes of lipid contents after different treatments. (g)Violin plots for comparing the intensity ratio of PC(32:1)/PC(36:2) (m/z 732.55/786.60) in PANC-1 with different treatments. (h) t-SNE analysis of PANC-1 with different treatments.

Thus, the above results show that the lipid metabolism in PDAC cells could be reversed by ACLY inhibition, which further supports

the notion that deregulated ACLY contributes to the abundance of lipids in PDAC cells. Moreover, the modifications induced by ACLY inhibition could be specifically detected by our sensitive single-cell DBDI-MS platform. Because DBDI-MS shows high sensitivity and high specificity at the level of cell lines, it has the potential to classify the cells in clinical cancer tissues, identify the characteristic metabolites of different cancer types, and distinguish cancer subtypes.

3.3.6 ACLY May Serve as a Novel Target for Established PDAC

The above findings revealed by our new DBDI platform inspired us to explore whether targeting ACLY could be beneficial for PDAC therapy. As a primitive ACLY inhibitor, SB-204990 displays tumor-suppressive effects in multiple tumors both in vitro and in vivo.[139]

To this end, we first treated PANC-1 and CFPAC-1 cells with the ACLY inhibitor SB-204990 and found a dosage dependent suppression of cell viability by SB-204990 in PDAC cells (Figures 3.7a and d). Accordingly, after transfecting PDAC cells with siRNA targeting ACLY (Figures 3.7b and e), we also found a significant reduction of cell viability (Figures 3.7c and f). Thus both chemical inhibitors or genetic approaches targeting ACLY could reduce PDAC cell viability, suggesting that ACLY could be a promising target in established PDAC.
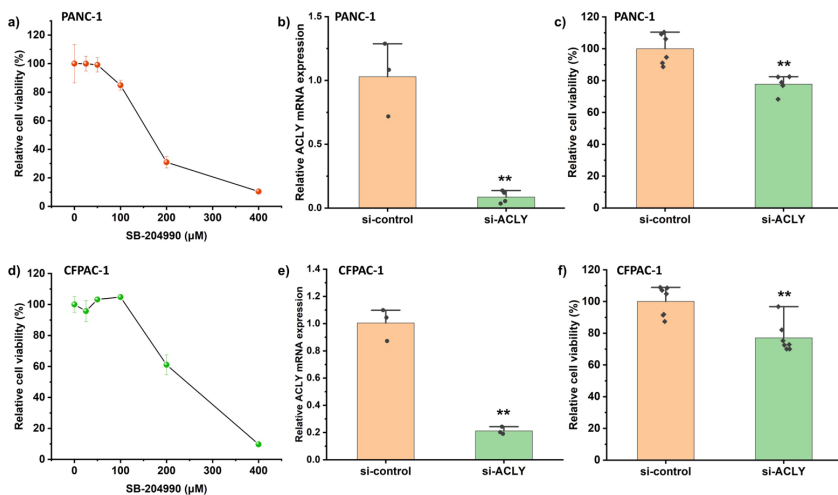
Figure 3.7. Chemical inhibition or siRNA approach targeting ACLY repress PDAC cell viability at the population level. (a,d) Relative cell viability detected by MTT assay in PANC-1 and CFPAC-1 cells treated with indicated concentration of SB-204990 and DMSO for 48 hours. Mean ± SD (n=4-8). (b,e) Relative ACLY mRNA expression in PANC -1 and CFPAC-1 cells transfected with si-control or si-Acly oligos. Mean ± SD (n=3-4). **, p<0.01, unpaired t-test. (e,f) Relative cell viability detected by MTT assay in PANC-1 and CFPAC-1 cells transfected with si-control or si-Acly oligos for 72 hours. Mean ± SD (n=6). **, p<0.01, unpaired t-test.

3.4 Conclusions

In conclusion, a high-throughput, label-free and sensitive DBDI-MS platform was developed for the analysis of single-cell metabolites, which achieved a throughput of approximately 38 cells per minute. The DBDI-MS platform is able to discriminate different cell types successfully based on their cellular metabolites. Compared with bulk cell analysis, our single-cell DBDI-MS platform can separate different cells from mixed cell suspensions according to its characteristic single-cell metabolite profile, and classify each type of

cell into a specific group, which may help detect lipid metabolism in clinical cancer tissues.

Since the DBDI-MS platform found that abnormal lipid metabolism occurs in pancreatic cancer cells, a series of biological methods were used to analyze the expression levels of ACLY and the activation of related biological pathways in the TCGA dataset and PDAC cells. We indeed found the deregulated ACLY, acetyl-CoA synthesis and lipid homeostasis pathways in PDAC. We further identified deregulated PI3K/AKT and mTORC1 pathways may promote the ACLY expression in PDAC.

By treating PDAC cells with different dosages of specific ACLY inhibitor, the redistribution of lipids in PDAC cells was observed by the DBDI-MS platform. Further biological experiments also demonstrated that both ACLY inhibitor or genetic approach that targeting ACLY could repress cell viability of PDAC cells. These results prove the high sensitivity of our DBDI-MS platform and also confirmed that ACLY indeed contributes to the lipid metabolism in PDAC cells, indicating ACLY may serve as a novel therapeutic target in PDAC.

Thus, our DBDI-MS platform may have the potential to serve as a new generation of mass cytometry and contribute to biological and clinical research.

3.5 Supporting information

3.5.1 The specific configuration and operation details of DBDI mass cytometry platform
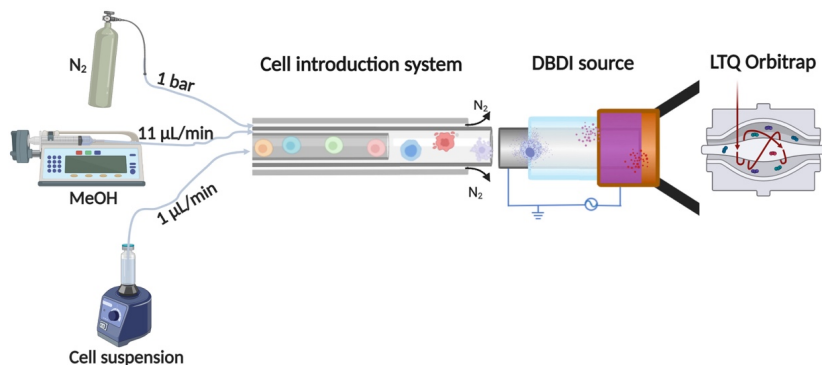
Figure S3.1. The specific configuration and operation details of DBDI mass cytometry platform, including: cell introduction system, a DBDI source, and an LTQ Orbitrap.

3.5.2 Optimization of experimental conditions for single-cell analysis

3.5.2.1 The effect of the solvent for cell suspensions on single-cell analysis

In order to maintain the structure of cells during the cell introduction process, the cells should be kept in an isotonic saline solution of neutral pH. As can be seen from Figure S3.2, different solvents had different effects on the intensity of cell metabolites and the number of cells detected per minute. Since the detected PC (34:1) had the highest intensity when the cells are in ammonium formate solution, and the number of cells detected per minute was also more than that detected in PBS and ammonium acetate, ammonium formate was thus selected as the solvent remain cell activity and integrity during further experiments.
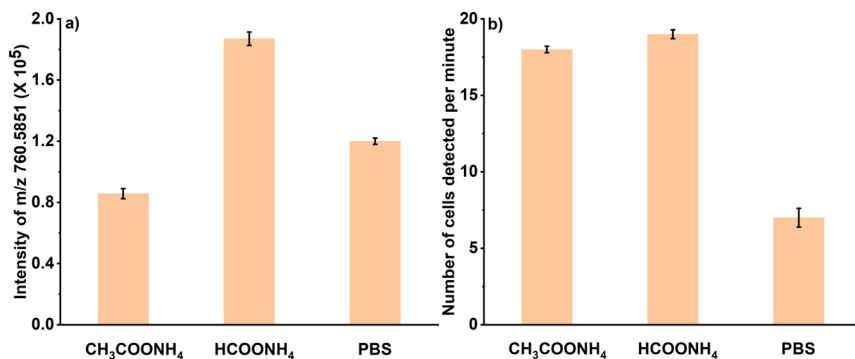
Figure S3.2. The effect of the solvent for cell suspensions on single cell analysis (PANC-1 cell suspension was chosen as the example). (a) Extraction efficiency of PC (34:1), (b) number of cells detected per minute.

3.5.2.2 Effect of the distance of inner capillary and intermediate capillary on single-cell analysis.

The distance between inner capillary and intermediate capillary, which represent the interaction time between extract fluid (MeOH) and cells, can determine the extraction efficiency of metabolites in cells. As shown in Figure S3.3, when the distance between inner capillary and intermediate capillary was 4 mm, detected PC (34:1) had the highest intensity, and the number of cells detected per minute was also the most, 4 mm was thus selected as the optimal distance during further experiments.
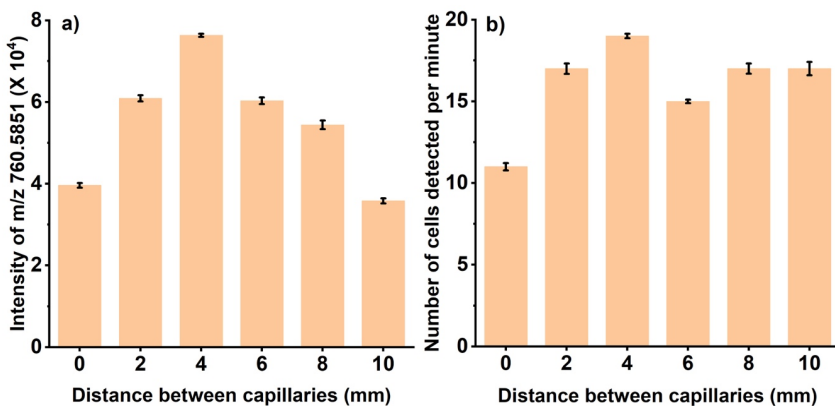
Figure S3.3. The effect of the distance of inner capillary and intermediate capillary on single-cell analysis (PANC-1 cell suspension was chosen as the example). (a) Extraction efficiency of PC (34:1), (b) number of cells detected per minute.

3.5.2.3 Effect of the voltage of DBDI on single-cell analysis.

In brief, the PANC-1 cell suspension (at a flow rate of 1 μL/min) and MeOH (at a flow rate of 11 μL/min) were introduced into the DBDI source via the cell introduction system. As shown in Figure S3.4, when the DBDI voltage was 0 kV, there were no obvious pulse peak signals in TIC (Figure S3.4a) and EIC (Figure S3.4b). When the DBDI voltage is between 2.2 kV and 2.8 kV, the pulse peak signals appeared in both TIC (Figure S3.4a) and EIC (Figure S3.4b). As mentioned in the main text, this is because only when the DBDI was on, the compounds in the cells could be ionized. A voltage of 2.6 kV was chosen for further experiments. Interestingly, it can be seen that when the voltage was increased to between 3 kV and 3.5 kV, the pulse peak signals can still be observed from the TIC (Figure S3.4a), but the number of pulse peak signals in EIC decreased and the intensity of pulse peak signals in EIC became very low as well, which was probably due to the fact that although the DBDI source has been considered a soft ionization source, when the voltage increased above 3kV in this study, the lipid peaks were fragmented.
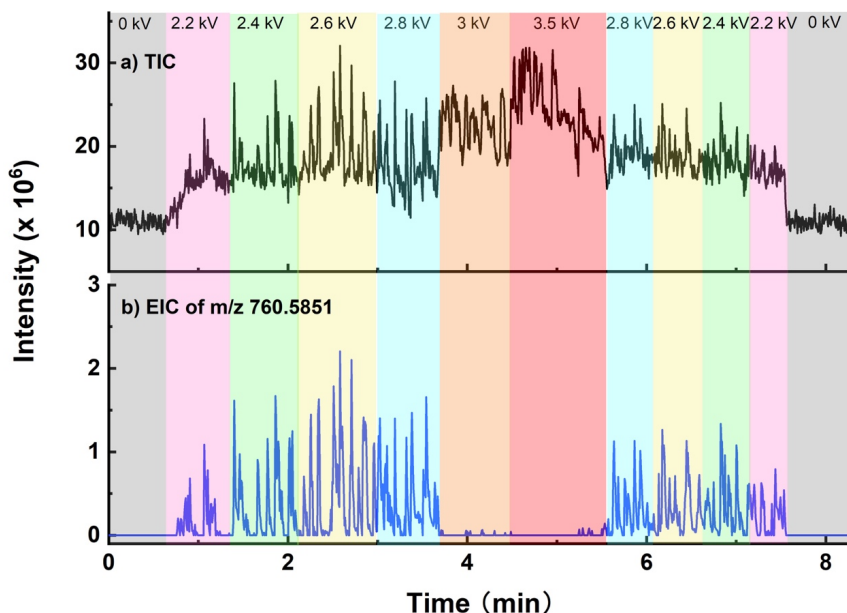
Figure S3.4. Effect of the voltage of DBDI on single-cell signal (PANC-1 cell suspension was chosen as the example). (a) Total ion chromatogram (TIC), (b) extracted ion chromatogram (EIC) of m/z 760.5851.

3.5.2.4 Effect of the composition and flow rate of lysis/extraction fluid on single cell analysis.

A suitable lysis/extraction fluid can help lyse cells and increase the coverage and signal intensity of the extracted metabolites. MeOH, EtOH, MeOH: H_2O = 1:1 and EtOH: H_2O = 1:1 were investigated in this work. As shown in Figure S3.5, the detected PC (34:1) had the highest intensity when pure MeOH was chose as the lysis/extraction fluid, and the number of cells detected per minute was also more than that detected in other lysis/extraction fluid, so MeOH was selected as the lysis/extraction fluid for further experiments.

The flow rate of MeOH has been optimized (Figure S3.6). As the flow rate was 11 μL/min, the signal of PC (34:1) and the number of

detected cells were higher than other flow rates, so the flow rate of MeOH was set to 11 µL/min during the entire experiment.
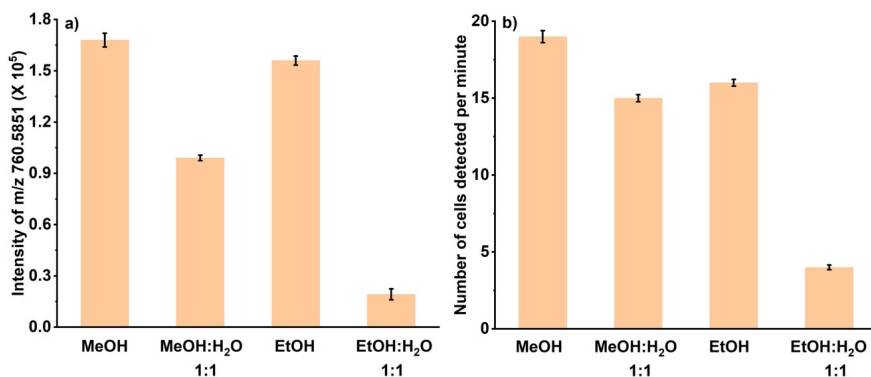
Figure S3.5. The effect of lysis/extraction fluid on single-cell analysis (PANC-1 cell suspension was chosen as the example). (a) Extraction efficiency of PC (34:1), (b) number of cells detected per minute.
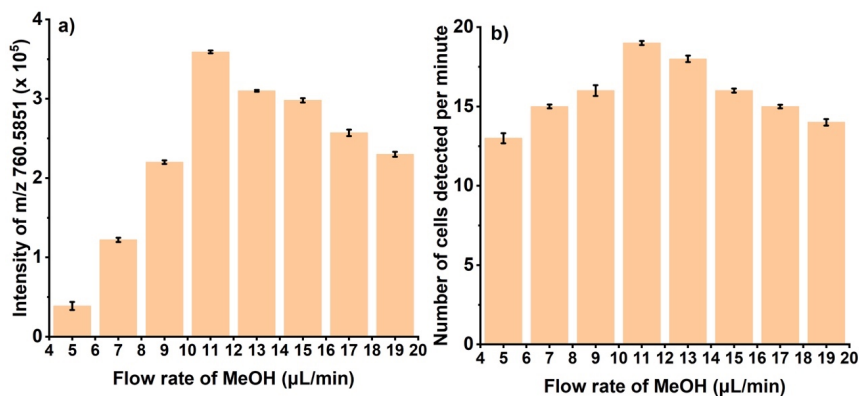
Figure S3.6. The effect of the flow rate of MeOH on single-cell analysis (PANC-1 cell suspension was chosen as the example). (a) Extraction efficiency of PC (34:1), (b) number of cells detected per minute.

3.5.3 Feasibility of single cell DBDI-MS

To further evaluate the performance of DBDI-MS, analysis of different cell suspensions was carried out, including PANC-1 cells (3×10^4 cells/mL), CFPAC-1 cells (3×10^4 cells/mL) and H6c7 cells (3×10^4 cells/mL). The cell suspension was introduced into the DBDI source at a flow rate of 1 μL/min under a continuous low-speed shaking by a vortex, which prevents the cells from depositing to the bottom of the vial, and make the suspensions homogenous and monodisperse. As can be seen from Figures S3.7a–c, Figures S3.8a–c and Figures S3.9a–c, the frequency and position of the m/z 760.5851 and m/z 732.5538 peaks matched with the frequency and position of the TIC, and the peak signals did not overlap with each other. Obvious lipid signals could be observed in the mass spectrum corresponding to the peaks (Figure S3.7e, Figure S3.8e and Figure S3.9e), but no lipid signals could be observed in the mass spectrum corresponding to the EIC between two peaks (Figure S3.7d, Figure S3.8d and Figure S3.9d). At a concentration of 3×10^4 cells/mL, more than 500 cells were detected in 18 minutes, and at a concentration of 2×10^4 cells/mL, more than 300 cells were detected in 18 minutes.
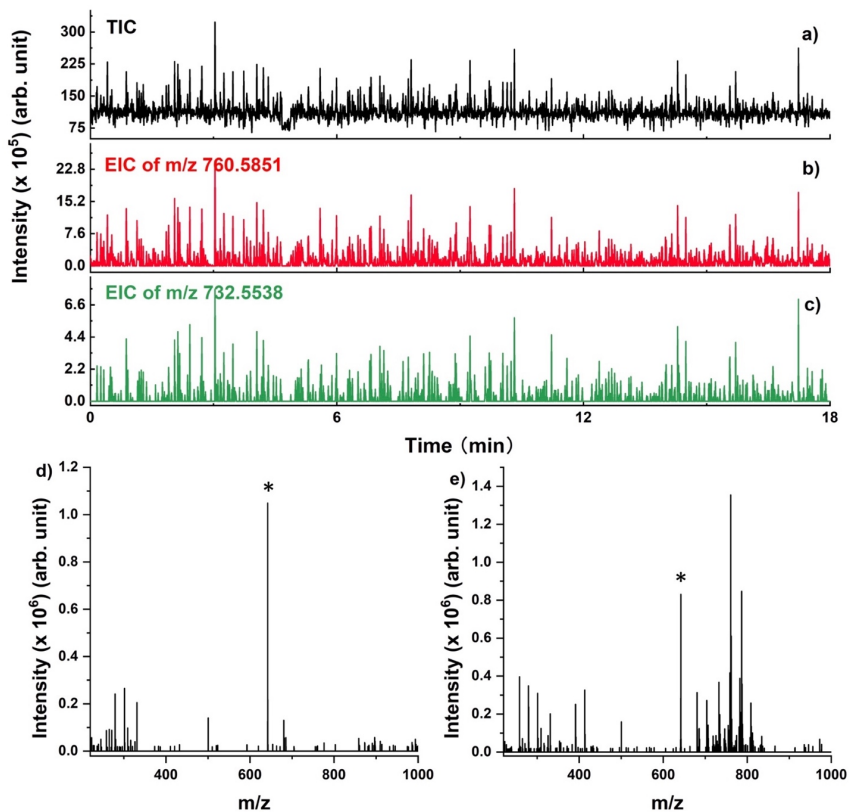
Figure S3.7. PANC-1 suspension analyzed by DBDI-MS. (a) Total ion chromatogram (TIC), (b) extracted ion chromatogram (EIC) of m/z 760.5851, (c) EIC of m/z 732.5538, (d) mass spectrum of blank, and (e) mass spectrum of PANC-1. The asterisk (*) indicates electronic noise in the spectra.
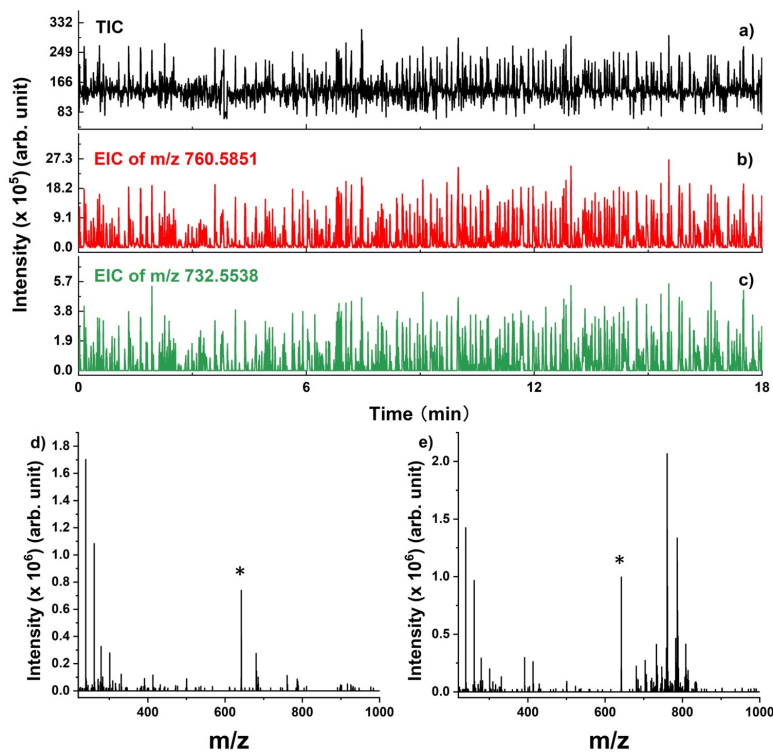
Figure S3.8. CFPAC-1 suspension analyzed by DBDI-MS. (a) Total ion chromatogram (TIC), (b) extracted ion chromatogram (EIC) of m/z 760.5851, (c) EIC of m/z 732.5538, (d) mass spectrum of blank, and (e) mass spectrum of CFPAC-1. The asterisk (*) indicates electronic noise in the spectra.
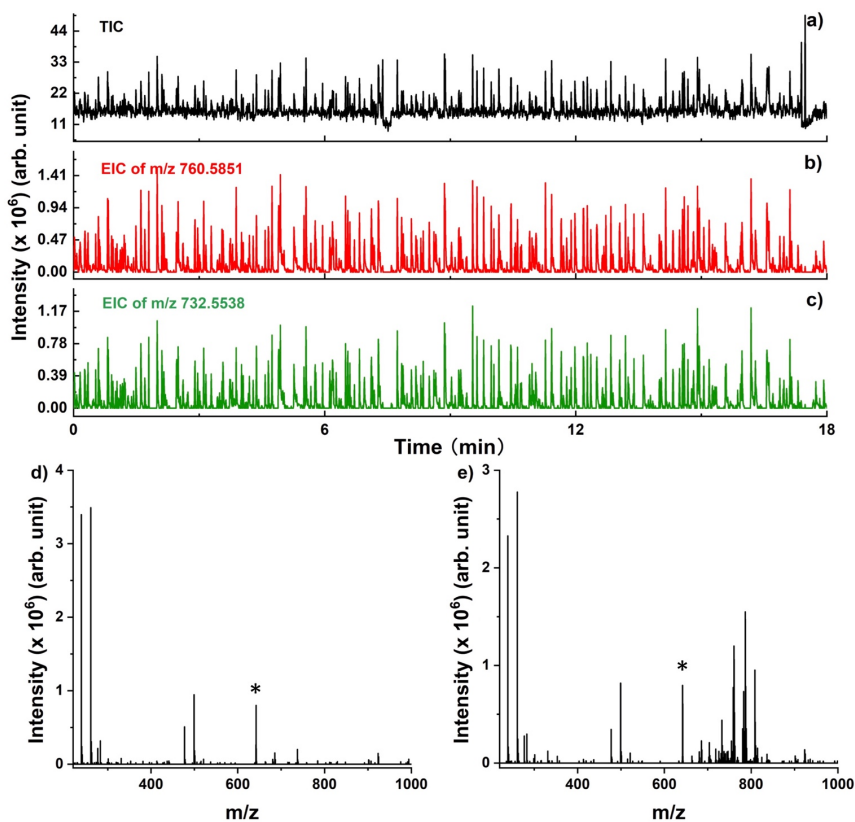
Figure S3.9. H6c7 suspension analyzed by DBDI-MS. (a) Total ion chromatogram (TIC), (b) extracted ion chromatogram (EIC) of *m/z* 760.5851, (c) EIC of *m/z* 732.5538, (d) mass spectrum of blank, and (e) mass spectrum of H6c7. The asterisk (*) indicates electronic noise in the spectra.

Table S3.1. Comparison between the calculated number of CFPAC-1 and the detected number of CFPAC-1 at different cell concentrations.

Cell density, cells mL^{-1}	Calculated cell number [min]	Detected cell number [min]					Average detected cell number [min]
5 x 10^3	5	4	3	4	4	3	3.6
1 x 10^4	10	9	8	8	9	7	8.2
2 x 10^4	20	19	20	19	18	18	18.8
3 x 10^4	30	27	26	27	26	28	26.8
4 x 10^4	40	37	36	39	39	38	37.8

Table S3.2. Comparison between the calculated number of H6c7 and the detected number of H6c7 at different cell concentrations.

Cell density, cells mL^{-1}	Calculated cell number [min]	Detected cell number [min]					Average detected cell number [min]
5 x 10^3	5	4	3	4	6	5	4.4
1 x 10^4	10	7	7	9	8	8	7.8
2 x 10^4	20	16	17	16	19	18	17.2
3 x 10^4	30	31	27	26	25	28	27.4
4 x 10^4	40	38	37	35	39	38	37.4

3.5.4. Metabolite profiling and discrimination of cell type

Abbreviations: Phosphatic acid (PA), phosphoethanolamine (PE), phosphatidylglycerol (PG), phosphatidylserine (PS), phosphatidylinositol (PI), phosphatidylcholine (PC), monoglycerides (MG), diglycerides (DG) and triglycerides (TG), cholesteryl ester (CE).

Table S3.3 Detected metabolite classification.

	Azasteroids and derivatives	1
	Ceramides	4
	Cholestane steroids	1
	Cycloartanols and derivatives	1
	Diradylglycerols	13
	Eicosanoids	1
	Fatty acid esters	5
	Fatty acids and conjugates	1
Lipids	Fatty alcohols	1
	Glycerophosphates	13
	Glycerophosphocholines	58
	Glycerophosphoethanolamines	42
	Glycerophosphoglycerols	13
	Glycerophosphoserines	11
	Glycosphingolipids	5
	Sesquaterpenoids	1
	Steroid esters	9
	Triradylcglycerols	8
Organic acids and derivatives	Amino acids	1
Organoheterocyclic compounds	Diazines	1
Organic oxygen compounds	Carbonyl compounds	1

Since the time available for analyzing a single cell was very limited, it was difficult to perform tandem MS for better characterization of the metabolites in a single cell. As shown in Figure S3.10, several lipids (SM(d34:1), PC(O-32:1), PC(32:1), PC(33:1), PC(34:1), PC(36:2)) in a population of PANC-1 cells were selected for tandem-MS analysis.
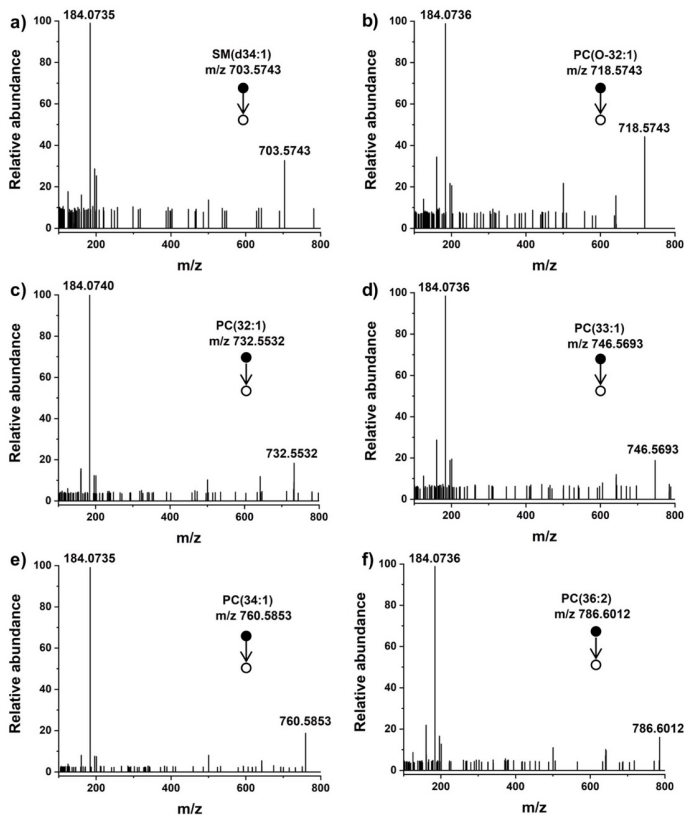
Figure S3.10. High-resolution MS/MS spectra of (a) SM(d34:1), (b) PC(O-32:1), (c)PC(32:1), (d)PC(33:1), (e)PC(34:1) and (f)PC(36:2).
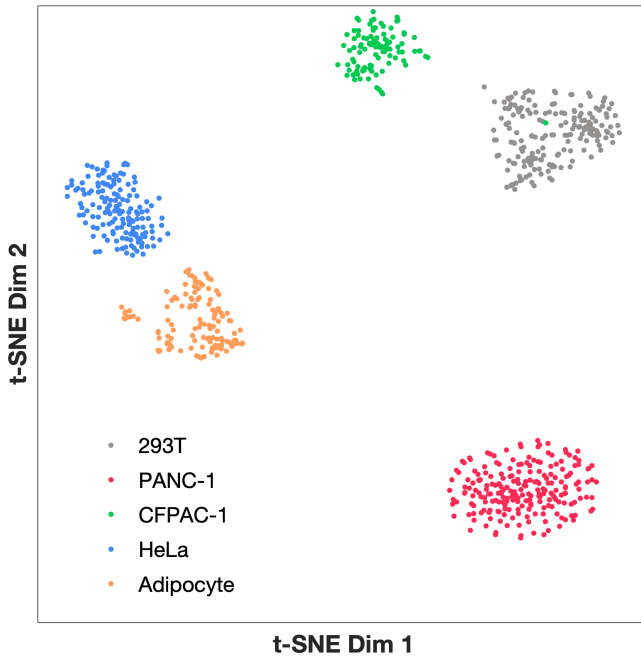
Figure S3.11. The distributed stochastic neighbor embedding (t-SNE) analysis of five cell types.

3.5.5 Single-cell DBDI-MS metabolic profile identify deregulated lipid metabolism in PDAC cells
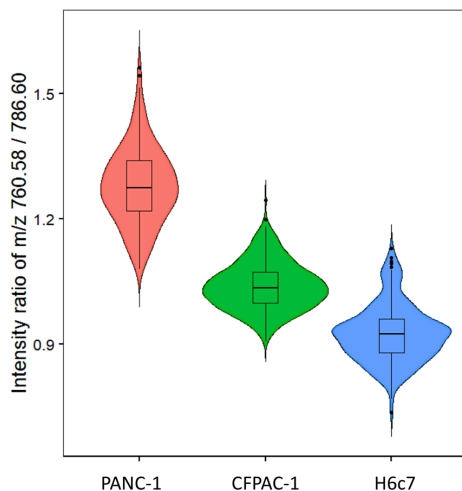
Figure S3.12. Violin plots for comparison of the intensity ratio of m/z 760.58/786.60 (PC(34:1)/ PC(36:2)) in PANC-1, CFPAC-1 and H6c7 cells at the single-cell level.
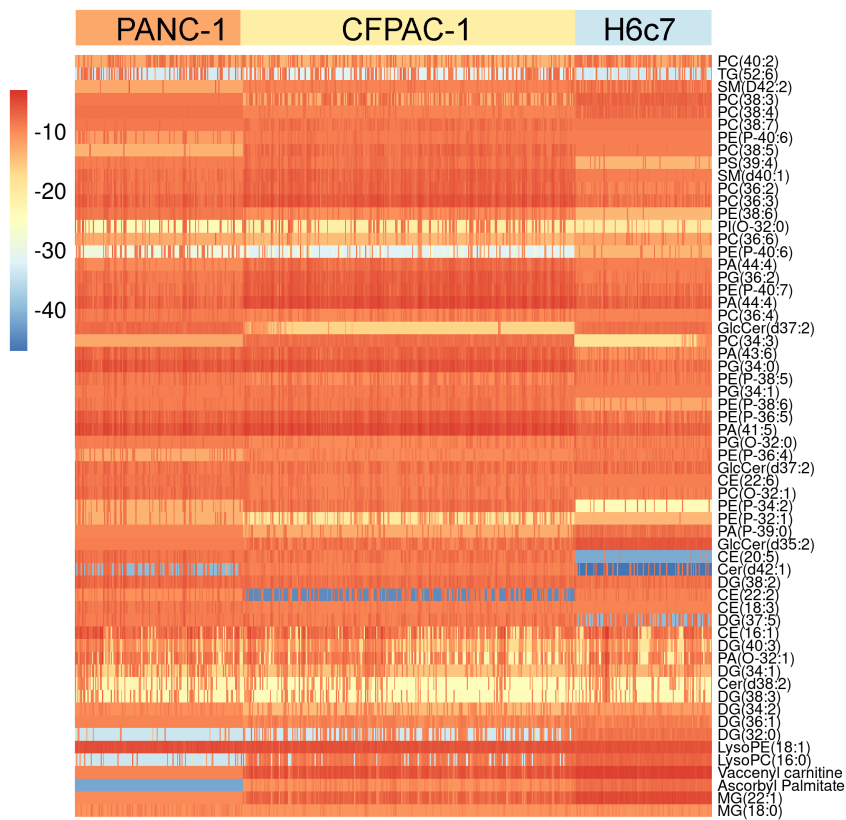
Figure S3.13. Heatmap of the single-cell metabolites in PANC-1, CFPAC-1 and H6c7.

3.5.6 Deregulated ACLY levels in PDAC
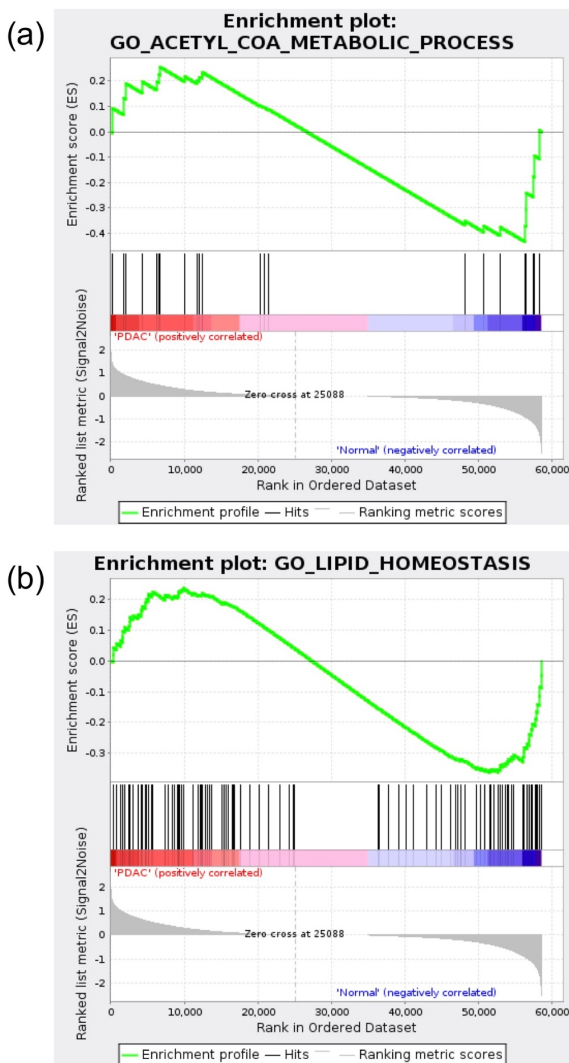
Figure S3.14. (a-b) Gene set Enrichment Analysis (GSEA) of acetyl-CoA metabolic process and lipid metabolism biological pathway in the same TCGA dataset described in Figure 3.5a.

3.5.7 ACLY inhibition induced lipid redistribution was specifically detected by the sensitive single cell DBDI-MS
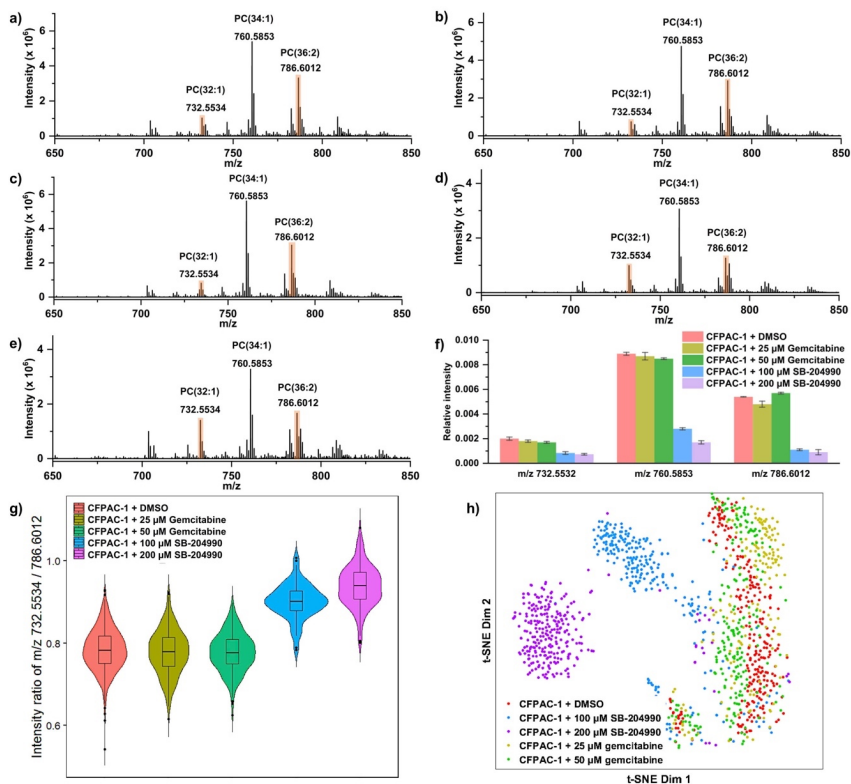
Figure S3.15. Results of the CFPAC-1 with different treatments. (a) Mass spectrum of CFPAC-1 treated with DMSO. (b) Mass spectrum of CFPAC-1 treated with 25 μM Gemcitabine. (c) Mass spectrum of CFPAC-1 treated with 50 μM Gemcitabine. (d) Mass spectrum of CFPAC-1 treated with 100 μM SB-204990. (e) Mass spectrum of CFPAC-1 treated with 200 μM SB-204990. (f) Bar plots for the changes of lipid contents after different treatments. (f) Violin plots for comparison of the intensity ratio of PC(32:1)/PC(36:2) (m/z 732.55/786.60) in CFPAC-1 with different treatments. (g) t-SNE analysis of CFPAC-1 with different treatments.

Hybrid Ionization Source Combining Nanoelectrospray and Dielectric Barrier Discharge Ionization for the Simultaneous Detection of Polar and Nonpolar Compounds in Single Cells

Single-cell metabolomics is expected to deliver fast and dynamic information on cell function; therefore, it requires rapid analysis of a wide variety of very small quantities of metabolites in living cells. In this work, a hybrid ionization source that combines nanoelectrospray ionization (nanoESI) and dielectric barrier discharge ionization (DBDI) is proposed for single-cell analysis. A capillary with a 1 μm i.d. tip was inserted into cells for sampling and then directly used as the nanoESI source for ionization of polar metabolites. In addition, a DBDI source was employed as a post-ionization source to improve the ionization of apolar metabolites in cells that are not easily ionized by ESI. By increasing the voltage of the DBDI source from 0 to 3.2 kV, the classes of detected metabolites can be shifted from mostly polar to both polar and apolar to mainly apolar. Plant cells (onion) and human cells (PANC-1) were

investigated in this study. After optimization, 50 compounds in onion cells and 40 compounds in PANC-1 cells were observed in ESI mode (3.5 kV) and an additional 49 compounds in onion cells and 73 compounds in PANC-1 cells were detected in ESI (3.5 kV)-DBDI (2.6 kV) hybrid mode. This hybrid ionization source improves the coverage, ionization efficiency, and limit of detection of metabolites with different polarities and could potentially contribute to the fast-growing field of single-cell metabolomics.

4.1 Introduction

Single-cell metabolic analysis provides useful information about cellular heterogeneity.[33,140-141] However, single-cell metabolomics is very challenging due to the low abundance and diverse structure of intracellular metabolites.

Mass spectrometry is a label-free analytical technique with high sensitivity, good selectivity, and fast response. It can simultaneously detect multiple low-molecular-weight metabolites in a cell and has been widely used for single-cell metabolomics.[142-144] The ionization method is crucial as it determines the coverage and limit of detection (LOD) of the metabolome. Mass spectrometry-based single-cell metabolomics mainly relies on secondary ion mass spectrometry (SIMS),[26,33,145] matrix-assisted laser desorption/ionization mass spectrometry (MALDI-MS),[25,63] and nanoelectrospray ionization mass spectrometry (nanoESI-MS).[141,146] SIMS has a high spatial resolution and can be used for subcellular analysis, but many fragments are usually generated during the ionization process. Although the spatial resolution of MALDI is far less than that of SIMS, MALDI is a soft ionization source that can detect many types of compounds with relatively high sensitivity. MALDI and SIMS have many applications in the area of single-cell imaging.[145,147-148] ESI-

based methods can be used for sampling and ionization of metabolites in living cells. Pioneering work in this area has been done by Masujima and co-workers.[149-151] They developed a "live single-cell MS" (LSC-MS) method and applied it to analyze metabolites in mouse embryonic fibroblasts cells,[151] human-derived circulating tumor cells (CTCs),[149] and plant cells.[150] Vertes and co-workers have demonstrated the efficient use of capillary microsampling combined with ESI and ion mobility separation (IMS) followed by MS for the analysis of single plant and animal cells.[152-154] Single-cell metabolite analysis by laser ablation ESI (LAESI) MS was also practiced by the same group,[37,155] and recently, they used it for single-cell high-throughput analysis.[156] Nemes and co-workers combined capillary electrophoresis (CE) and ESI-MS for single-cell analysis.[157-159] More recently, they enabled in vivo single-cell proteomics and metabolomics in South African clawed frog embryos *via* CE-ESI-MS.[160] Both of these groups used probe sampling and ESI ionization methods to study single cells. Each single-cell ionization method has its own advantages. For example, nanoESI is suitable for the ionization of polar metabolites, but it is less suitable for ionizing nonpolar metabolites due to its ionization mechanism.

We reasoned that different ionization methods can complement each other, which should be beneficial for the study of single-cell metabolomics. For example, dielectric barrier discharge ionization (DBDI) source is a sensitive, efficient, and cheap low-temperature plasma source, which is based on completely different ionization processes than ESI.[94,98] The plasma contains many reactive species, including electrons, ions, neutral atoms, excited states, radicals, and photons.[161] Reactive species in the plasma determine the ionization reactions and product ions.[94,101,162] Some reactive species (e.g., $N_2^{+\bullet}$, $O_2^{+\bullet}$, N_2^*) will lead to charging of nonpolar compounds through charge transfer, electron impact, or Penning ionization processes, while other reactive species (e.g., $(H_2O)_n H^+$) ionize polar compounds

via protonation. The applied voltage is a crucial parameter that influences the ionization efficiency and selectivity of the generated product ions. By increasing the plasma voltage, the energy and the number of electrons will increase.[95] A high applied voltages will thus increase the ionization efficiency.[163] In addition, DBDI can be operated with dopants to boost the ion yield of specific analytes.[96] Our group has developed a small, soft, and practical DBDI source with high ion transmission efficiency and has used it for single-cell metabolism analysis.[34] We have proven that DBDI-MS can detect multiple metabolites at the single-cell level and distinguish different cell types based on the information on detected metabolites.

Possible strategies to improve the ionization efficiency of nonpolar metabolites and expand the detection range of metabolites in single cells are to develop alternative ionization sources, post-ionization sources, or versatile hybrid ionization sources for single-cell metabolomics. Hybrid ionization sources have been used in the past, although only on the bulk level, never in the context of the analysis of nonpolar metabolites in single cells. For example, Shiea and co-workers introduced a combination of ESI with atmospheric pressure chemical ionization to post-ionize neutrals produced by laser desorption and thermal desorption. Both polar and nonpolar analytes were observed.[164] Another example is the use of matrix-assisted laser desorption electrospray ionization (MALDESI) for imaging applications, which was pioneered by Muddiman and co-workers.[165-166] They combined the benefits of MALDI and ESI post-ionization to increase the ion yield. The Franzke group also reported that DBDI can increase the signal intensity of lysine that has been ionized by ESI.[167] The general concept is to use a post-ionization scheme to boost the ion yield, and we propose that it would also be advantageous to ionize nonpolar metabolites and metabolites that exhibit low ionization yield. Therefore, we hypothesized that

combining ESI and DBDI will enlarge the range of metabolites that can be covered and lower the LOD, which is crucial for single-cell metabolomics.

In this study, we introduce a hybrid nanoESI-DBDI source for single-cell analysis, which has two modes: an "ESI mode" and a "hybrid mode" to detect intracellular metabolites with different polarities. As a proof of principle, a glass capillary with a tip diameter of 1 µm was inserted into a cell for sucking in cell contents (Figure 4.1a), and then the cellular metabolites were ionized by the hybrid nanoESI-DBDI source (Figure 4.1b), where the nanoESI primarily ionizes polar metabolites, followed by a DBDI source as a post-ionization source to ionize less polar, nonpolar metabolites and metabolites with low ESI ionization yield. We were able to demonstrate the detection of metabolites from single plant and animal cells. This hybrid source improved the coverage of metabolites of different polarities from 50 metabolites (ESI mode) to 86 metabolites (hybrid mode) in onion cells, and from 40 metabolites (ESI mode) to 111 metabolites (hybrid mode) in PANC-1 cells.
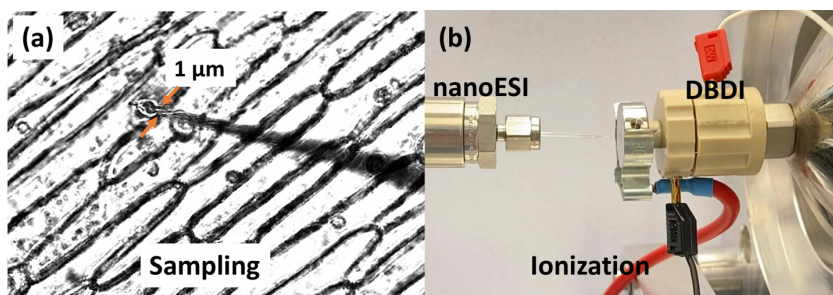
Figure 4.1. (a) Single cell sampling process. (b) Photo of the nanoESI-DBDI ionization source.

4.2 Experimental Section

4.2.1 Chemicals

Methanol, acetonitrile (ACN), and chlorobenzene were purchased from Sigma-Aldrich Chemie GmbH (Buchs, Switzerland). Testosterone, l-valine, anthracene, fluoranthene, and *N,N*-dimethylformamide (DMF) were purchased from Fluka Chemie GmbH (Buchs, Switzerland). l-Threonine was purchased from AppliChem GmbH (Darmstadt, Germany). l-Cysteine was purchased from abcr GmbH (Karlsruhe, Germany). 08:0 PC and 12:0 PC (DLPC) were purchased from Avanti Polar Lipids (Alabaster). Yellow onions (*Allium cepa*) were purchased from a local supermarket in Zurich. Phosphate-buffered saline (PBS) was purchased from Thermo Fisher Scientific (Buchs, Switzerland). PANC-1 cells were purchased from American Type Culture Collection (ATCC).

4.2.2 Sample Preparation

Standard solutions of L-threonine, L-valine, L-cysteine, testosterone, 08:0 PC, 12:0 PC (DLPC), anthracene, and fluoranthene were prepared at a concentration of 10 ppm in MeOH/water (1:1), ACN/DMF (1:1), and chlorobenzene/DMF (1:1) separately. A mixture of the eight compounds was prepared at a concentration of 10 ppm in MeOH/water (1:1).

4.2.3 Cell Culture and Single-Cell Sampling

The epidermal cell layer of yellow onion bulbs was freshly peeled and placed on a glass slide, which was then placed on the platform of an inverted microscope (Nikon Eclipse Ti Light Microscope). A micropipette puller (Sutter Instrument, Novato) was used to fabricate capillaries with a 1 μm tip. Next, the capillary was inserted into a capillary holder installed on a home-built manipulator. By adjusting the angle and distance between the tip of the capillary and

the cell, the capillary was carefully inserted into the cell. The sampling process was observed by optical microscopy (as shown in Figure 4.1a). Around 30% of the cytoplasmatic cell content was extracted by applying a negative pressure applied by the syringe on the back of the capillary holder. After the cell sampling, the tip of the pulled capillary was backfilled with 2 μL of an assistant solvent.

PANC-1 cells were grown in Dulbecco's modified Eagle's medium (DMEM) with 10% (v/v) fetal bovine serum and 1% penicillin–streptomycin (P/S) at 37 °C in a humidified incubator (Thermo Fisher Scientific) with 5% CO_2. Before single-cell sampling, the dish was washed twice with PBS and then washed twice with ammonia formate. The dish was then placed on the platform of an inverted microscope to select a target cell and observe the sampling process. The subsequent single PANC-1 cell sampling method was the same as for single onion cells. Sampling images of PANC-1 cell and onion cell are shown in Figure S4.1.

4.2.4 Hybrid Ionization Source

In this study, a hybrid ionization source (Figures 4.1b and S4.2) that combines nanoESI and DBDI was used to do single-cell analysis. A home-built nanoESI source was used to ionize polar metabolites in cells, followed by an active capillary plasma ionization source (based on a dielectric barrier discharge ionization) to ionize nonpolar metabolites in cells. The details about the home-built DBDI source can be found in a previous publication.[98] In brief, the DBDI has two electrodes (Figure S4.2), an inner electrode (grounded, stainless steel, ID: 0.6 mm and OD: 1.0 mm) and an outer electrode (high voltage, copper, ID: 1.55 mm, around a glass capillary). They are isolated by a glass capillary that acts as a dielectric barrier. When a high alternating current (AC) voltage is applied to the outer electrode, a plasma is ignited inside the capillary. The ignition voltage of DBDI is around 2.0 kVpp. The operating AC voltage of

DBDI in this work was 2.2–3.2 kVpp. The DBDI source was connected directly to the inlet capillary of the mass spectrometer to achieve almost 100% transmission efficiency of the ions formed.

4.2.5 Mass Spectrometry

An LTQ Orbitrap mass spectrometer (Thermo Fisher Scientific, San Jose) was used to acquire mass spectra in positive-ion mode and in full-scan mode at a resolution of 30 000 full width at half-maximum (FWHM) (at m/z 400) with a mass tolerance specified to be <10 ppm. The mass-to-charge range was set to 50–1000, capillary voltage was 50 V, tube lens voltage was 120 V, capillary temperature was 320 °C, and AGC target = 10^6. Mass spectra were acquired using 1 microscan and a maximum injection time of 50 ms.

4.2.6 Data Analysis

The Xcalibur software version 2.2 (Thermo Fisher Scientific, San Jose) was used to record the MS raw data generated from the LTQ Orbitrap. MS raw data (.raw) was converted to the mzXML format by the MSConvert software (ProteoWizard, v3.0)[136] and then imported into Matlab (R2019b version, MathWorks, Natick, MA) for preprocessing.

Metabolite assignments were carried out by comparing the observed mass with the theoretical mass in an onion metabolite database[140] and some other online databases, including Plant Metabolome Database (http://scbt.sastra.edu/pmdb/), Human Metabolome Database (https://hmdb.ca/), and the METLIN metabolite database (https://metlin.scripps.edu/).

4.3 Results and Discussion

4.3.1 Effect of the DBDI Source Voltage and the nanoESI-DBDI Ionization Mechanism

To evaluate the ability of nanoESI-DBDI-MS to analyze polar and nonpolar compounds, eight model compounds with different polarities were selected: L-threonine, L-valine, L-cysteine, testosterone, 08:0 PC, 12:0 PC (DLPC), anthracene, and fluoranthene.

We first investigated the effect of the DBDI operating voltage on the ionization efficiency of two compounds with different polarities. During the entire experiment, the nanoESI was turned on, using a voltage of 3.5 kV. As shown in Figure 4.2a, when the DBDI was turned off, L-threonine was ionized by the ESI source through proton transfer. When the voltage of DBDI was between 2.2 and 2.8 kV, the signal of L-threonine was higher than with only the ESI running. This may be because reactive species in the plasma (H^+, H_3O^+, cluster ions, etc.) can increase the overall ion yield of L-threonine *via* proton transfer. However, the signal of L-threonine decreased with increasing DBDI voltage. Above 2.8 kV, the signal of L-threonine dropped significantly. We interpret this to be the result of L-threonine fragmentation (Figure S4.3), resulting in a decrease in its parent ion signal. On the contrary, anthracene could not be ionized when only the ESI was turned on (Figure 4.2b). When the DBDI was turned on, the signal of anthracene increased with increasing DBDI voltage. Anthracene may thus be mainly ionized *via* charge transfer, electron impact, or Penning ionization. As the DBDI voltage increases, the number of electrons in the plasma also increases, which helps to ionize anthracene, resulting in a signal enhancement. When the voltage of the DBDI source was 2.6 kV, the intensity of L-threonine was higher than when only the ESI was turned on, and the signal of anthracene was also relatively stable. Therefore, 2.6 kV was selected as the DBDI operating voltage for subsequent experiments.

In general, by simply adjusting the DBDI voltage from low to high (0–3.2 kV), the ionization reaction in the hybrid nanoESI-DBDI source is switched from proton transfer to charge transfer, electron impact, and Penning ionization. In this way, nanoESI-DBDI-MS can not only detect polar compounds but also analyze nonpolar compounds.
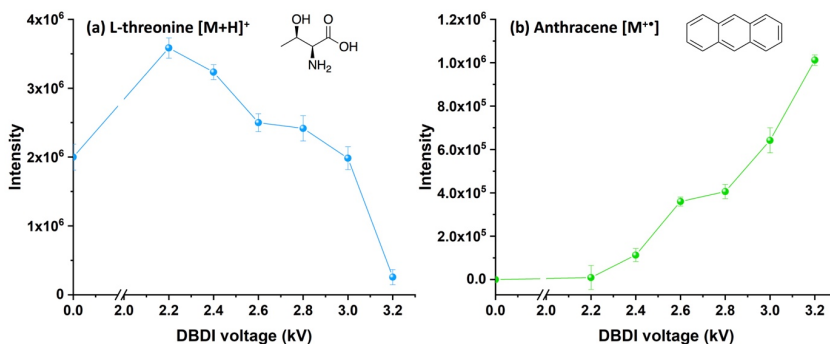
Figure 4.2. Effect of the DBDI voltage on the intensity of (a) L-threonine and (b) anthracene. ESI voltage was set to 3.5 kV in both cases.

4.3.2 Effect of Assistant Solvents

The effect of different solvents on the ionization efficiency of the model compounds was also studied.[96,168] Three solvent mixtures with different polarities (MeOH/water = 1:1, ACN/DMF = 1:1, chlorobenzene/DMF = 1:1) were used to dissolve the samples investigated here. The effect of these three assistant solvents on the intensity of the eight model compounds is shown in Figure S4.4 and described in detail in Section S4.5.3 in the Supporting Information (SI). Since both polar compounds and nonpolar compounds have good ionization efficiencies when MeOH/water (1:1) was used as the

assistant solvent, MeOH/water (1:1) was selected as the solvent for subsequent experiments.

The mass spectra of the eight compounds dissolved in MeOH/water (1:1) are shown in Figure 4.3. In ESI mode, the product ions of three polar amino acids appeared as $[M + H]^+$ (Figures 4.3a–c). In hybrid mode, the ionization efficiencies of all product ions increased. For the three lipids (Figures 4.3d–f), the observed product ions were $[M + H]^+$ and $[M + Na]^+$. Turning on the DBDI increased the ionization efficiencies of all product ions. For the two nonpolar PAHs (Figures 4.3 g,h), no prominent product ions were observed in ESI-only mode. In hybrid mode, $[M]^{+\bullet}$ ions were the dominant product ions. Based on the above results, it can be seen that when the DBDI voltage was set to 2.6 kV, the protonated species (RH^+) in the plasma could improve the ionization of polar compounds to produce protonated molecular ions. Moreover, radical cations in the plasma could also promote ionization of nonpolar compounds.

By analyzing a mixture containing eight polar and nonpolar compounds, the ability of the hybrid source to simultaneously detect mixtures was further evaluated. As shown in Figure 4.4, L-threonine, L-valine, L-cysteine, testosterone, 08:0 PC, and 12:0 PC (DLPC) could be ionized in ESI mode, and their product ions were $[M + H]^+$. No product ions from anthracene and fluoranthene were observed. In the "ESI + DBDI" mode, L-threonine, L-valine, L-cysteine, testosterone, 08:0 PC, 12:0 PC (DLPC), and anthracene were all detected. The product ion of anthracene was $[M]^{+\bullet}$, the product ions of other compounds were also $[M + H]^+$, and the intensity of all of the product ions was significantly improved except for fluoranthene. Although no product ions from fluoranthene were observed in the mixture due to the ion-suppression effects among different product ions, fluoranthene can be ionized by ESI-DBDI alone. The signal-to-noise ratios (S/N) of the eight model compounds indeed improved

after turning on the DBDI. For example, the S/N of L-threonine increased ~3 times.
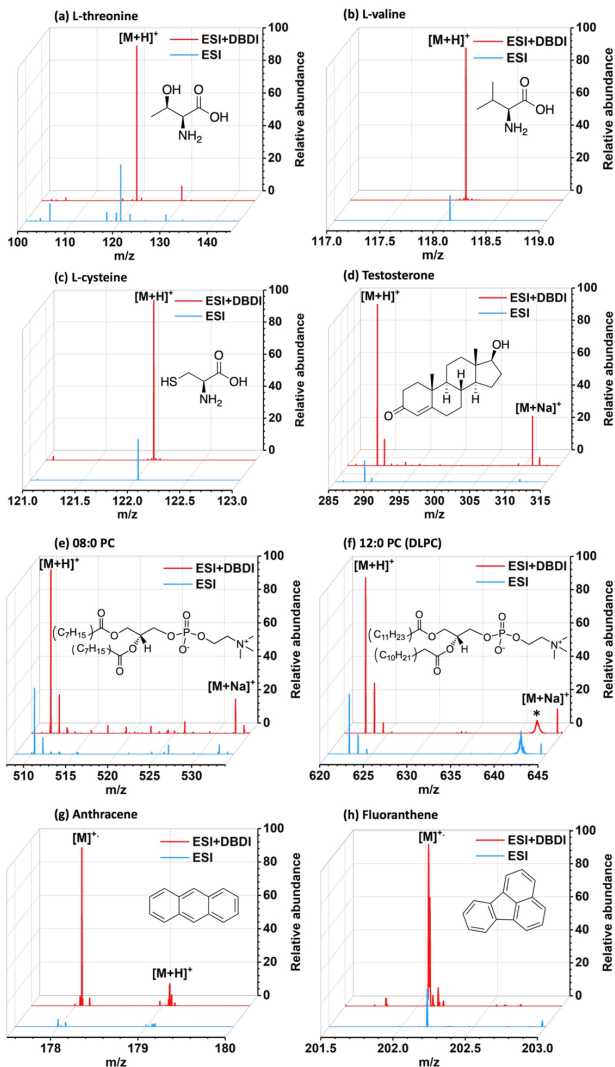
Figure 4.3. Mass spectra of eight model compounds with different polarities ionized by ESI and ESI-DBDI (solvent MeOH/water = 1:1): (a) L-threonine, (b) L-valine, (c) L-cysteine, (d) testosterone, (e) 08:0 PC, (f) 12:0 PC (DLPC), (g) anthracene, and (h) fluoranthene (ESI voltage: 3.5 kV; DBDI voltage: 2.6 kV; the asterisk (*) indicates electronic noise in the spectra).
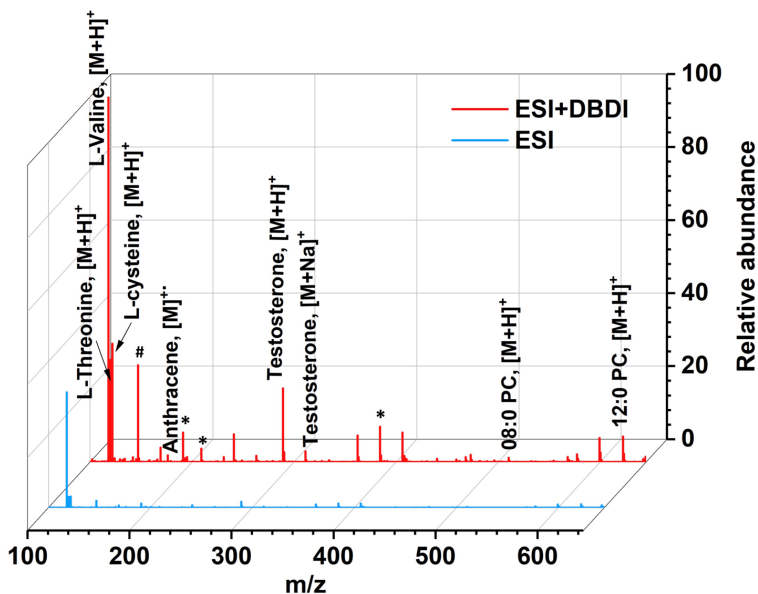
Figure 4.4. Mass spectrum of a mixture of eight model compounds with different polarities: L-threonine, L-valine, L-cysteine, testosterone, 08:0 PC, 12:0 PC (DLPC), anthracene, and fluoranthene (ESI voltage: 3.5 kV; DBDI voltage: 2.6 kV; the pound sign (#) indicates ACN + MeOH clusters; the asterisk (*) indicates electronic noise in the spectra).

4.3.3 Single-Cell Metabolite Analysis

We then applied the ESI-DBDI hybrid source to analyze metabolites in both single plant cells and animal cells, analyzing dozens of cells and measuring at least three replicates for each cell type to validate the reproducibility and robustness of our method.

We first chose onion cells as an application example because single-cell analysis of onion cells has been widely reported.[37,140,169-170] It is also relatively easy to do sampling on an onion cell. After microsampling, the onion cell metabolites were analyzed by ESI-DBDI-MS. In the positive-ion mode (m/z range between 50 and 1000), approximately 50 metabolites were detected in ESI mode in onion cells (Table S4.1). The observed product ions were mostly [M + H]⁺ and [M + Na]⁺, which are commonly seen in ESI. Some other common in-source fragments like [M + H – H_2O]⁺ and [M + H – 2H_2O]⁺ were also observed.[171] When the DBDI was turned on (2.6–2.8 kV), approximately 86 metabolites were detected (Table S4.2), among which 49 metabolites were not observed in ESI-only mode. Most of them were nonpolar. Except for [M + H]⁺, [M + Na]⁺, [M + H – H_2O]⁺, and [M + H – 2H_2O]⁺, [M]⁺• ions were also formed in hybrid mode.

Among all ionized metabolites in the onion cell, three polar metabolites (threonine, glutamine, and serine) and three nonpolar metabolites (2,5-dimethylthiophene, 1-propenyl propyl disulfide, and 5-hydroxymethyl-2-furancarboxaldehyde) were chosen as markers to highlight the differences between the ESI mode and the hybrid mode in detail. As shown in Figure 4.5a, when only ESI was on, only polar metabolites (threonine, glutamine, and serine) were detected. When the DBDI voltage was between 2.2 and 2.4 kV, the signal of threonine did not change significantly, and the signals of glutamine and serine were slightly reduced. At the same time, less polar metabolites (2,5-dimethylthiophene and 1-propenyl propyl disulfide) could be observed, but no clear signal from 5-hydroxymethyl-2-furancarboxaldehyde was observed. When the DBDI voltage was between 2.6 and 2.8 kV, the signal of polar metabolites (threonine, glutamine, and serine) decreased somewhat, while the signals of less polar metabolites (2,5-dimethylthiophene, 1-propenyl propyl disulfide, and 5-

hydroxymethyl-2-furancarboxaldehyde) increased significantly. When the DBDI voltage was between 3 and 3.2 kV, the signal of polar compounds was significantly reduced. Especially for glutamine, almost no obvious signal remained, but the signal of nonpolar compounds was further improved. By comparing the mass spectra of an onion cell in ESI mode (Figure 4.5b) and in hybrid mode (Figure 4.5c), it can be seen that the mass spectral profiles are quite different. For example, in ESI mode (Figure 4.6a), abundant peaks were at m/z 102.06 (assigned to threonine), m/z 164.07 (S-propyl-L-cysteine), m/z 175.12 (arginine), and m/z 184.07 (phosphorylcholine), which are polar onion cell metabolites. When the DBDI voltage was switched on to 2.6 kV (Figure 4.6b), less polar metabolites such as 3-(methylthiomethylthio)-1-propene (m/z 89.04), 2,5-dimethylthiophene (m/z 113.04), and di-1-propenyl sulfide (m/z 115.05) were also observed in addition to polar metabolites such as furfuryl acetate (m/z 123.04), arginine (m/z 175.12), and citrullin (m/z 198.09).

We also investigated PANC-1 cells, as an example of a human cell, by ESI-DBDI-MS in this study. As shown in Table S4.3, there were around 40 metabolites observed in ESI mode. The observed product ions and in-source fragments included [M + H]+, [M + Na]+, [M + K]+, [M + H – H_2O]+, and [M + H – $2H_2O$]+. Approximately 111 metabolites were detected (Table S4.4) in a single PANC-1 cell when the DBDI was turned on (2.6–2.8 kV), of which additional 71 metabolites were not observed in ESI-only mode. [M + H]+, [M + Na]+, [M + K]+, [M + H – H_2O]+, and [M]+• ions were the observed product ions in hybrid mode.
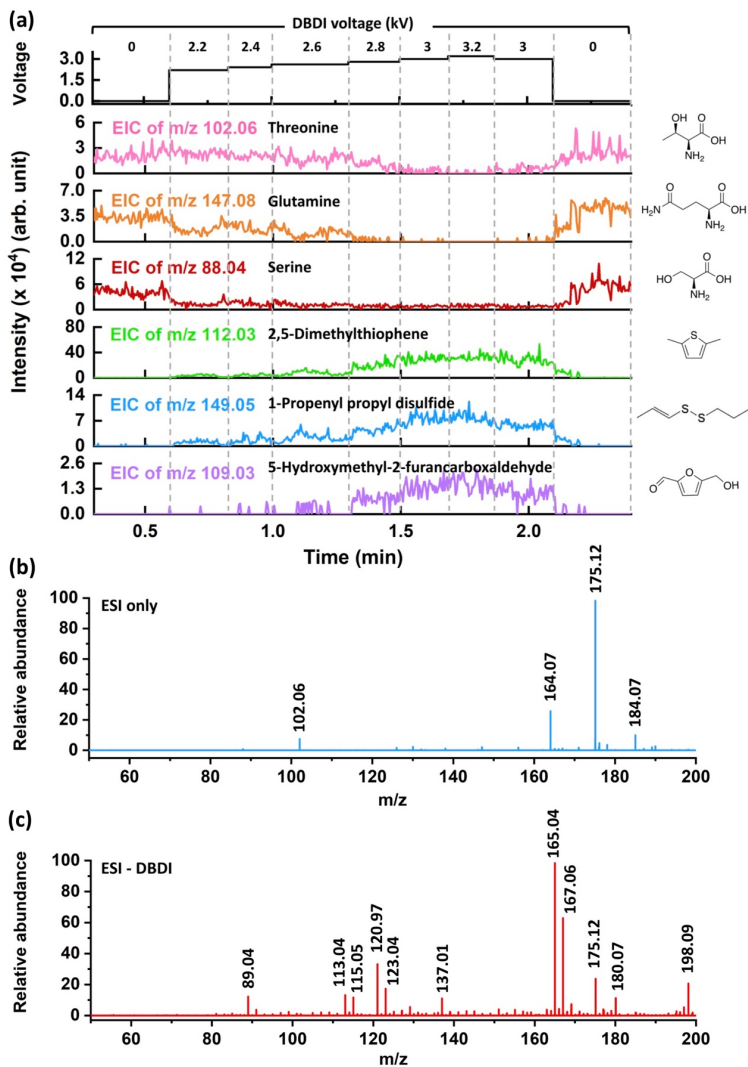
Figure 4.5. Metabolite analysis in a representative single onion cell. (a) total ion chromatogram (TIC) and extracted ion chromatograms (EICs) of six metabolites in onion cells in ESI/hybrid mode. (ESI was always on: 3.5 kV), (b) mass spectrum acquired in ESI (3.5 kV) mode, (c) mass spectrum acquired in ESI (3.5 kV)-DBDI (2.6 kV) hybrid mode.
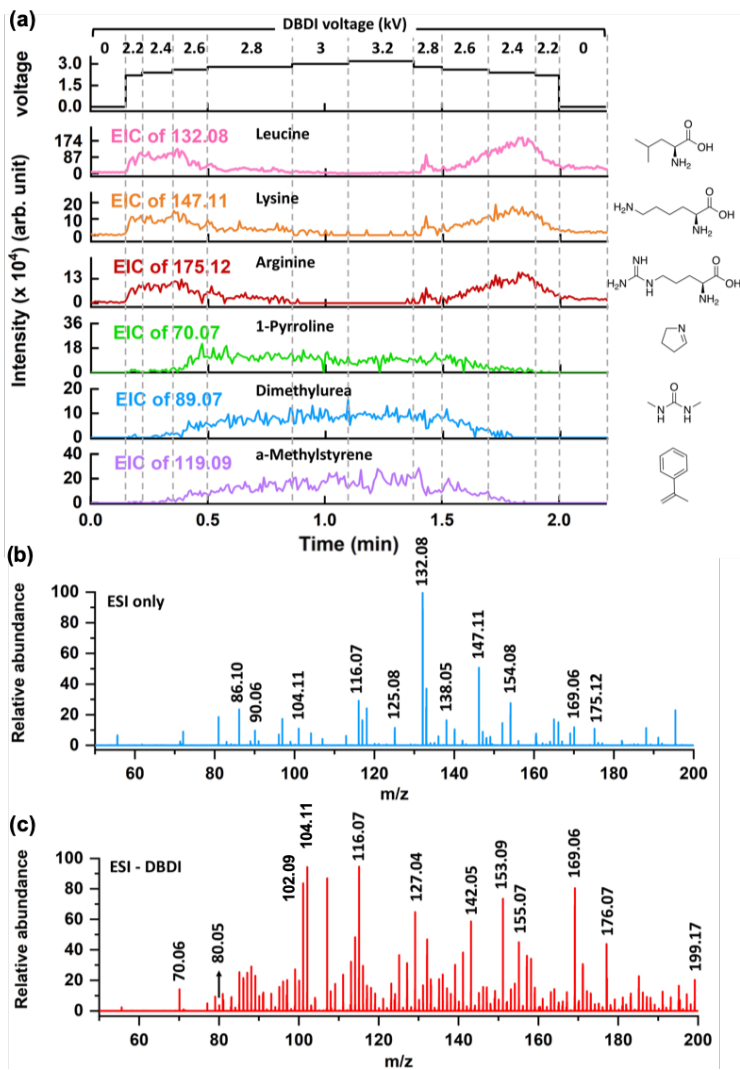
Figure 4.6. Metabolite analysis in a representative single PANC-1 cell. (a) total ion chromatogram (TIC) and extracted ion chromatograms (EICs) of six metabolites in onion cells in ESI/hybrid mode. (ESI was always on: 3.5 kV), (b) mass spectrum acquired in ESI (3.5 kV) mode, (c) mass spectrum acquired in ESI (3.5 kV)-DBDI (2.6 kV) hybrid mode.

Three polar (leucine, lysine, and arginine) and three nonpolar metabolites (1-pyrroline, dimethylurea, and a-methylstyrene) were selected as markers from all of the ionized compounds to show the difference between ESI mode and hybrid mode. As shown in Figure 4.6a, nonpolar metabolites (1-pyrroline, dimethylurea, and a-methylstyrene) were not detectable in ESI-only mode. When the DBDI voltage was between 2.2 and 2.6 kV, nonpolar metabolites (1-pyrroline, dimethylurea, and a-methylstyrene) were observed. At the same time, the signal of polar metabolites (leucine, lysine, and arginine) significantly increased. When the DBDI voltage was between 2.8 and 2.3 kV, the signal of polar metabolites (leucine, lysine, and arginine) was reduced, while the signals of nonpolar metabolites (1-pyrroline, dimethylurea, and a-methylstyrene) increased slightly. When the DBDI voltage was 3.2 kV, the signals of polar compounds were almost nondetectable, while the signals of nonpolar compounds did not change obviously. The mass spectral profiles of a PANC-1 cell in ESI mode and hybrid mode are evidently different. In ESI mode (Figure 4.6b), abundant peaks were at m/z 116.07 (assigned to proline), m/z 132.08 (creatine), m/z 147.11 (lysine), and m/z 154.08 (leucine), which are polar PANC-1 cell metabolites. When the DBDI voltage was switched on to 2.6 kV (Figure 4.6b), polar metabolites including 1-pyrroline (m/z 70.06), pyridine (m/z 80.05), etc., and nonpolar metabolites including proline (m/z 116.07), threonine (m/z 142.05), etc. were detected at the same time.

The above results further confirmed that by adjusting the DBDI voltage, the ESI-DBDI source can be switched to different modes. When the DBDI is turned off, the metabolites in the cells are mainly ionized by the ESI source through proton transfer. Due to the complex environment in the cells, matrix effects, and ion

suppression, the ion yield of less polar and nonpolar metabolites is reduced. Since DBDI is less affected by matrix effects and ion-suppression effect than ESI, and there are many reactive species in the plasma, turning on the DBDI increased the ion yield of less polar and nonpolar metabolites *via* a range of ionization reactions, including proton transfer, charge transfer, electron impact, and Penning ionization. For high-throughput single-cell analysis, on-line infusion of a cell suspension into the hybrid source presented here could be used[34] and an automatic voltage scan, similar to data-independent acquisition in liquid chromatography–mass spectrometry (LC–MS), could be helpful.

4.4 Conclusions

In this study, a hybrid ESI + DBDI ionization source was developed for single-cell analysis. The ESI-DBDI source can be operated in ESI mode and hybrid mode. In ESI mode, polar metabolites are ionized well. In hybrid mode, nonpolar or less nonpolar metabolites exhibit good ionization efficiency. By gradually increasing the DBDI voltage from 0 to 3.2 kV, the classes of ionized metabolites in cells can be shifted from mostly polar, to both polar and apolar, to mainly apolar. This hybrid ESI + DBDI source apparently relies on multiple ionization mechanisms such as proton transfer, charge transfer, and Penning ionization. It can thereby improve the ionization efficiency of metabolites of different polarities, the limit of detection, and the coverage of metabolites, which may contribute to the development of metabolomics at the single-cell level.

4.5 Supporting information

4.5.1 Single-cell sampling
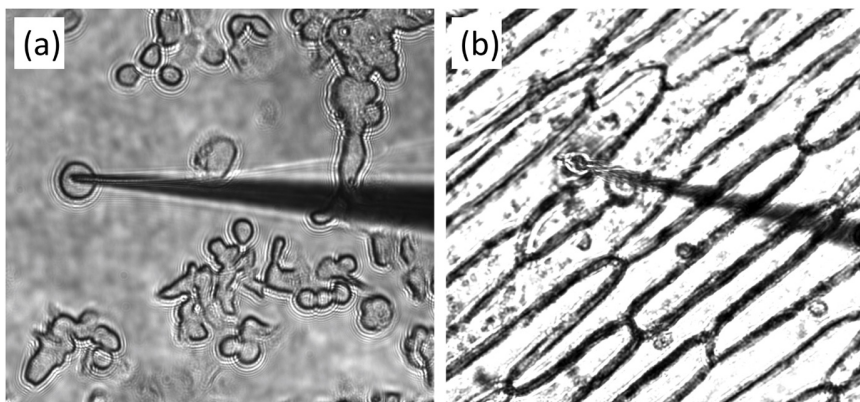
Figure S4.1. Sampling images of (a) PANC-1 cell and (b) onion cell.
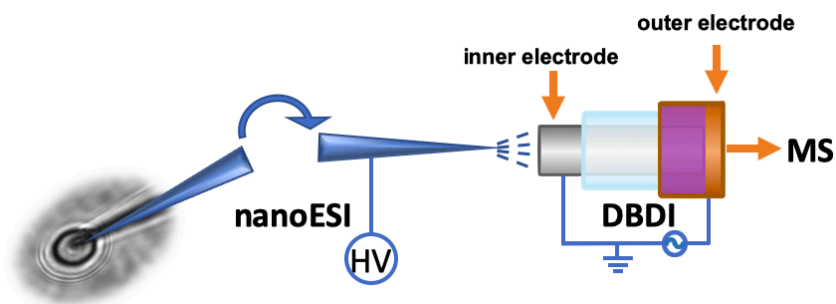
Figure S4.2. The configuration of ESI-DBDI hybrid source.

4.5.2 Effect of the voltage of DBDI source
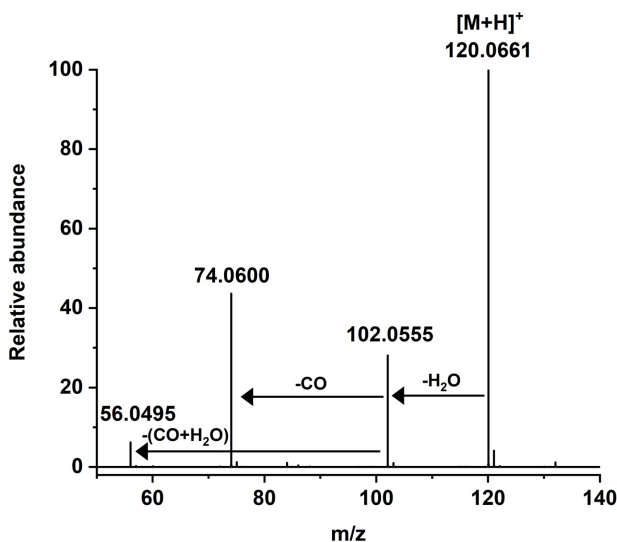
Figure S4.3. Fragment ions mass spectrum of L-threonine. (ESI voltage: 3.5 kV, DBDI voltage: >2.8 kV)

4.5.3 Effect of assistant solvents

As shown in Figures S4.4a, b and c, the ionization efficiencies of the three polar amino acids (L-threonine, L-valine, L-cysteine) dissolved in MeOH/water (1:1) and ACN/DMF (1:1) were higher than that in chlorobenzene/DMF(1:1) in ESI mode and hybrid mode. Compared with the ESI mode, the ionization efficiencies of the three polar amino acids dissolved in MeOH/water (1:1), ACN/DMF (1:1) and chlorobenzene/DMF (1:1) were significantly improved in the hybrid mode. For the non-polar lipid testosterone (Figure S4.4d), when the assistant solvent was MeOH/water (1:1), [M+H]$^+$ and [M+Na]$^+$ could be observed in both ESI mode and hybrid mode, and [M+H]$^+$ were the predominant product ions. Compared with the ESI

mode, the intensity of [M+H]⁺ and [M+Na]⁺ increased after the DBDI source was turned on, and [M+H]⁺ were still the main product ions. When the assistant solvents were ACN/DMF (1:1) and chlorobenzene/DMF (1:1), no obvious product ions were detected in ESI mode and hybrid mode. For the polar lipids 08:0 PC and 12:0 PC (DLPC) (Figures S4.4e and f), [M+H]⁺ and [M+Na]⁺ could be observed in both ESI mode and hybrid mode, [M+H]⁺ were the dominant product ions when the assistant solvent was MeOH/water (1:1). After DBDI was turned on, the intensity of [M+H]⁺ and [M+Na]⁺ were significantly improved. When the assistant solvents were ACN/DMF (1:1) and chlorobenzene/DMF (1:1), although the ionization efficiencies of all product ions were lower than when the assistant solvent was MeOH/water (1:1), the ionization efficiencies of all product ions were improved when DBDI was turned on. We also measured two polycyclic aromatic hydrocarbons (PAHs) (anthracene and fluoranthene). Although they are hardly found in cells, they are non-polar and difficult to ionize, so they were used to evaluate the ability of ESI-DBDI to ionize non-polar compounds. It can be seen from Figures S4.4g and h that when only switched on ESI, the two PAHs dissolved in MeOH/water (1:1), ACN/DMF (1:1) and chlorobenzene/DMF (1:1) had no obvious signals. In hybrid mode, when the assistant solvent was chlorobenzene/DMF (1:1), the ionization efficiencies of anthracene and fluoranthene were higher than when the assistant solvent was MeOH, and [M]⁺• was the main product ions. When the assistant solvent was ACN, there were no obvious signals. Based on the above results, both polar compounds and non-polar compounds have good ionization efficiencies when MeOH/water (1:1) was used as the assistant solvent, so MeOH/water (1:1) was selected as the assistant solvent for subsequent experiments.
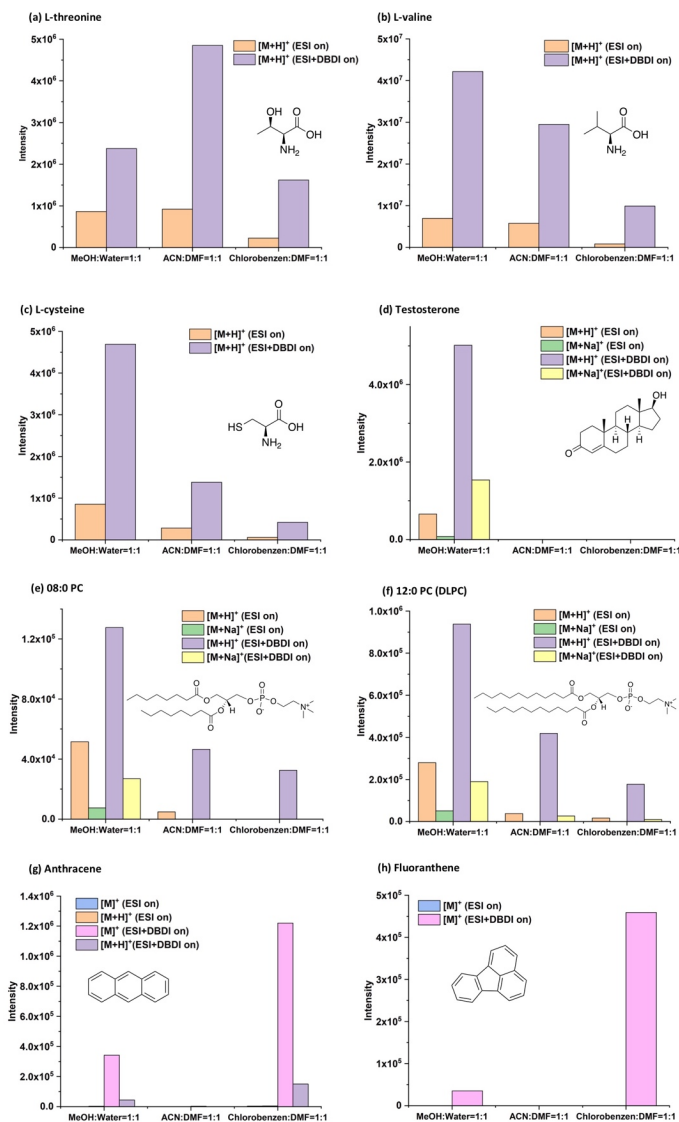
Figure S4.4. Effect of assistant solvents (MeOH: water=1:1, ACN: DMF=1:1, Chlorobenzene: DMF=1:1) on the intensity of 8 compounds with different polarities. (a) L-threonine, (b) L-valine, (c) L-cysteine, (d) testosterone, (e) 08:0 PC, (f) 12:0 PC

(DLPC), (g) anthracene and (h) fluoranthene. (ESI voltage: 3.5 kV, DBDI voltage: 2.6 kV)

4.5.4. Single-cell detection

Table S4.1. Putative metabolites from a single onion cell ionized by ESI source.

	ESI				
	Chemical name	**Chemical formula**	**Theoretical m/z**	**Measured m/z**	**PPM**
1	Glucose (DP1)	$C_6H_{12}O_6(+Na^+)$	203.0532	203.0525	3.45
2	(2R,2'S)-Isobuteine	$C_7H_{13}NO_4S(+H-H_2O^+)$	190.0538	190.0529	4.74
		$C_7H_{13}NO_4S(+H^+)$	208.0644	208.0637	3.36
3	(R)C(R)S-S-Propylcysteine sulfoxide (propiin)	$C_6H_{13}NO_3S(+H^+)$	180.069	180.0694	2.22
4	(S)C(S)S-S-Methylcysteine sulfoxide (Methiin)	$C_4H_9NO_3S(+H^+)$	152.0381	152.0375	3.95
5	1-(1-Propenylsulfinyl)propyl propyl disulfide	$C_9H_{18}OS_3(+H^+)$	239.0598	239.0591	2.93
6	1-Propenyl 1-(1-propenylsulfinyl)propyl disulfide	$C_9H_{16}OS_3(+H^+)$	237.0441	237.0437	1.69
7	2-Isopropyl-6-methoxypyrazine	$C_8H_{12}N_2O(+Na^+)$	175.0847	175.0854	4.00
8	2-Methyl-1-propenethiol	$C_5H_{10}S(+H^+)$	103.0582	103.0581	0.97
9	5´-O-b-Glucosylpyridoxin	$C_{14}H_{21}NO_8(+H^+)$	332.1345	332.1332	3.91
10	Adenosine	$C_{10}H_{13}N_5O_4(+H^+)$	268.1046	268.1044	0.75
11	Ajoene	$C_9H_{14}OS_3(+H^+)$	235.0285	235.028	2.13

12	Arginine	$C_6H_{14}N_4O_2(+H-H_2O^+)$	157.1089	157.1084	3.18
		$C_6H_{14}N_4O_2(+H^+)$	175.1195	175.119	2.86
13	Asparagine	$C_4H_8N_2O_3(+H^+)$	133.0613	133.0607	4.51
14	Butyl isopropyl disulfide	$C_7H_{16}S_2(+H^+)$	165.0772	165.0773	0.61
15	Citrullin	$C_6H_{13}N_3O_3(+H-H_2O^+)$	158.093	158.0925	3.16
16	Cycloalliin	$C_6H_{11}NO_3S(+H^+)$	178.0538	178.0533	2.81
		$C_6H_{11}NO_3S(+Na^+)$	200.0357	200.035	3.50
17	Cys(Prop-1-enyl) (Deoxyisoalliin)	$C_6H_{11}NO_2S(+H^+)$	162.0589	162.0582	4.32
18	Cys(Propyl) (Deoxypropiin)	$C_6H_{13}NO_2S(+H^+)$	164.0745	164.0741	2.44
19	g-Aminobutyric acid	$C_4H_9NO_2(+H^+)$	104.0712	104.0705	6.73
20	g-Glu-Cys(Propyl) S-Oxide	$C_{11}H_{20}N_2O_6S(+H-H_2O^+)$	291.1015	291.1011	1.37
21	gamma-Glutamylglutamine	$C_{10}H_{17}N_3O_6(+H-H_2O^+)$	258.109	258.1101	4.26
22	gamma-Glutamylphenylalanine	$C_{14}H_{18}N_2O_5(+H^+)$	295.1294	295.1286	2.71
23	Glutamine	$C_5H_9NO_4(+H^+)$	147.077	147.0763	4.76
		$C_5H_9NO_4(+Na^+)$	169.0589	169.0585	2.37
24	Histidine	$C_6H_9N_3O_2(+H^+)$	156.0773	156.0766	4.48
25	Leucine	$C_6H_{13}NO_2(+H^+)$	132.1025	132.1018	5.30
26	Lysine	$C_6H_{14}N_2O_2(+H^+)$	147.1133	147.1126	4.76
27	Methyl 1-(1-propenylthio)propyl disulfide	$C_7H_{14}S_3(+Na^+)$	217.0155	217.0124	14.28

28	Methyl 1-(methylthio)propyl disulfide	$C_5H_{12}S_3(+H^+)$	169.0179	169.0199	11.83
		$C_5H_{12}S_3(+Na^+)$	190.9998	190.9966	16.75
29	N^a-(Hydroxysuccinyl)arginine[c]	$C_{10}H_{18}N_4O_6(+H^+)$	291.1305	291.13	1.72
30	N^w-Methyl-Arg	$C_7H_{16}N_4O_2(+H^+)$	189.1352	189.1345	3.70
31	PC(34:0)/ PE(37:0)	$C_{42}H_{84}NO_8P(+Na^+)$	784.5827	784.5826	0.13
32	PC(34:2)/ PE(37:2)	$C_{42}H_{80}NO_8P$ (+H$^+$)	758.5694	758.5703	1.19
33	PC(36:4)	$C_{44}H_{80}NO_8P$ (+H$^+$)	782.5694	782.5703	1.15
34	PE-NMe(38:9)	$C_{44}H_{70}NO_8P$ (+H-H$_2$O$^+$)	754.4812	754.4794	2.39
35	PE(40:8)	$C_{45}H_{74}NO_8P$ (+H-2H$_2$O$^+$)	752.5025	752.5083	7.71
36	PE(42:9)	$C_{47}H_{76}NO_8P$ (+H-H$_2$O$^+$)	796.5282	796.5262	2.51
37	PE(44:10)	$C_{49}H_{78}NO_8P$ (+H-H$_2$O$^+$)	822.5438	822.5388	6.08
38	PE(44:11)	$C_{49}H_{76}NO_8P$ (+H-H$_2$O$^+$)	820.5282	820.5263	2.32
39	Phenylalanine	$C_9H_{11}NO_2(+H^+)$	166.0868	166.0862	3.61
40	Phosphorylcholine	$C_5H_{14}NO_4P(+H^+)$	184.0739	184.0732	3.80
41	Pipecolic acid	$C_6H_{11}NO_2(+H^+)$	130.0868	130.0862	4.61
42	Proline	$C_5H_9NO_2(+H^+)$	116.0712	116.0706	5.17
43	Pyroglutamic acid	$C_5H_7NO_3(+H^+)$	130.0504	130.0498	4.61
44	Serine	$C_3H_7NO_3$ (+H-H$_2$O$^+$)	88.0399	88.0393	6.82

45	Sucrose (DP2)	$C_{12}H_{22}O_{11}(+Na^+)$	365.106	365.1052	2.19
46	Threonine	$C_4H_9NO_3(+H-2H_2O^+)$	84.0449	84.0443	7.14
		$C_4H_9NO_3(+H-H_2O^+)$	102.0555	102.055	4.90
		$C_4H_9NO_3(+H^+)$	120.0661	120.0654	5.83
47	Tryptophan	$C_{11}H_{12}N_2O_2(+H^+)$	205.0977	205.097	3.41
48	Tyramine	$C_8H_{11}NO(+H-H_2O^+)$	120.0813	120.0808	4.16
49	Tyrosine	$C_9H_{11}NO_3(+H^+)$	182.0817	182.0812	2.75
50	Valine	$C_5H_{11}NO_2(+H^+)$	118.0868	118.0862	5.08

Table S4.2. Putative metabolites from a single onion cell ionized by ESI-DBDI source.

ESI-DBDI					
	Chemical name	**Chemical formula**	**Theoretical m/z**	**Measured m/z**	**PPM**
1	Glucose (DP1)	$C_6H_{12}O_6(+H-2H_2O^+)$	145.0501	145.0494	4.83
		$C_6H_{12}O_6 (+H-H_2O^+)$	163.0607	163.0601	3.68
		$C_6H_{12}O_6(+H^+)$	181.0712	181.0707	2.76
		$C_6H_{12}O_6(+Na^+)$	203.0532	203.0525	3.45
2	(E,E)-Di-1-propenyl disulfide	$C_6H_{10}S_2(+H^+)$	147.0296	147.0302	4.08
3	(R)C(R)S-S-Propylcysteine sulfoxide (propiin)	$C_6H_{13}NO_3S(+H^+)$	180.069	180.0694	2.22

4	(S)C(S)S-S-Methylcysteine sulfoxide (Methiin)	$C_4H_9NO_3S(+H^+)$	152.0381	152.0375	3.95
5	(Z)-4-Hexenal	$C_6H_{10}O(+H-H_2O^+)$	81.0704	81.0698	7.40
		$C_6H_{10}O(+H^+)$	99.0809	99.0803	6.06
6	(Z)-S-1-Propenyl methanesulfinothioate	$C_4H_8OS_2(+H-H_2O^+)$	118.9989	118.9982	5.88
		$C_4H_8OS_2(+H^+)$	137.0094	137.0089	3.65
7	1-(1-Propenylthio)propyl propyl disulfide	$C_9H_{18}S_3(+H^+)$	223.0648	223.0637	4.93
8	1-(Methylsulfinyl)propyl propyl disulfide	$C_7H_{16}OS_3(+Na^+)$	235.0261	235.0277	6.81
9	1-Propenyl 1-(1-propenylsulfinyl)propyl disulfide	$C_9H_{16}OS_3(+H^+)$	237.0441	237.0437	1.69
10	1-Propenyl propyl disulfide	$C_6H_{12}S_2(+H^+)$	149.0459	149.0455	2.68
11	1-Propenyl propyl sulfide	$C_6H_{12}S^{+\bullet}$	116.0659	116.0654	4.31
		$C_6H_{12}S(+H^+)$	117.0738	117.0732	5.12
12	1,1-Diethoxyethane	$C_6H_{14}O_2(+H-2H_2O^+)$	83.086	83.0855	6.02
		$C_6H_{14}O_2(+H-H_2O^+)$	101.0966	101.096	5.93
13	1,2,3-Trithiane	$C_3H_6S_3(+H^+)$	138.971	138.9703	5.04
14	2-Isopropyl-3-oxosuccinate	$C_7H_{10}O_5(+H^+)$	175.0607	175.06	4.00
15	2-Isopropyl-6-methoxypyrazine	$C_8H_{12}N_2O(+Na^+)$	175.0847	175.0854	4.00
16	2-Tridecanone	$C_{13}H_{26}O(+H^+)$	199.2062	199.2053	4.52

17	2-Vinyl-4H-1,3-dithiine	$C_6H_8S_2(+H^+)$	145.0146	145.0139	4.83
18	2,4-Dimethylfuran	$C_6H_8O(+H-H_2O^+)$	79.0548	79.0542	7.59
		$C_6H_8O(+H^+)$	97.0653	97.0648	5.15
19	2,4,6-Triethyl-1,3,5-oxadithiane	$C_9H_{18}OS_2(+H^+)$	189.0772	189.0756	8.46
20	2,4,6-Triethyl-1,3,5-trioxane	$C_9H_{18}O_3(+H-H_2O^+)$	157.1229	157.1222	4.46
		$C_9H_{18}O_3(+H^+)$	175.1334	175.1327	4.00
21	2,4,6-Trimethyl-1,3,5-dioxathiane	$C_6H_{12}O_2S(+H-H_2O^+)$	131.053	131.0524	4.58
		$C_6H_{12}O_2S(+H^+)$	149.0636	149.0629	4.70
22	2,5-Dimethylthiophene	$C_6H_8S^{+\bullet}$	112.0346	112.0341	4.46
		$C_6H_8S(+H^+)$	113.0425	113.0419	5.31
23	3-(Methylthio)-1-propene	$C_4H_8S(+H^+)$	89.0425	89.0421	4.49
24	3-Mercapto-2-methylpentanol	$C_6H_{14}OS(+H-H_2O^+)$	117.0738	117.0731	5.98
25	3-Methoxytyramine	$C_9H_{13}NO_2(+H-H_2O^+)$	150.0919	150.0915	2.67
26	5-Hydroxymethyl-2-furancarboxaldehyde	$C_6H_6O_3(+H-H_2O^+)$	109.029	109.0283	6.42
		$C_6H_6O_3(+H^+)$	127.0395	127.0389	4.72
27	Ajoene	$C_9H_{14}OS_3(+H^+)$	235.0285	235.028	2.13
28	Alanine	$C_3H_7NO_2(+H^+)$	90.0555	90.0548	7.77
29	Allitridin	$C_6H_{10}S_3(+H^+)$	179.0023	179.0022	0.56
30	Allixin	$C_{12}H_{18}O_4(+H-H_2O^+)$	209.1178	209.1171	3.35
		$C_{12}H_{18}O_4(+H^+)$	227.1283	227.1273	4.40
31	Arginine	$C_6H_{14}N_4O_2(+H^+)$	175.1195	175.119	2.86

32	Asparagine	$C_4H_8N_2O_3(+H^+)$	133.0613	133.0607	4.51
33	Bissulfine	$C_6H_{10}O_2S_2(+H-H_2O^+)$	161.0094	161.0089	3.11
		$C_6H_{10}O_2S_2(+H^+)$	179.0201	179.0195	3.35
34	Butyl isopropyl disulfide	$C_7H_{16}S_2(+H^+)$	165.0772	165.0773	0.61
35	Cibulins	$C_3H_8OS(+H^+)$	93.0374	93.0368	6.45
36	Citric acid	$C_6H_8O_7(+H^+)$	193.0348	193.0349	0.52
37	Cycloalliin	$C_6H_{11}NO_3S(+H^+)$	178.0538	178.0533	2.81
38	Cys(Prop-1-enyl) (Deoxyisoalliin)	$C_6H_{11}NO_2S(+H-H_2O^+)$	144.0483	144.0478	3.47
		$C_6H_{11}NO_2S(+H^+)$	162.0589	162.0582	4.32
39	Cys(Propyl) (Deoxypropiin)	$C_6H_{13}NO_2S(+H^+)$	164.0745	164.0741	2.44
40	Di-1-propenyl sulfide	$C_6H_{10}S(+H^+)$	115.0581	115.0575	5.21
41	Dipropyl trisulfide	$C_6H_{14}S_3(+H^+)$	183.0336	183.031	14.21
42	Ethyl isopropyl disulfide	$C_5H_{12}S_2(+Na^+)$	159.0278	159.0287	5.66
43	Furfuryl acetate	$C_7H_8O_3(+H-H_2O^+)$	123.0446	123.0443	2.44
		$C_7H_8O_3(+H^+)$	141.0552	141.0545	4.96
44	gamma-Glutamylalanine	$C_8H_{14}N_2O_5(+H-2H_2O^+)$	183.0769	183.0778	4.92
45	Glutamine	$C_5H_9NO_4(+H^+)$	147.077	147.0763	4.76
46	Histidine	$C_6H_9N_3O_2(+H^+)$	156.0773	156.0766	4.48
47	Leucine	$_6H_{13}NO_2 (+H-H_2O^+)$	114.0918	114.0913	4.38
		$C_6H_{13}NO_2(+H^+)$	132.1025	132.1018	5.30
48	Lysine	$C_6H_{14}N_2O_2(+H^+)$	147.1133	147.1126	4.76

49	Methyl 1-(1-propenylthio)propyl disulfide	$C_7H_{14}S_3(+Na^+)$	217.0155	217.0124	14.28
50	Methyl 2,4,6-trihydroxybenzoate	$C_8H_8O_5(+H-2H_2O^+)$	149.0239	149.0232	4.70
51	N^w-Methyl-Arg	$C_7H_{16}N_4O_2(+H^+)$	189.1352	189.1345	3.70
52	Pantothenic acid	$C_9H_{17}NO_5(+H-2H_2O^+)$	184.0974	184.0968	3.26
		$C_9H_{17}NO_5(+H-H_2O^+)$	202.1079	202.1073	2.97
		$C_9H_{17}NO_5(+H^+)$	220.1185	220.1177	3.63
53	PC(34:0)/ PE(37:0)	$C_{42}H_{84}NO_8P(+Na^+)$	784.5827	784.5826	0.13
54	PC(34:2)/ PE(37:2)	$C_{42}H_{80}NO_8P(+H^+)$	758.5694	758.5703	1.19
55	PC(36:4)	$C_{44}H_{80}NO_8P(+H^+)$	782.5694	782.5703	1.15
56	PE-NMe(38:9)	$C_{44}H_{70}NO_8P(+H-H_2O^+)$	754.4812	754.4794	2.39
57	PE(40:8)	$C_{45}H_{74}NO_8P(+H-2H_2O^+)$	752.5025	752.5083	7.71
58	PE(42:9)	$C_{47}H_{76}NO_8P(+H-H_2O^+)$	796.5282	796.5262	2.51
59	PE(44:10)	$C_{49}H_{78}NO_8P(+H-H_2O^+)$	822.5438	822.5388	6.08
60	PE(44:11)	$C_{49}H_{76}NO_8P(+H-H_2O^+)$	820.5282	820.5263	2.32
61	Phenylalanine	$C_9H_{11}NO_2(+H^+)$	166.0868	166.0862	3.61
62	Pipecolic acid	$C_6H_{11}NO_2(+H^+)$	130.0868	130.0862	4.61
63	Proline	$C_5H_9NO_2(+H^+)$	116.0712	116.0706	5.17
64	Propyl 1-(propylsulfinyl)propyl disulfide	$C_9H_{20}OS_3(+H-H_2O^+)$	223.0649	223.0665	7.17

65	Pyridoxin	$C_8H_{11}NO_3$(+H-H_2O^+)	152.0719	152.0712	4.60
		$C_8H_{11}NO_3$(+H$^+$)	170.0817	170.0807	5.88
66	Pyroglutamic acid	$C_5H_7NO_3$(+H$^+$)	130.0504	130.0498	4.61
67	R-Propyl 1-propenesulfinothioate	$C_6H_{12}OS_2$(+H$^+$)	165.0408	165.0403	3.03
68	S-Methyl methanesulfinothioate	$C_2H_6OS_2$(+H$^+$)	110.9938	110.9932	5.41
69	S-Propyl 1-propanesulfinothioate	$C_6H_{14}OS_2$(+H-H_2O^+)	149.0459	149.0459	0.00
		$C_6H_{14}OS_2$(+H$^+$)	167.0564	167.056	2.39
70	S-Propyl thiosulfate	$C_3H_8O_3S_2$(+H-$2H_2O^+$)	120.9781	120.9776	4.13
71	S-Propyl-L-cysteine	$C_6H_{13}NO_2S_2$(+H$^+$)	196.0466	196.0459	3.57
72	Serine	$C_3H_7NO_3$ (+H-H_2O^+)	88.0399	88.0393	6.82
73	Sucrose (DP2)	$C_{12}H_{22}O_{11}$(+H-H_2O^+)	325.1135	325.1129	1.85
74	Thial-1-Propene-1-thiol S-oxide	C_3H_6OS(+H$^+$)	91.0218	91.0212	6.59
75	Threonine	$C_4H_9NO_3$(+H-$2H_2O^+$)	84.0449	84.0443	7.14
		$C_4H_9NO_3$(+H-H_2O^+)	102.0555	102.055	4.90
		$C_4H_9NO_3$(+H$^+$)	120.0661	120.0654	5.83
76	Tiglic aldehyde	C_5H_8O(+H$^+$)	85.0653	85.0647	7.05
77	Trigonelline	$C_7H_8NO_2^{+\bullet}$	138.0555	138.0548	5.07
		$C_7H_8NO_2$(+H-$2H_2O^+$)	103.0422	103.0424	1.94
78	Tryptophan	$C_{11}H_{12}N_2O_2$(+H$^+$)	205.0977	205.097	3.41

79	Tsibulin 1	$C_{13}H_{22}O_2(+H-2H_2O^+)$	175.1487	175.148	4.00
		$C_{13}H_{22}O_2(+H-H_2O^+)$	193.1592	193.1586	3.11
		$C_{13}H_{22}O_2 (+H^+)$	211.1698	211.1692	2.84
80	Tsibulin 2	$C_{11}H_{18}O_2(+H^+)$	183.1385	183.1379	3.28
81	Tyramine	$C_8H_{11}NO(+H-H_2O^+)$	120.0813	120.0808	4.16
82	Tyrosine	$C_9H_{11}NO_3(+H^+)$	182.0817	182.0812	2.75
83	Valine	$C_5H_{11}NO_2$ (+H-H_2O^+)	100.0762	100.0753	8.99
		$C_5H_{11}NO_2(+H^+)$	118.0868	118.0862	5.08
84	xi-1-(Propylthio)-1-propanethiol	$C_6H_{14}S_2(+Na^+)$	173.0434	173.0444	5.78
85	xi-2-Methyl-1,3-oxathiane	$C_5H_{10}OS(+H-H_2O^+)$	101.0425	101.0418	6.93
86	Zwiebelane B	$C_6H_{10}OS_2(+H^+)$	163.0251	163.0245	3.68

Table S4.3. Putative metabolites from a single PANC-1 cell ionized by ESI source.

ESI					
	Chemical name	**Chemical formula**	**Theoretical m/z**	**Measured m/z**	**PPM**
1	1-Methylnaphthalene	$C_{11}H_{10}(+H-H_2O)$	125.0756	125.0748	6.16
2	2-Hexenoylcholine	$C_{11}H_{22}NO_2(+H^+)$	200.1651	200.1658	3.65
3	Alanine	$C_3H_7NO_2(+H^+)$	90.055	90.0551	1.22
4	APC	$C_{33}H_{38}N_4O_8(+Na^+)$	641.2582	641.2582	0.00
5	Arginine	$C_6H_{14}N_4O_2(+H^+)$	175.119	175.1192	1.20

6	CE(20:2)	$C_{47}H_{80}O_2(+H-2H_2O)$	641.6031	641.6033	0.23
7	Creatine	$C_4H_9N_3O_2(+H^+)$	132.0768	132.0770	1.67
		$C_4H_9N_3O_2(+Na^+)$	154.0587	154.0589	1.23
8	Creatinine	$C_4H_7N_3O(+Na^+)$	136.0481	136.0482	0.66
9	Ectoine	$C_6H_{10}N_2O_2(+H-H_2O)$	125.0715	125.0713	1.28
10	Glutamine	$C_5H_{10}N_2O_3(+Na^+)$	169.0584	169.0586	1.42
11	Glycerophosphorylcholine (GPC)	$C_8H_{20}NO_6P(+Na^+)$	280.092	280.0926	2.14
12	Leucine	$C_6H_{13}NO_2(+H^+)$	132.1019	132.1021	1.21
		$C_6H_{13}NO_2(+Na^+)$	154.0838	154.0840	1.43
13	Lysine	$C_6H_{13}NO_2(+H^+)$	147.1128	147.1130	1.56
14	PA(30:1)	$C_{33}H_{63}O_8P(+Na^+)$	641.4153	641.4091	9.67
15	PC(30:1)/PE(33:1)	$C_{38}H_{74}NO_8P(+Na^+)$	726.5044	726.5055	1.49
16	PC(32:1)	$C_{40}H_{78}NO_8P(+H^+)$	732.5538	732.5543	0.63
17	PC(32:3)/ PE(35:3)	$C_{40}H_{74}NO_8P(+H^+)$	728.5211	728.5207	0.56
18	PC(34:1)/ PE(37:1)	$C_{42}H_{82}NO_8P(+H^+)$	760.5851	760.5861	1.33
		$C_{42}H_{82}NO_8P(+H-H_2O)$	742.5751	742.5753	0.31
19	PC(34:2)/ PE(37:2)	$C_{42}H_{80}NO_8P(+H-2H_2O)$	740.5595	740.5590	0.66
		$C_{42}H_{80}NO_8P(+H^+)$	758.5694	758.5713	2.52
		$C_{42}H_{80}NO_8P(+Na^+)$	780.5514	780.5514	0.01
20	PC(34:3)	$C_{42}H_{78}NO_8P(+H^+)$	756.5538	756.5546	1.10
21	PC(34:4)/ PE(37:4)	$C_{42}H_{76}NO_8P(+H^+)$	754.5381	754.5388	0.87
22	PC(34:5)/ PE(37:5)	$C_{42}H_{74}NO_8P(+H^+)$	752.5225	752.5232	0.97
23	PC(36:2)	$C_{44}H_{84}NO_8P(+H-H_2O)$	768.5908	768.5916	1.04

		$C_{44}H_{84}NO_8P(+H^+)$	786.6007	786.6044	4.64
		$C_{44}H_{84}NO_8P(+Na^+)$	808.5827	808.5835	0.99
		$C_{44}H_{84}NO_8P(+K^+)$	824.5566	824.5567	0.07
24	PC(36:3)	$C_{44}H_{82}NO_8P(+H-H_2O)$	766.5751	766.5761	1.32
25	PC(36:4)	$C_{44}H_{80}NO_8P(+H^+)$	782.5694	782.5717	2.94
26	PC(38:6)/ PE(37:2)	$C_{46}H_{80}NO_8P(+H^+)$	806.5694	806.5710	2.01
27	PC(40:5)	$C_{48}H_{86}NO_8P(+H-2H_2O)$	800.5964	800.6019	6.92
28	PC(O-30:0)	$C_{38}H_{78}NO_7P(+Na^+)$	714.5408	714.5423	2.10
29	PC(P-32:0)/PC(O-32:1)	$C_{40}H_{80}NO_7P(+H^+)$	718.5745	718.5766	2.91
		$C_{40}H_{80}NO_7P(+K^+)$	756.5304	756.5305	0.15
30	PE(38:4)	$C_{44}H_{79}O_{10}P(+H^+)$	799.5484	799.5487	0.40
31	PE(40:8)	$C_{45}H_{74}NO_8P(+H-H_2O)$	770.5125	770.5115	1.34
32	PE(44:8)	$C_{47}H_{78}NO_8P(+H-H_2O)$	798.5438	798.5439	0.09
33	PE(44:9)	$C_{47}H_{76}NO_8P(+H-H_2O)$	796.5282	796.5283	0.13
34	PG(34:1)	$C_{40}H_{77}O_{10}P(+Na^+)$	771.5147	771.5144	0.38
35	Phosphorylcholine	$C_5H_{15}NO_4P(+Na^+)$	206.0558	206.0555	1.36
36	Piperidine	$C_5H_{11}N(+H^+)$	86.0964	86.0966	2.79
37	Proline	$C_5H_9NO_2(+H^+)$	116.0706	116.0709	2.15
		$C_5H_9NO_2(+Na^+)$	138.0525	138.0526	0.87
38	SM(d39:2)	$C_{44}H_{87}N_2O_6P(+K^+)$	809.5933	809.5896	4.56
39	Spermidine	$C_7H_{19}N_3(+H^+)$	146.1652	146.1656	3.01
40	Valine	$C_5H_{11}NO_2(+H^+)$	118.0863	118.0865	2.03
		$C_5H_{11}NO_2(+Na^+)$	140.0682	140.0682	0.07

Table S4.4. Putative metabolites from a single PANC-1 cell ionized by ESI-DBDI source.

	Chemical name	Chemical formula	Theoretical m/z	Measured m/z	PPM
			ESI-DBDI		
1	(3R,7R)-1,3,7-Octanetriol	$C_8H_{18}O_3(+H^+)$	163.1329	163.1331	1.29
2	(S)-Spinacine	$C_7H_9N_3O_2^{+\bullet}$	167.0695	167.0682	7.54
3	(Z)-1,3-Octadiene	$C_8H_{12}(+H^+)$	109.1012	109.1014	2.11
4	1-Methyl-4-nitroimidazole	$C_4H_5N_3O_2^{+\bullet}$	127.0382	127.0391	6.69
5	1-Methylhistidine/3-Methylhistidine	$C_7H_{11}N_3O_2^{+\bullet}$	169.0851	169.0864	7.75
6	1-Methylnaphthalene	$C_{11}H_{10}(+H-H_2O)$	125.0756	125.0748	6.16
7	1-Methylpyrrolinium	$C_5H_{10}N^{+\bullet}$	84.0813	84.0809	5.23
8	1-Pyrroline	$C_4H_7N(+H^+)$	70.0651	70.0652	2.00
9	1-Pyrroline-5-carboxylic acid	$C_5H_7NO_2(+H^+)$	114.055	114.0552	1.67
10	2-Amino-a-carboline	$C_{11}H_9N_3^{+\bullet}$	183.0796	183.0786	5.35
11	2-Benzoxazolol	$C_7H_5NO_2^{+\bullet}$	135.032	135.0321	1.04
12	2-Keto-6-acetamidocaproate	$C_8H_{13}NO_4(+H-H_2O)$	170.0818	170.0815	1.53
13	2-Methylfuran	$C_5H_6O(+H^+)$	83.0491	83.0494	3.01
14	2-Oxoarginine	$C_6H_{11}N_3O_3^{+\bullet}$	173.08	173.0808	4.62
15	3-Hydroxyheptanoylcarnitine	$C_{14}H_{27}NO_5(+H-2H_2O)$	254.1762	254.1760	0.90
16	3-Hydroxyhexanoylcarnitine	$C_{13}H_{25}NO_5(+H^+)$	217.1071	217.1074	1.15
17	3-Isoxazolidinone	$C_3H_5NO_2(+H^+)$	88.0393	88.0394	1.48

18	3-Methylcyclopentene	$C_6H_{10}(+H^+)$	83.0855	83.0857	2.17
19	4-(Nitrosoamino)-1-(3-pyridinyl)-1-butanone	$C_9H_{11}N_3O_2^{+\bullet}$	193.0851	193.0839	6.27
20	4-Guanidinobutanoic acid	$C_5H_{11}N_3O_2^{+\bullet}$	145.0851	145.0861	6.62
21	4-Hydroxy-2-butenoic acid gamma-lactone	$C_4H_4O_2(+H^+)$	85.0284	85.0286	2.12
22	4-Hydroxydebrisoquine	$C_{10}H_{13}N_3O^{+\bullet}$	191.1059	191.1046	6.85
23	5-[(5-Methyl-2-thienyl)methylene]-2(5H)-furanone	$C_{10}H_8O_2S^{+\bullet}$	192.0245	192.0247	1.09
24	6-Thioinosinic acid	$C_{10}H_{12}N_4O_4S(+H-2H_2O)$	249.0452	249.0463	4.50
25	8,8-Diethoxy-2,6-dimethyl-2-octanol	$C_{14}H_{30}O_3(+H-H_2O)$	229.2168	229.2168	0.04
26	a-Methylstyrene	$C_9H_{10}(+H^+)$	119.0855	119.0858	2.27
27	Acetylcholine	$C_7H_{16}NO_2^{+\bullet}$	146.1181	146.1177	2.94
28	Acetylglycine	$C_4H_7NO_3(+H^+)$	118.0499	118.0502	2.88
29	Acetylisoniazid	$C_8H_9N_3O_2^{+\bullet}$	179.0695	179.0683	6.98
30	Alanine	$C_3H_7NO_2(+H^+)$	90.055	90.0551	1.22
31	APC	$C_{33}H_{38}N_4O_8(+Na^+)$	641.2582	641.2582	0.00
32	Arginine	$C_6H_{14}N_4O_2^{+\bullet}$	174.1117	174.1128	6.55
		$C_6H_{14}N_4O_2(+H^+)$	175.119	175.1192	1.20
33	Benzothiazole	$C_7H_5NS(+H^+)$	136.0215	136.0216	0.88
34	Betaine aldehyde	$C_5H_{12}NO^{+\bullet}$	102.0919	102.0915	4.41
35	Butyl butyryllactate	$C_{11}H_{20}O_4(+H-H_2O)$	199.1335	199.1333	1.05
36	CE(20:2)	$C_{47}H_{80}O_2(+H-2H_2O)$	641.6031	641.6033	0.23
37	Choline	$C_5H_{14}NO^{+\bullet}$	104.1075	104.1071	3.55

38	Citrulline	$C_6H_{13}N_3O_3^{+\bullet}$	175.0957	175.0972	8.40
39	Creatine	$C_4H_9N_3O_2^{+\bullet}$	131.0695	131.0704	6.87
		$C_4H_9N_3O_2(+H^+)$	132.0768	132.0770	1.67
		$C_4H_9N_3O_2(+Na^+)$	154.0587	154.0589	1.23
40	Creatinine	$C_4H_7N_3O^{+\bullet}$	113.0589	113.0600	9.29
		$C_4H_7N_3O(+H^+)$	114.0662	114.0663	0.53
		$C_4H_7N_3O(+Na^+)$	136.0481	136.0482	0.66
41	Cymenene	$C_{10}H_{12}(+H^+)$	133.1012	133.1012	0.23
42	Cysteinyl-Cysteine	$C_6H_{12}N_2O_3S_2(+H^+)$	225.0362	225.0348	6.40
43	Cytosine	$C_4H_5N_3O^{+\bullet}$	111.0433	111.0442	8.29
44	Diethylcarbamazine	$C_{10}H_{21}N_3O^{+\bullet}$	199.1685	199.1694	4.37
45	Diethylthiophosphate	$C_4H_{11}O_3PS(+H-2H_2O)$	135.004	135.0030	7.70
46	Dimethylguanidino valeric acid	$C_8H_{15}N_3O_3^{+\bullet}$	201.1113	201.1123	4.72
47	Dimethylurea	$C_3H_8N_2O(+H^+)$	89.0709	89.0712	2.92
48	Ectoine	$C_6H_{10}N_2O_2(+H-H_2O)$	125.0715	125.0713	1.28
49	Gabapentin	$C_9H_{17}NO_2(+H^+)$	172.1332	172.1336	2.38
50	Glutamine	$C_5H_{10}N_2O_3(+H^+)$	147.0764	147.0767	1.97
		$C_5H_{10}N_2O_3(+Na^+)$	169.0584	169.0586	1.42
51	Glycerophosphorylcholine (GPC)	$C_8H_{20}NO_6P(+Na^+)$	280.092	280.0926	2.14
52	Guanidinosuccinic acid	$C_5H_9N_3O_4(+H^+)$	176.0666	176.0663	1.87
53	Guanidoacetic acid	$C_3H_7N_3O_2^{+\bullet}$	117.0538	117.0550	9.82
54	Histamine	$C_5H_9N_3^{+\bullet}$	111.0796	111.0807	9.45
55	Histidinal	$C_6H_9N_3O^{+\bullet}$	139.0746	139.0756	7.12
56	Homoarecoline	$C_9H_{15}NO_2(+H^+)$	170.1176	170.1181	3.17

57	L-Carnitine	$C_7H_{15}NO_3(+H^+)$	162.1125	162.1127	0.93
58	L-Histidine	$C_6H_9N_3O_2^{+\bullet}$	155.0695	155.0681	8.77
		$C_6H_9N_3O_2(+H^+)$	156.0768	156.0770	1.22
		$C_6H_9N_3O_2(+Na^+)$	178.0587	178.0588	0.34
59	L-Histidinol	$C_6H_{11}N_3O^{+\bullet}$	141.0902	141.0912	7.37
60	L-Threonine	$C_4H_9NO_3(+H^+)$	120.0655	120.0658	2.33
61	Leucine	$C_6H_{13}NO_2(+H^+)$	132.1019	132.1021	1.21
		$C_6H_{13}NO_2(+Na^+)$	154.0838	154.0840	1.43
62	Lysine	$C_6H_{14}N_2O_2(+H^+)$	147.1128	147.1130	1.56
63	Methionyl-Methionine	$C_{10}H_{20}N_2O_3S_2(+H-2H_2O)$	245.0788	245.0787	0.41
64	Methylcyclohexadiene	$C_7H_{10}(+H^+)$	95.0855	95.0858	2.84
65	Methylcytosine	$C_5H_7N_3O^{+\bullet}$	125.0589	125.0601	9.52
66	Methylhistamine	$C_6H_{11}N_3O^{+\bullet}$	125.0953	125.0963	7.67
67	N-Acetylhistamine	$C_7H_{11}N_3O^{+\bullet}$	153.0902	153.0913	7.38
68	N-Carbamoylputrescine	$C_5H_{13}N_3O^{+\bullet}$	131.1059	131.1070	8.70
69	N-Methylpyridinium	$C_6H_8N^{+\bullet}$	94.0651	94.0653	2.02
70	N1,N8-Diacetylspermidine	$C_{11}H_{23}N_3O_2^{+\bullet}$	229.179	229.1802	5.28
71	Na,Na-Dimethylhistamine	$C_7H_{13}N_3^{+\bullet}$	139.1109	139.1121	8.41
72	Oxamniquine	$C_{14}H_{21}N_3O_3(+H^+)$	280.1656	280.1656	0.00
73	PA(30:1)	$C_{33}H_{63}O_8P(+Na^+)$	641.4153	641.4091	9.67
74	PC(30:1)/PE(33:1)	$C_{38}H_{74}NO_8P(+Na^+)$	726.5044	726.5055	1.49
75	PC(32:1)	$C_{40}H_{78}NO_8P(+H^+)$	732.5538	732.5543	0.63
76	PC(32:3)/ PE(35:3)	$C_{40}H_{74}NO_8P(+H^+)$	728.5211	728.5207	0.56
77	PC(34:1)/ PE(37:1)	$C_{42}H_{82}NO_8P(+H^+)$	760.5851	760.5861	1.33

		$C_{42}H_{82}NO_8P(+H-H_2O)$	742.5751	742.5753	0.31
78	PC(34:2)/ PE(37:2)	$C_{42}H_{80}NO_8P(+H-2H_2O)$	740.5595	740.5590	0.66
		$C_{42}H_{80}NO_8P(+H^+)$	758.5694	758.5713	2.52
		$C_{42}H_{80}NO_8P(+Na^+)$	780.5514	780.5514	0.01
79	PC(34:3)	$C_{42}H_{78}NO_8P(+H^+)$	756.5538	756.5546	1.10
80	PC(34:4)/ PE(37:4)	$C_{42}H_{76}NO_8P(+H^+)$	754.5381	754.5388	0.87
81	PC(34:5)/ PE(37:5)	$C_{42}H_{74}NO_8P(+H^+)$	752.5225	752.5232	0.97
82	PC(36:2)	$C_{44}H_{84}NO_8P(+H-H_2O)$	768.5908	768.5916	1.04
		$C_{44}H_{84}NO_8P(+H^+)$	786.6007	786.6044	4.64
		$C_{44}H_{84}NO_8P(+Na^+)$	808.5827	808.5835	0.99
		$C_{44}H_{84}NO_8P(+K^+)$	824.5566	824.5567	0.07
83	PC(36:3)	$C_{44}H_{82}NO_8P(+H-H_2O)$	766.5751	766.5761	1.32
84	PC(36:4)	$C_{44}H_{80}NO_8P(+H^+)$	782.5694	782.5717	2.94
85	PC(38:6)/ PE(37:2)	$C_{46}H_{80}NO_8P(+H^+)$	806.5694	806.5710	2.01
86	PC(40:5)	$C_{48}H_{86}NO_8P(+H-2H_2O)$	800.5964	800.6019	6.92
87	PC(O-30:0)	$C_{38}H_{78}NO_7P(+Na^+)$	714.5408	714.5423	2.10
88	PC(P-32:0)/PC(O-32:1)	$C_{40}H_{80}NO_7P(+H^+)$	718.5745	718.5766	2.91
		$C_{40}H_{80}NO_7P(+K^+)$	756.5304	756.5305	0.15
89	PE(38:4)	$C_{44}H_{79}O_{10}P(+H^+)$	799.5484	799.5487	0.40
90	PE(40:8)	$C_{45}H_{74}NO_8P(+H-H_2O)$	770.5125	770.5115	1.34
91	PE(44:8)	$C_{47}H_{78}NO_8P(+H-H_2O)$	798.5438	798.5439	0.09

92	PE(44:9)	$C_{47}H_{76}NO_8P(+H-H_2O)$	796.5282	796.5283	0.13
93	PG(34:1)	$C_{40}H_{77}O_{10}P(+Na^+)$	771.5147	771.5144	0.38
94	Phosphorylcholine	$C_5H_{15}NO_4P(+Na^+)$	206.0558	206.0555	1.36
		$C_5H_{15}NO_4P(+K^+)$	222.0298	222.0296	0.90
95	Phthalide	$C_8H_6O_2^{+\bullet}$	134.0368	134.0355	10.00
		$C_8H_6O_2(+H^+)$	135.0441	135.0441	0.30
96	Piperidine	$C_5H_{11}N(+H^+)$	86.0964	86.0966	2.79
97	Proline	$C_5H_9NO_2(+H^+)$	116.0706	116.0709	2.15
		$C_5H_9NO_2(+Na^+)$	138.0525	138.0526	0.87
		$C_5H_9NO_2(K^+)$	154.0265	154.0267	1.56
98	Pyridine	$C_5H_5N(+H^+)$	80.0495	80.0496	1.75
99	Pyridostigmine	$C_9H_{13}N_2O_2^{+\bullet}$	181.0977	181.0994	9.33
100	Pyruvatoxime	$C_3H_5NO_3(+H^+)$	104.0342	104.0343	1.35
101	SM(d39:2)	$C_{44}H_{87}N_2O_6P(+K^+)$	809.5933	809.5896	4.56
102	Spermidine	$C_7H_{19}N_3(+H^+)$	146.1652	146.1656	3.01
103	Taurine	$C_2H_7NO_3S(+H^+)$	148.0039	148.0040	0.88
104	Tetrahydropteridine	$C_6H_8N_4^{+\bullet}$	136.0749	136.0756	5.36
105	Thioguanine	$C_5H_5N_5S(+H-H_2O)$	150.0239	150.0249	6.40
106	Threonine	$C_4H_9NO_3(+Na^+)$	142.0475	142.0475	0.07

107	Treosulfan	$C_6H_{14}O_8S_2$(+H-H_2O)	261.0103	261.0118	5.63
108	Trimethylaminoacetone	$C_6H_{14}NO^{+•}$	116.1075	116.1072	2.41
109	Valine	$C_5H_{11}NO_2$(+H$^+$)	118.0863	118.0865	2.03
		$C_5H_{11}NO_2$ (+Na$^+$)	140.0682	140.0682	0.07
110	Valine betaine	$C_8H_{18}NO_2^{+•}$	160.1332	160.1334	1.25
111	α-[3-(nitrosoamino)propyl]-3-pyridinemethanol	$C_9H_{13}N_3O_2^{+•}$	195.1008	195.1017	4.72

Development of a 3D-Printed Ionization Source for Single-Cell Analysis

This chapter presents a method for manufacturing an ionization source that is specially adapted for mass spectrometry-based single-cell analysis using 3D printing technology. This all-in-one 3D-printed ESI source integrates the sample introduction, metabolite extraction and ionization into one device, simplifying the process of single-cell analysis and improving the reproducibility of the measurement. We successfully used it for high-throughput analysis of three types of cancer cells (around 17 cells/min), and used the t-SNE algorithm to distinguish different cell types based on selected features. When compared to other ionization sources, 3D-printed ionization sources have the advantages of low cost, fast fabrication time, and mass production.

5.1. Introduction

The study of metabolic heterogeneity in cells is essential to understand the physiology and pathology of diseases.[172-174] In this context, it is of great interest to perform metabolomics at the single-cell level. However, analyzing metabolites in single cells is difficult due to the fast metabolic dynamics, the large diversity of the molecular structures, and the inability to label or amplify metabolites.[1]

In recent years, mass spectrometry has been widely used for single-cell metabolomics analysis because it is very sensitive, highly specific, and able to analyze multiple molecules

simultaneously.[20,26,29,32,34-35,37,44,48,57,63,76,175] The electrospray ionization (ESI) source is one of the most popular used ionization sources in single-cell mass spectrometry.[20,37,44,48,57,175] It is an atmospheric pressure ionization source that does not require a vacuum operating environment and can sample single cells in situ for analysis. For example, Masujima and colleagues pioneered this field by developing a "live single-cell MS" (live MS) method and using it to investigate subcellular metabolites in RBL-2H3 (rat leukemia cell line),[24] plant cells[39,41] and CTCs.[38] Yang and co-workers developed a single-probe-based nanoESI source to directly analyze metabolites in single HeLa cells.[42] Vertes and co-workers proposed *in-situ* analysis of individual cells by LAESI-MS at atmospheric pressure, and successfully analyzed metabolites plant cells.[37] Because hundreds or thousands of measurements are required in biology to produce statistically significant data, this places challenging demands on the throughput of single-cell mass spectrometry. Therefore, microfluidic methods have been coupled with nanoESI for single-cell analysis to enable high-throughput analysis and obtain biologically meaningful data.[56-60] For example, capillary microfluidics platform-based flow cytometry ESI-MS (CyESI-MS) technique[57-58] developed by Zhang group and organic mass cytometry combining nanoESI with microfluidic chips[59] proposed by Liu group have been used to achieve high-throughput single-cell analysis. Although these methods have achieved high-throughput single-cell analysis, the assembly of the cell introduction system and its assembly with the ESI source may be biased, which will affect the reproducibility and accuracy of results.

Here, we report on a versatile all-in-one three-dimensional (3D)-printed ESI source for single-cell analysis that simplifies the process and improves the reproducibility of single-cell analysis by integrating sample introduction, metabolite extraction, and

ionization of analytes into one unit (Figure 5.1). In this study, 3D printing provided sharable CAD data, good reproducibility, high accuracy, short manufacturing time and low printing cost for this 3D-printed ionization source. The capability of the 3D-printed ionization source was validated by successful analyses of three types of cancer cells. To the best of our knowledge, this is the first time 3D-printing technology has been used to design an ionization source for single-cell analysis.

5.2. Experimental Section

5.2.1 Chemicals, Materials and cells

Methanol (99.9%) and ammonium formate (>99.0%) were purchased from Sigma-Aldrich Chemie GmbH (Buchs, Switzerland). 0:8 PC and 0:12 PC were purchased from from Avanti Polar Lipids (Birmingham, UK). Phosphate Buffer Saline (PBS) were purchased from Thermo Fisher Scientific (Buchs, Switzerland). Fused silica capillary tubes were purchased from Polymicro Technologies (BGB Analytik AG, Switzerland). HeLa, Panc 10.05 and AsPC-1 cells were purchased from ATCC.

5.2.2 Cell culture

HeLa was maintained in DMEM medium supplied with 10% (v/v) fetal bovine serum and 1% Penicillin-Streptomycin (P/S). Panc 10.05 and AsPC-1 cells were maintained in RPMI-1640 medium supplemented with 10% (v/v) fetal bovine serum and 1% Penicillin-Streptomycin (P/S). The cells were cultured at 37°C in the humidified incubator (Thermo Fisher Scientific) with 5% CO_2.

5.2.3 Preparation of Cell Suspensions

Prior to the experiment, cells were trypsinized and centrifuged at 1000 rpm for 4 minutes to remove the medium, and then they were resuspended in 1xPBS. The cells were resuspended in 140 mM NH_4COOH solution after undergoing a second centrifugation (1000 rpm, 4 minutes) to remove PBS.

5.2.4 Design and fabrication of the 3D-printed ionization source

Autodesk Inventor Professional 2021 (California, USA) was used to design the 3D-printed ionization source, which was then printed using "VisiJet M2R-CL" material (3D Systems, California, USA) by a professional 3D printer (ProJet MJP 2500, 3D Systems, California, USA). The 3D-printed ionization source was cleaned with steam and isopropanol after printing, and dried in an oven for 24 hours before usage. The details of the design of the 3D-printed ionization can be found in the technical drawing shown in Figure 5.1a. In brief, the all-in-one 3D-printed ESI source consists of three channels, as shown in Figure 5.1a. The external channel (1 mm I.D.) was used for gas introduction. MeOH was introduced from the intermediate channel (300 μm I.D.) as an extraction solution. A fused silica capillary (193 μm O.D., 75 μm I.D.) was inserted through the internal channel (200 μm I.D.) of the 3D-printed ionization source to deliver cell suspensions. Figure 5.1b shows a photograph of the 3D-printed ionization source.
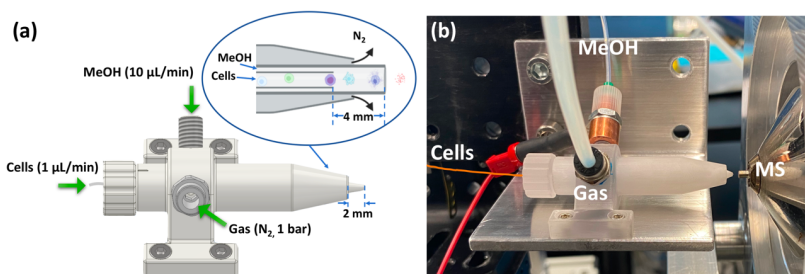
Figure 5.1. Schematic diagram (Figure 5.1a) and photograph (Figure 5.1b) of the 3D-printed ionization source. Cells are introduced, lysed by a coaxial flow of methanol, and N_2 gas serves as a sheath gas to help produce the spray. (When the MeOH flow rate was 10 μL/min and the distance between the inner capillary and the intermediate channel was 4 mm, the highest signal intensity of PC (34:1) was detected, and the highest number of cells per minute was detected, so these conditions were chosen for further experiments.)

5.2.5 Procedure for single-cell analysis

Before cell introduction, the intermediate channel was carefully washed with MeOH, and the inner capillary was thoroughly rinsed with a 140 mM NH_4COOH aqueous solution until the background total ion chromatogram (TIC) remained stable. The freshly prepared cell suspension was injected into the inner capillary at a flow rate of 1 μL/min, while MeOH was introduced into the intermediate channel at a flow rate of 10 μL/min. A DC voltage of 5.0 kV was applied to the MeOH through an electrode, creating a stable electrospray at the tip of the intermediate channel. As shown in Figure 5.1a, the outlet end of the intermediate channel was 4 mm longer than the outlet end of the inner capillary. When the cell suspension exits the inner capillary and comes into contact with MeOH in the intermediate channel, the cells are lysed and metabolites in the cells are extracted into MeOH and nebulized into the mass spectrometer with the assistance of a flow of nitrogen sheath gas in the external channel. All channels were

flushed with MeOH for 10 minutes at a flow rate of 7 L/min following each measurement.

5.2.6 Mass Spectrometry

Mass spectra were acquired in positive ion mode, with an LTQ Orbitrap mass spectrometer (Thermo Fischer Scientific, San Jose, U.S.A.), in full scan mode at a resolution of 30,000 FWHM (at m/z 400) with a mass tolerance specified to be < 10 ppm. The mass-to-charge range was set to 100–1000, the capillary voltage was 50 V, the tube lens voltage was 120 V, the capillary temperature was 320°C, and the AGC target value was 10^6. Mass spectra were acquired using 1 microscan and a maximum injection time of 10 ms.

5.2.7 Data analysis

Raw files were converted to mzML format by using the module MSConverter in the ProteoWizard (v3.0) software. After this, all analyses and graphs were made with the software R. The spectra were extracted and preprocessed with the MALDIQUANT package for R. This indicated normalization to the TIC, spectrum alignment, signal-to-noise filtering with a value of 3, removal of features present in less than 20% of samples and those with more than 20% of zero values. The markers PC (34:1) (m/z 760.5894) and PC (32:1) (m/z 732.5554) were chosen to detect single cells and extract all associated ion signals. Then the t-SNE algorithm was constructed with 388 features (perplexity value of 50 and 5000 iterations).

5.3. Results and Discussion

Before detecting cells, two phosphatidylcholine standards (0:8 PC and 0:12 PC) dissolved in MeOH were used to evaluate the viability of the 3D-printed ionization source. As shown in Figure 5.2, the ions of these two phosphatidylcholines appeared as $[M + H]^+$ and $[M + Na]^+$, which are regularly observed in ESI.
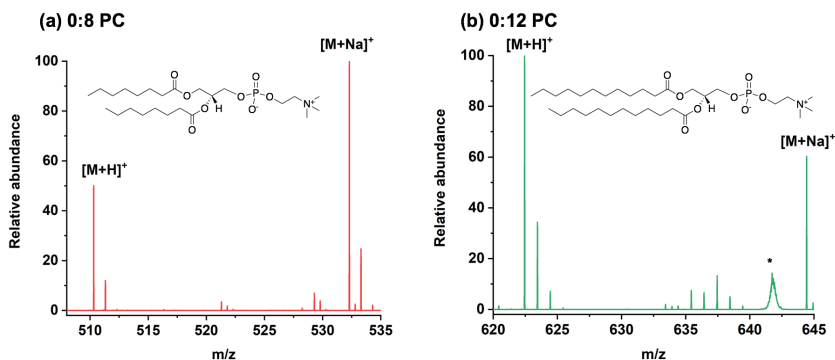
Figure 5.2. Mass spectra of two lipids measured by the 3D-printed ion source, (a) 0:8 PC and (b) 0:12 PC (ESI voltage: 5 kV; the asterisk (*) indicates electronic noise in the spectra.)

We then applied the 3D-printed ionization source for single-cell analysis of AsPC-1 cells. An AsPC-1 cell suspension (2×10^4 cells/mL) was introduced into the 3D-printed ionization source. The lipid PC (32:1) (m/z 732.55), the main component of the cell membrane, was selected as a marker for cell lysate entering the mass spectrometer, and its signal pulses in the extracted ion chromatogram (EIC) matched those in the total ion chromatogram (TIC) (Figures 5.3a and b), and separate mass spectra of individual cells could be extracted from the signal pulses in the EIC (Figure 5.3c). As shown in Figures 5.3a and b, 17 cells on average were detected per minute, which is slightly lower than the theoretical number of 20 cells/min,

calculated from the cell diversity of the suspension and the flow rate, probably due to the cell introduction process that led to some cell loss and occasional inclusion of more than 1 cell.
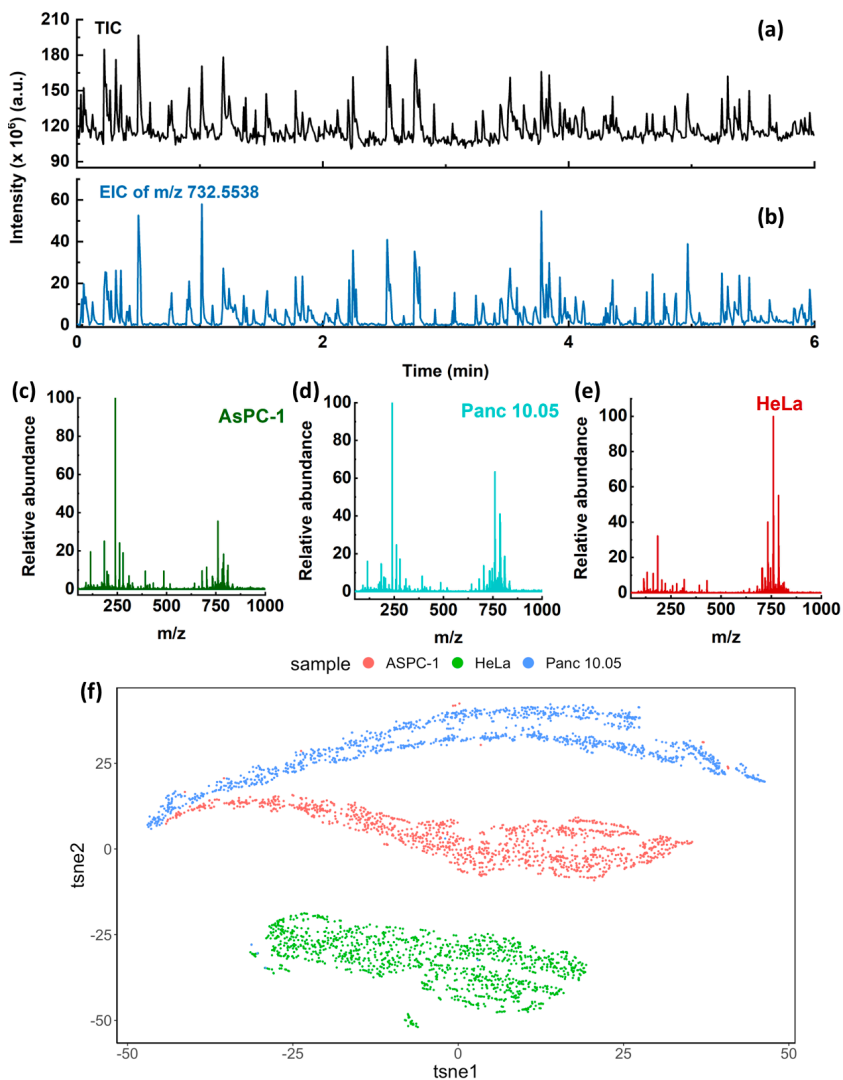
Figure 5.3. Three types of cancer cells measured by the 3D-printed ionization source in positive mode. (a) TIC and (b) EIC of m/z 732.5554 of an AsPC-1 cell suspension. (c) Typical AsPC-1 single-cell mass spectrum. (d) Typical Panc 10.05 single-cell mass spectrum. (e) Typical HeLa single-cell mass spectrum. (f) t-SNE analysis of AsPC-1, Panc 10.05 and HeLa cells, each point represents a cell, and clustering for each cell type can be observed. (AsPC-1 and Panc 10.05 are human pancreatic cancer cell lines, and HeLa is a human cervical cancer cell line.)

After validating the capability of 3D-printed ionization source for single-cell analysis, we used it to measure two more cancer cell types, Panc 10.05 cells and HeLa cells, to study cellular heterogeneity. The mass spectra of Panc 10.05 and HeLa cells are shown in Figures 5.3d and e. After data preprocessing, the t-SNA selected 388 features from these three cancer cell lines. We then used t-distributed stochastic neighbor embedding (t-SNE), an unsupervised nonlinear technique useful for data visualization. Based on the chemical profiles obtained after data treatment, three types of cancer cells are visualized by the t-SNE algorithm. (Figure 5.3f).

5.4. Conclusions

Overall, this work is the first to use a 3D-printed ionization source for single-cell analysis. This all-in-one 3D-printed ESI source was successfully applied to analyze three different types of cancer cells (AsPC-1, Panc 10.05 and HeLa) with a throughput of approximately 17 cells per minute. Based on the measured compounds, our method allows distinguishing different cancer cells. The development of 3D-printed ionization sources provides more possibilities for single-cell analysis.

Conclusions & Outlook

Because even populations of clonal cells are heterogeneous, it is of great significance to develop analysis methods with single-cell sensitivity. Mass spectrometry is increasingly used for single-cell analysis, due to its high sensitivity, good selectivity, and ability to detect multiple compounds simultaneously. Single-cell mass spectrometry cannot be advanced further without the development of ionization sources, because any ionization source has its own advantages and limitations, and different methods can complement each other.

In this dissertation, home-built ambient ionization sources, including a DBDI source, a hybrid ESI-DBDI source and a 3D-printed ionization source, were developed to investigate single-cell metabolomics.

Firstly, a high-throughput (38 cells/min), label-free and sensitive DBDI-MS platform was developed for the analysis of single-cell metabolites. The DBDI-MS platform is able to discriminate different cell types (HEK-293T, PANC-1, CFPAC-1, H6c7, HeLa, and iBAs) successfully, based on the presence of different cellular metabolites. A key innovation of this work is that mass spectrometry was used to provide novel insights into abnormal lipid metabolism in established PDAC. We propose that ACLY could be a potential target for treating established PDAC. A variety of biological methods were used to investigate the expression levels of ACLY and the activation of related biological pathways in the TCGA dataset and PDAC cells. The DBDI-MS platform observed the redistribution of lipids in PDAC cells after treating them with different doses of a specific ACLY inhibitor. Further biological experiments revealed that both ACLY inhibitors

and genetic approaches targeting ACLY could suppress PDAC cell viability. These findings demonstrate the high sensitivity of our DBDI-MS platform and confirm that ACLY does indeed govern lipid metabolism in PDAC cells, implying that ACLY could be a novel therapeutic target in PDAC. As a result, our DBDI-MS platform has the potential to become useful for mass cytometry, thereby contributing to biological and clinical research.

Next, we reported a hybrid ionization source that combines ESI and DBDI to improve analyte coverage (mainly targeting non-polar compounds). This hybrid ESI + DBDI source apparently relies on several ionization processes, including Penning ionization, charge transfer, and proton transfer. In this work, the metabolites in human (PANC-1) and plant cells (onion) were investigated. After optimization, 40 compounds in PANC-1 cells and 50 compounds in onion cells were detected in ESI only mode (3.5 kV). In ESI (3.5 kV)-DBDI (2.6 kV) hybrid mode, additional 73 compounds in PANC-1 cells and an additional 49 compounds in onion cells were measured. With its improved coverage, ionization efficiency, and limit of detection of metabolites with various polarities, this hybrid ionization source may help to accelerate the development of single-cell metabolomics.

Finally, we proposed a 3D-printed ionization source for single-cell analysis. Three types of cancer cells (AsPC-1, Panc 10.05, and HeLa) were successfully measured using the ionization source at a throughput of about 17 cells per minute. Our technique enables cell type discrimination of various cancer cells based on the detected metabolites. This ionization source is cheaper, more reproducible, and more easily manufactured as compared to other ionization sources. The development of 3D-printed ionization sources also opens up new avenues for single-cell analysis.

Despite the progress made in mass spectrometry-based single-cell analysis, there is still some space for improvement:

(1) Sampling methods.

Most current single-cell mass spectrometry techniques are destructive, which makes it difficult to monitor and measure intracellular metabolites in real time during cell proliferation or drug treatment. Therefore, it is necessary to develop *in-situ* non-destructive single-cell sampling methods that work efficiently and high throughput, without interfering with the normal metabolic processes of cells. For example, Nemes and co-workers employed *in-situ* microprobe sampling for developing *Xenopus laevis* embryos. After sampling and measurement, they tested the embryos' viability and found that they can still develop freely into visually normally behaving tadpoles.[51] However, this sampling method is still on the slow side in terms of throughput.

The efficiency of single-cell analysis can be increased by developing single-cell automatic sampling devices, which can save time for sampling and effort of the experimenter. The sample throughput of single-cell mass spectrometry can be improved by combining cell sorting techniques such as flow cytometry and inkjet cell printing, or microfluidic chips with mass spectrometers. For example, Zhang and co-workers proposed a capillary microfluidics platform-based flow cytometry ESI-MS (CyESI-MS) technique to achieve high-throughput single-cell analysis (38 cells/min), cell type discrimination, and biomarker screening.[57-58] Liu and co-workers combined nanoESI with microfluidic chips to identify 100 metabolites and 6 protein biomarkers in single cancer cells with a high throughput of 40 cells/min, and they successfully distinguished different cell types based on the information of simultaneously detected proteins and metabolites.[59]

(2) Sensitivity and dynamic range of mass spectrometry.

Since the intracellular chemical composition is very complex, the size of a cell is very small, and some intracellular metabolites are present only at the trace level, single-cell metabolomics is challenging. Therefore, it is important to improve the sensitivity and dynamic range of mass spectrometry to realize the detection of low-abundance metabolites in single cells. Improvements in instrument functionality and sample preparation steps will help to improve the overall sensitivity and dynamic range required for routine single-cell metabolomics analysis.

(3) Ionization methods.

Each single-cell ionization method has its own advantages. For instance, although SIMS has a high spatial resolution and is suitable for subcellular analysis, the ionization process typically results in many fragments. Although the spatial resolution of MALDI is far less than that of SIMS, MALDI is a soft ionization method that can detect a wide range of compounds with relatively high sensitivity. However, MALDI needs a relatively complex sample preparation. NanoESI can be used for sampling and ionization of metabolites in living cells, and it is suitable for the ionization of polar metabolites, but it is less suitable for ionizing nonpolar metabolites due to its ionization mechanism. Since different ionization methods can complement each other, developing new ionization sources and hybrid sources should be beneficial for the study of single-cell metabolomics. For example, in this dissertation, we developed a DBDI source and a hybrid ionization source that combines ESI source and DBDI source to improve metabolites coverage in single cells. In addition, we fabricated and used a high-throughput ESI-based 3D-printed ionization source for single-cell metabolomics. This 3D-printed ionization source integrates the cell introduction system, metabolite extraction and ionization source into one unit, simplifying the process of single-cell analysis.

(4) Multi-omics research.

The range of biomolecules that can be detected in single cells is continuously expanding due to the improvement of the performance of single-cell analysis methods. The study of single-cell multi-omics has become increasingly popular. For example, Nemes and co-workers enabled in vivo single-cell proteomics and metabolomics in South African clawed frog embryos *via* CE-ESI-MS.[160] Future omics research will continue to go deeper, not only focusing on measurement issues but also penetrating into important cell biology-related issues. Mass spectrometry can be combined with multiple techniques to obtain more information, thus realizing the study of single-cell multi-omics.

(5) Data analysis for single-cell metabolomics.

The lack of well-established open-access data analysis platforms that are particularly suitable for single-cell metabolomics is a problem that prevents the widespread development of single-cell metabolomics. Each laboratory has to develop its own tools, which hinders collaboration and attempts to reproduce the results. This is made even more difficult by the variety of mass spectrometric methods used in single-cell metabolomics, and consequently, the file formats and kinds of data collected. Therefore, it is still work in progress for MS-based single-cell metabolomic research to design standardized and validated single-cell data analysis pipelines for metabolomics with the correct identification of noise sources.

In conclusion, single-cell metabolomics should be combined with information from single-cell proteomics, genomics, and transcriptomics to study metabolic pathways and principles based on the detection of metabolites, in order to be able to address and solve profound problems related to life sciences, human health and disease. We hope to have delivered some encouraging ideas for the development of single-cell mass spectrometry in this thesis.

References

(1) Zenobi, R. Single-cell metabolomics: analytical and biological perspectives. *Science* **2013**, 342, 1243259.

(2) Abdallah, B. Y.; Horne, S. D.; Stevens, J. B., et al., Single cell heterogeneity. *Cell Cycle* **2013**, 12, 3640-3649.

(3) Jindal, A.; Gupta, P.; Jayadeva, et al., Discovery of rare cells from voluminous single cell expression data. *Nat. Commun.* **2018**, 9, 4719.

(4) Nassar, S. F.; Raddassi, K.; Wu, T. Single-Cell Multiomics Analysis for Drug Discovery. *Metabolites* **2021**, 11.

(5) Wang, D.; Bodovitz, S. Single cell analysis: the new frontier in 'omics'. *Trends Biotechnol.* **2010**, 28, 281-290.

(6) Bock, C.; Farlik, M.; Sheffield, N. C. Multi-Omics of Single Cells: Strategies and Applications. *Trends Biotechnol.* **2016**, 34, 605-608.

(7) Amantonico, A.; Urban, P. L.; Zenobi, R. Analytical techniques for single-cell metabolomics: state of the art and trends. *Anal. Bioanal. Chem.* **2010**, 398, 2493-2504.

(8) German, J. B.; Hammock, B. D.; Watkins, S. M. Metabolomics: building on a century of biochemistry to guide human health. *Metabolomics* **2005**, 1, 3-9.

(9) Heinemann, M.; Zenobi, R. Single cell metabolomics. *Curr. Opin. Biotechnol.* **2011**, 22, 26-31.

(10) Schmid, A.; Kortmann, H.; Dittrich, P. S., et al., Chemical and biological single cell analysis. *Curr. Opin. Biotechnol.* **2010**, 21, 12-20.

(11) Lin, Z. C.; Xie, C.; Osakada, Y., et al., Iridium oxide nanotube electrodes for sensitive and prolonged intracellular measurement of action potentials. *Nat. Commun.* **2014**, 5, 3206.

(12) Liu, Y.; Li, M.; Zhang, F., et al., Development of Au Disk Nanoelectrode Down to 3 nm in Radius for Detection of Dopamine Release from a Single Cell. *Anal. Chem.* **2015**, 87, 5531-5538.

(13) Li, Y.-T.; Zhang, S.-H.; Wang, L., et al., Nanoelectrode for Amperometric Monitoring of Individual Vesicular Exocytosis Inside Single Synapses. *Angew. Chem., Int. Ed.* **2014**, 53, 12456-12460.

(14) Sandmann, M.; Lippold, M.; Saalfrank, F., et al., Multidimensional single-cell analysis based on fluorescence microscopy and automated image analysis. *Anal. Bioanal. Chem.* **2017**, 409, 4009-4019.

(15) Murschhauser, A.; Röttgermann, P. J. F.; Woschée, D., et al., A high-throughput microscopy method for single-cell analysis of event-time correlations in nanoparticle-induced cell death. *Commun. Biol.* **2019**, 2, 35.

(16) Muzzey, D.; van Oudenaarden, A. Quantitative Time-Lapse Fluorescence Microscopy in Single Cells. *Annu. Rev. Cell Dev. Biol.* **2009**, 25, 301-327.

(17) Harrison, J. P.; Berry, D. Vibrational Spectroscopy for Imaging Single Microbial Cells in Complex Biological Samples. *Frontiers in Microbiology* **2017**, 8.

(18) Spadea, A.; Denbigh, J.; Lawrence, M. J., et al., Analysis of Fixed and Live Single Cells Using Optical Photothermal Infrared with Concomitant Raman Spectroscopy. *Anal. Chem.* **2021**, 93, 3938-3950.

(19) Li, M.; Xu, J.; Romero-Gonzalez, M., et al., Single cell Raman spectroscopy for cell sorting and imaging. *Curr. Opin. Biotechnol.* **2012**, 23, 56-63.

(20) Lombard-Banek, C.; Moody, S. A.; Manzini, M. C., et al., Microsampling Capillary Electrophoresis Mass Spectrometry Enables Single-Cell Proteomics in Complex Tissues: Developing Cell Clones in Live Xenopus laevis and Zebrafish Embryos. *Anal. Chem.* **2019**, 91, 4797-4805.

(21) Kawai, T.; Ota, N.; Okada, K., et al., Ultrasensitive Single Cell Metabolomics by Capillary Electrophoresis–Mass Spectrometry with a Thin-Walled Tapered Emitter and Large-Volume Dual Sample Preconcentration. *Anal. Chem.* **2019**, 91, 10564-10572.

(22) Zhuang, M.; Hou, Z.; Chen, P., et al., Introducing charge tag via click reaction in living cells for single cell mass spectrometry. *Chem. Sci.* **2020**, 11, 7308-7312.

(23) Stolee, J. A.; Shrestha, B.; Mengistu, G., et al., Observation of subcellular metabolite gradients in single cells by laser ablation electrospray ionization mass spectrometry. *Angew. Chem., Int. Ed.* **2012**, 51, 10386-10389.

(24) Fujii, T.; Matsuda, S.; Tejedor, M. L., et al., Direct metabolomics for plant cells by live single-cell mass spectrometry. *Nat. Protoc.* **2015**, 10, 1445-1456.

(25) Amantonico, A.; Oh, J. Y.; Sobek, J., et al., Mass spectrometric method for analyzing metabolites in yeast with single cell sensitivity. *Angew. Chem., Int. Ed.* **2008**, 47, 5382-5385.

(26) Do, T. D.; Comi, T. J.; Dunham, S. J., et al., Single Cell Profiling Using Ionic Liquid Matrix-Enhanced Secondary Ion Mass Spectrometry for Neuronal Cell Type Differentiation. *Anal. Chem.* **2017**, 89, 3078-3086.

(27) Chen, X.; Sun, M.; Yang, Z. Single cell mass spectrometry analysis of drug-resistant cancer cells: Metabolomics studies of synergetic effect of combinational treatment. *Anal. Chim. Acta* **2022**, 1201, 339621.

(28) Song, L.; Chingin, K.; Wang, M., et al., Polarity-Specific Profiling of Metabolites in Single Cells by Probe Electrophoresis Mass Spectrometry. *Anal. Chem.* **2022**, 94, 4175-4182.

(29) Amantonico, A.; Urban, P. L.; Fagerer, S. R., et al., Single-Cell MALDI-MS as an Analytical Tool for Studying Intrapopulation Metabolic Heterogeneity of Unicellular Organisms. *Anal. Chem.* **2010**, 82, 7394-7400.

(30) Xie, W.; Gao, D.; Jin, F., et al., Study of Phospholipids in Single Cells Using an Integrated Microfluidic Device Combined with Matrix-Assisted Laser Desorption/Ionization Mass Spectrometry. *Anal. Chem.* **2015**, 87, 7052-7059.

(31) Fu, Q.; Tang, J.; Cui, M., et al., Application of porous metal enrichment probe sampling to single cell analysis using matrix-assisted laser desorption ionization time of flight mass spectrometry (MALDI-TOF-MS). *J. Mass Spectrom.* **2016**, 51, 62-68.

(32) Tian, H.; Sparvero, L. J.; Blenkinsopp, P., et al., Secondary-Ion Mass Spectrometry Images Cardiolipins and Phosphatidylethanolamines at the Subcellular Level. *Angew. Chem., Int. Ed.* **2019**, 58, 3156-3161.

(33) Yuan, Z.; Zhou, Q.; Cai, L., et al., SEAM is a spatial single nuclear metabolomics method for dissecting tissue microenvironment. *Nat. Methods* **2021**, 18, 1223-1232.

(34) Liu, Q.; Ge, W.; Wang, T., et al., High-Throughput Single-Cell Mass Spectrometry Reveals Abnormal Lipid Metabolism in Pancreatic Ductal Adenocarcinoma. *Angew. Chem., Int. Ed.* **2021**, 60, 24534-24542.

(35) Liu, Q.; Lan, J.; Wu, R., et al., Hybrid Ionization Source Combining Nanoelectrospray and Dielectric Barrier Discharge Ionization for the

Simultaneous Detection of Polar and Nonpolar Compounds in Single Cells. *Anal. Chem.* **2022**, 94, 2873-2881.

(36) Nišavić, M.; Janjić, G. V.; Hozić, A., et al., Positive and negative nano-electrospray mass spectrometry of ruthenated serum albumin supported by docking studies: an integrated approach towards defining metallodrug binding sites on proteins†. *Metallomics* **2018**, 10, 587-594.

(37) Shrestha, B.; Vertes, A. In Situ Metabolic Profiling of Single Cells by Laser Ablation Electrospray Ionization Mass Spectrometry. *Anal. Chem.* **2009**, 81, 8265-8271.

(38) Abouleila, Y.; Onidani, K.; Ali, A., et al., Live single cell mass spectrometry reveals cancer-specific metabolic profiles of circulating tumor cells. *Cancer Sci.* **2019**, 110, 697-706.

(39) Lorenzo Tejedor, M.; Mizuno, H.; Tsuyama, N., et al., In Situ Molecular Analysis of Plant Tissues by Live Single-Cell Mass Spectrometry. *Anal. Chem.* **2012**, 84, 5221-5228.

(40) Mizuno, H.; Tsuyama, N.; Harada, T., et al., Live single-cell video-mass spectrometry for cellular and subcellular molecular detection and cell classification. *J. Mass Spectrom.* **2008**, 43, 1692-1700.

(41) Fujii, T.; Matsuda, S.; Tejedor, M. L., et al., Direct metabolomics for plant cells by live single-cell mass spectrometry. *Nat. Protoc.* **2015**, 10, 1445-1456.

(42) Pan, N.; Rao, W.; Kothapalli, N. R., et al., The Single-Probe: A Miniaturized Multifunctional Device for Single Cell Mass Spectrometry Analysis. *Anal. Chem.* **2014**, 86, 9376-9380.

(43) Zhu, Y.; Liu, R.; Yang, Z. Redesigning the T-probe for mass spectrometry analysis of online lysis of non-adherent single cells. *Anal. Chim. Acta* **2019**, 1084, 53-59.

(44) Gong, X.; Zhao, Y.; Cai, S., et al., Single cell analysis with probe ESI-mass spectrometry: detection of metabolites at cellular and subcellular levels. *Anal. Chem.* **2014**, 86, 3809-3816.

(45) Nemes, P.; Rubakhin, S. S.; Aerts, J. T., et al., Qualitative and quantitative metabolomic investigation of single neurons by capillary electrophoresis electrospray ionization mass spectrometry. *Nat. Protoc.* **2013**, 8, 783-799.

(46) Lapainis, T.; Rubakhin, S. S.; Sweedler, J. V. Capillary Electrophoresis with Electrospray Ionization Mass Spectrometric Detection for Single-Cell Metabolomics. *Anal. Chem.* **2009**, 81, 5858-5864.

(47) Onjiko Rosemary, M.; Moody Sally, A.; Nemes, P. Single-cell mass spectrometry reveals small molecules that affect cell fates in the 16-cell embryo. *Proc. Natl. Acad. Sci. U. S. A.* **2015**, 112, 6545-6550.

(48) Lombard-Banek, C.; Moody, S. A.; Nemes, P. Single-Cell Mass Spectrometry for Discovery Proteomics: Quantifying Translational Cell Heterogeneity in the 16-Cell Frog (Xenopus) Embryo. *Angew. Chem., Int. Ed.* **2016**, 55, 2454-2458.

(49) Onjiko, R. M.; Portero, E. P.; Moody, S. A., et al., In Situ Microprobe Single-Cell Capillary Electrophoresis Mass Spectrometry: Metabolic Reorganization in Single Differentiating Cells in the Live Vertebrate (Xenopus laevis) Embryo. *Anal. Chem.* **2017**, 89, 7069-7076.

(50) Portero, E. P.; Nemes, P. Dual cationic–anionic profiling of metabolites in a single identified cell in a live Xenopus laevis embryo by microprobe CE-ESI-MS. *Analyst* **2019**, 144, 892-900.

(51) Lombard-Banek, C.; Li, J.; Portero, E. P., et al., In Vivo Subcellular Mass Spectrometry Enables Proteo-Metabolomic Single-Cell Systems Biology in a Chordate Embryo Developing to a Normally Behaving Tadpole (X. laevis)*. *Angew. Chem., Int. Ed.* **2021**, 60, 12852-12858.

(52) Stolee, J. A.; Vertes, A. Toward Single-Cell Analysis by Plume Collimation in Laser Ablation Electrospray Ionization Mass Spectrometry. *Anal. Chem.* **2013**, 85, 3592-3598.

(53) Stopka, S. A.; Khattar, R.; Agtuca, B. J., et al., Metabolic Noise and Distinct Subpopulations Observed by Single Cell LAESI Mass Spectrometry of Plant Cells in situ. *Front. Plant Sci.* **2018**, 9, 1646.

(54) Joensson, H. N.; Andersson Svahn, H. Droplet Microfluidics—A Tool for Single-Cell Analysis. *Angew. Chem., Int. Ed.* **2012**, 51, 12176-12192.

(55) Whitesides, G. M. The origins and the future of microfluidics. *Nature* **2006**, 442, 368-373.

(56) Zhang, L.; Xu, T.; Zhang, J., et al., Single Cell Metabolite Detection Using Inertial Microfluidics-Assisted Ion Mobility Mass Spectrometry. *Anal. Chem.* **2021**, 93, 10462-10468.

(57) Yao, H.; Zhao, H.; Zhao, X., et al., Label-free Mass Cytometry for Unveiling Cellular Metabolic Heterogeneity. *Anal. Chem.* **2019**, 91, 9777-9783.

(58) Yao, H.; Zhao, H.; Pan, X., et al., Discriminating Leukemia Cellular Heterogeneity and Screening Metabolite Biomarker Candidates using Label-Free Mass Cytometry. *Anal. Chem.* **2021**, 93, 10282-10291.

(59) Xu, S.; Liu, M.; Bai, Y., et al., Multi-Dimensional Organic Mass Cytometry: Simultaneous Analysis of Proteins and Metabolites on Single Cells. *Angew. Chem., Int. Ed.* **2020**, 60, 1806-1812.

(60) Huang, Q.; Mao, S.; Khan, M., et al., Dean flow assisted cell ordering system for lipid profiling in single-cells using mass spectrometry. *Chem. Commun.* **2018**, 54, 2595-2598.

(61) Comi, T. J.; Makurath, M. A.; Philip, M. C., et al., MALDI MS Guided Liquid Microjunction Extraction for Capillary Electrophoresis–Electrospray Ionization MS Analysis of Single Pancreatic Islet Cells. *Anal. Chem.* **2017**, 89, 7765-7772.

(62) Fagerer, S. R.; Schmid, T.; Ibáñez, A. J., et al., Analysis of single algal cells by combining mass spectrometry with Raman and fluorescence mapping. *Analyst* **2013**, 138, 6732-6736.

(63) Neumann, E. K.; Comi, T. J.; Rubakhin, S. S., et al., Lipid Heterogeneity between Astrocytes and Neurons Revealed by Single-Cell MALDI-MS Combined with Immunocytochemical Classification. *Angew. Chem., Int. Ed.* **2019**, 58, 5910-5914.

(64) Niehaus, M.; Soltwisch, J.; Belov, M. E., et al., Transmission-mode MALDI-2 mass spectrometry imaging of cells and tissues at subcellular resolution. *Nat. Meth.* **2019**, 16, 925-931.

(65) Neumann, E. K.; Ellis, J. F.; Triplett, A. E., et al., Lipid Analysis of 30 000 Individual Rodent Cerebellar Cells Using High-Resolution Mass Spectrometry. *Anal. Chem.* **2019**, 91, 7871-7878.

(66) Urban, P. L.; Jefimovs, K.; Amantonico, A., et al., High-density micro-arrays for mass spectrometry. *Lab Chip* **2010**, 10, 3206-3209.

(67) Urban, P. L.; Schmidt, A. M.; Fagerer, S. R., et al., Carbon-13 labelling strategy for studying the ATP metabolism in individual yeast cells by micro-arrays for mass spectrometry. *Mol. Biosyst.* **2011**, 7, 2837-2840.

(68) Ibáñez Alfredo, J.; Fagerer Stephan, R.; Schmidt Anna, M., et al., Mass spectrometry-based metabolomics of single yeast cells. *Proc. Natl. Acad. Sci. U. S. A.* **2013**, 110, 8790-8794.

(69) Urban, P. L.; Schmid, T.; Amantonico, A., et al., Multidimensional Analysis of Single Algal Cells by Integrating Microspectroscopy with Mass Spectrometry. *Anal. Chem.* **2011**, 83, 1843-1849.

(70) Soltwisch, J.; Kettling, H.; Vens-Cappell, S., et al., Mass spectrometry imaging with laser-induced postionization. *Science* **2015**, 348, 211-215.

(71) Beckercor, C. H.; Wufn, K. J. On the photoionization of large molecules. *J. Am. Soc. Mass Spectrom.* **1995**, 6, 883-888.

(72) Rohlfing, A.; Leisner, A.; Hillenkamp, F., et al., Investigation of the Desorption Process in UV Matrix-Assisted Laser Desorption/Ionization with a Liquid 3-Nitrobenzyl Alcohol Matrix by Photoacoustic Analysis, Fast-Flash Imaging, and UV-Laser Postionization. *J. Phys. Chem. C* **2010**, 114, 5367-5381.

(73) Kettling, H.; Vens-Cappell, S.; Soltwisch, J., et al., MALDI Mass Spectrometry Imaging of Bioactive Lipids in Mouse Brain with a Synapt G2-S Mass Spectrometer Operated at Elevated Pressure: Improving the Analytical Sensitivity and the Lateral Resolution to Ten Micrometers. *Anal. Chem.* **2014**, 86, 7798-7805.

(74) Soltwisch, J.; Souady, J.; Berkenkamp, S., et al., Effect of Gas Pressure and Gas Type on the Fragmentation of Peptide and Oligosaccharide Ions Generated in an Elevated Pressure UV/IR-MALDI Ion Source Coupled to an Orthogonal Time-of-Flight Mass Spectrometer. *Anal. Chem.* **2009**, 81, 2921-2934.

(75) Barré, F. P. Y.; Paine, M. R. L.; Flinders, B., et al., Enhanced Sensitivity Using MALDI Imaging Coupled with Laser Postionization (MALDI-2) for Pharmaceutical Research. *Anal. Chem.* **2019**, 91, 10840-10848.

(76) Soltwisch, J.; Heijs, B.; Koch, A., et al., MALDI-2 on a Trapped Ion Mobility Quadrupole Time-of-Flight Instrument for Rapid Mass Spectrometry Imaging and Ion Mobility Separation of Complex Lipid Profiles. *Anal. Chem.* **2020**, 92, 8697-8703.

(77) Agüi-Gonzalez, P.; Jähne, S.; Phan, N. T. N. SIMS imaging in neurobiology and cell biology. *J. Anal. At. Spectrom.* **2019**, 34, 1355-1368.

(78) Angerer, T. B.; Chakravarty, N.; Taylor, M. J., et al., Insights into the histology of planarian flatworm Phagocata gracilis based on location specific, intact lipid information provided by GCIB-ToF-SIMS imaging. *Biochim. Biophys. Acta, Mol. Cell Biol. Lipids* **2019**, 1864, 733-743.

(79) Kurczy Michael, E.; Piehowski Paul, D.; Van Bell Craig, T., et al., Mass spectrometry imaging of mating Tetrahymena show that changes in cell morphology regulate lipid domain formation. *Proc. Natl. Acad. Sci. U. S. A.* **2010**, 107, 2751-2756.

(80) Ostrowski Sara, G.; Van Bell Craig, T.; Winograd, N., et al., Mass Spectrometric Imaging of Highly Curved Membranes During Tetrahymena Mating. *Science* **2004**, 305, 71-73.

(81) Phan, N. T. N.; Fletcher, J. S.; Ewing, A. G. Lipid Structural Effects of Oral Administration of Methylphenidate in Drosophila Brain by Secondary Ion Mass Spectrometry Imaging. *Anal. Chem.* **2015**, 87, 4063-4071.

(82) Rabasco, S.; Nguyen, T. D. K.; Gu, C., et al., Localization and Absolute Quantification of Dopamine in Discrete Intravesicular Compartments Using NanoSIMS Imaging. *Int. J. Mol. Sci.* **2022**, 23.

(83) Passarelli, M. K.; Pirkl, A.; Moellers, R., et al., The 3D OrbiSIMS—label-free metabolic imaging with subcellular lateral resolution and high mass-resolving power. *Nat. Meth.* **2017**, 14, 1175-1183.

(84) Tian, H.; Maciążek, D.; Postawa, Z., et al., CO2 Cluster Ion Beam, an Alternative Projectile for Secondary Ion Mass Spectrometry. *J. Am. Soc. Mass Spectrom.* **2016**, 27, 1476-1482.

(85) Pareek, V.; Tian, H.; Winograd, N., et al., Metabolomics and mass spectrometry imaging reveal channeled de novo purine synthesis in cells. *Science* **2020**, 368, 283-290.

(86) Albert, A.; Engelhard, C. Characteristics of Low-Temperature Plasma Ionization for Ambient Mass Spectrometry Compared to Electrospray Ionization and Atmospheric Pressure Chemical Ionization. *Anal. Chem.* **2012**, 84, 10657-10664.

(87) Ding, X.; Garikapati, V.; Spengler, B., et al., Analysis of ketone-based neurosteroids by reactive low-temperature plasma mass spectrometry. *Rapid Commun. Mass Spectrom.* **2018**, 32, 1439-1450.

(88) Kumano, S.; Sugiyama, M.; Yamada, M., et al., Development of a portable mass spectrometer characterized by discontinuous sample gas

introduction, a low-pressure dielectric barrier discharge ionization source, and a vacuumed headspace technique. *Anal. Chem.* **2013**, 85, 5033-5039.

(89) Zhang, J. I.; Tao, W. A.; Cooks, R. G. Facile determination of double bond position in unsaturated fatty acids and esters by low temperature plasma ionization mass spectrometry. *Anal. Chem.* **2011**, 83, 4738-4744.

(90) Ahmed, E.; Xiao, D.; Dumlao, M. C., et al., Nanosecond Pulsed Dielectric Barrier Discharge Ionization Mass Spectrometry. *Anal. Chem.* **2020**, 92, 4468-4474.

(91) Dumlao, M.; Khairallah, G. N.; Donald, W. A. Internal Energy Deposition in Dielectric Barrier Discharge Ionization is Significantly Lower than in Direct Analysis in Real-Time Mass Spectrometry. *Aust. J. Chem.* **2017**, 70, 1219-1226.

(92) Lara-Ortega, F. J.; Robles-Molina, J.; Brandt, S., et al., Use of dielectric barrier discharge ionization to minimize matrix effects and expand coverage in pesticide residue analysis by liquid chromatography-mass spectrometry. *Anal. Chim. Acta* **2018**, 1020, 76-85.

(93) Zhang, H.; He, J.; Qiao, L., et al., Doped Argon Surface Desorption Dielectric-Barrier Discharge Ionization Mass Spectrometry for Fragile Compounds. *Anal. Chem.* **2018**, 90, 9033-9039.

(94) Gyr, L.; Klute, F. D.; Franzke, J., et al., Characterization of a Nitrogen-Based Dielectric Barrier Discharge Ionization Source for Mass Spectrometry Reveals Factors Important for Soft Ionization. *Anal. Chem.* **2019**, 91, 6865-6871.

(95) Gyr, L.; Wolf, J. C.; Franzke, J., et al., Mechanistic Understanding Leads to Increased Ionization Efficiency and Selectivity in Dielectric Barrier Discharge Ionization Mass Spectrometry: A Case Study with Perfluorinated Compounds. *Anal. Chem.* **2018**, 90, 2725-2731.

(96) Huba, A. K.; Mirabelli, M. F.; Zenobi, R. High-throughput screening of PAHs and polar trace contaminants in water matrices by direct solid-phase microextraction coupled to a dielectric barrier discharge ionization source. *Anal. Chim. Acta* **2018**, 1030, 125-132.

(97) Huba, A. K.; Mirabelli, M. F.; Zenobi, R. Understanding and Optimizing the Ionization of Polycyclic Aromatic Hydrocarbons in Dielectric Barrier Discharge Sources. *Anal. Chem.* **2019**, 91, 10694-10701.

(98) Liu, Q.; Zenobi, R. Rapid Analysis of Fragrance Allergens by Dielectric Barrier Discharge Ionization Mass Spectrometry. *Rapid Commun. Mass Spectrom.* **2020**, e9021.

(99) Mirabelli, M. F.; Gionfriddo, E.; Pawliszyn, J., et al., A quantitative approach for pesticide analysis in grape juice by direct interfacing of a matrix compatible SPME phase to dielectric barrier discharge ionization-mass spectrometry. *Analyst* **2018**, 143, 891-899.

(100) Mirabelli, M. F.; Wolf, J. C.; Zenobi, R. Pesticide analysis at ppt concentration levels: coupling nano-liquid chromatography with dielectric barrier discharge ionization-mass spectrometry. *Anal. Bioanal. Chem.* **2016**, 408, 3425-3434.

(101) Wolf, J. C.; Gyr, L.; Mirabelli, M. F., et al., A Radical-Mediated Pathway for the Formation of [M + H](+) in Dielectric Barrier Discharge Ionization. *J. Am. Soc. Mass Spectrom.* **2016**, 27, 1468-1475.

(102) Wolf, J. C.; Schaer, M.; Siegenthaler, P., et al., Direct quantification of chemical warfare agents and related compounds at low ppt levels: comparing active capillary dielectric barrier discharge plasma ionization and secondary electrospray ionization mass spectrometry. *Anal. Chem.* **2015**, 87, 723-729.

(103) Schwartz, J. C.; Senko, M. W.; Syka, J. E. P. A two-dimensional quadrupole ion trap mass spectrometer. *J. Am. Soc. Mass Spectrom.* **2002**, 13, 659-669.

(104) Scigelova, M.; Makarov, A. Orbitrap Mass Analyzer – Overview and Applications in Proteomics. *Proteomics* **2006**, 6, 16-21.

(105) Makarov, A.; Denisov, E.; Kholomeev, A., et al., Performance Evaluation of a Hybrid Linear Ion Trap/Orbitrap Mass Spectrometer. *Anal. Chem.* **2006**, 78, 2113-2120.

(106) Ackermann, M. A functional perspective on phenotypic heterogeneity in microorganisms. *Nat. Rev. Microbiol.* **2015**, 13, 497-508.

(107) Jindal, A.; Gupta, P.; Jayadeva, et al., Discovery of rare cells from voluminous single cell expression data. *Nat. Commun.* **2018**, 9, 4719.

(108) Alix-Panabières, C.; Pantel, K. Clinical Applications of Circulating Tumor Cells and Circulating Tumor DNA as Liquid Biopsy. *Cancer Discovery* **2016**, 6, 479.

(109) Lawson, D. A.; Bhakta, N. R.; Kessenbrock, K., et al., Single-cell analysis reveals a stem-cell program in human metastatic breast cancer cells. *Nature* **2015**, 526, 131-135.

(110) Heath, J. R.; Ribas, A.; Mischel, P. S. Single-cell analysis tools for drug discovery and development. *Nat. Rev. Drug Discov.* **2016**, 15, 204-216.

(111) Stuart, T.; Satija, R. Integrative single-cell analysis. *Nat. Rev. Genet.* **2019**, 20, 257-272.

(112) Davis, R. T.; Blake, K.; Ma, D., et al., Transcriptional diversity and bioenergetic shift in human breast cancer metastasis revealed by single-cell RNA sequencing. *Nat. Cell Biol.* **2020**, 22, 310-320.

(113) Hanahan, D.; Weinberg, Robert A. Hallmarks of Cancer: The Next Generation. *Cell* **2011**, 144, 646-674.

(114) Pavlova, Natalya N.; Thompson, Craig B. The Emerging Hallmarks of Cancer Metabolism. *Cell Metab.* **2016**, 23, 27-47.

(115) Rawla, P.; Sunkara, T.; Gaduputi, V. Epidemiology of Pancreatic Cancer: Global Trends, Etiology and Risk Factors. *World J. Oncol.* **2019**, 10, 10-27.

(116) Chang, H.-H.; Moro, A.; Takakura, K., et al., Incidence of pancreatic cancer is dramatically increased by a high fat, high calorie diet in KrasG12D mice. *PLoS ONE* **2017**, 12, e0184455.

(117) Fan, J.; Slowikowski, K.; Zhang, F. Single-cell transcriptomics in cancer: computational challenges and opportunities. *Exp. Mol. Med.* **2020**, 52, 1452-1465.

(118) Suva, M. L.; Tirosh, I. Single-Cell RNA Sequencing in Cancer: Lessons Learned and Emerging Challenges. *Mol. Cell* **2019**, 75, 7-12.

(119) Lim, H.; Lee, S. Y.; Park, Y., et al., Mass spectrometry imaging of untreated wet cell membranes in solution using single-layer graphene. *Nat. Methods* **2021**, 18, 316-320.

(120) Amantonico, A.; Oh, J. Y.; Sobek, J., et al., Mass spectrometric method for analyzing metabolites in yeast with single cell sensitivity. *Angew. Chem., Int. Ed.* **2008**, 47, 5382-5385.

(121) Kompauer, M.; Heiles, S.; Spengler, B. Atmospheric pressure MALDI mass spectrometry imaging of tissues and cells at 1.4-mum lateral resolution. *Nat. Methods* **2017**, 14, 90-96.

(122) Onjiko, R. M.; Moody, S. A.; Nemes, P. Single-cell mass spectrometry reveals small molecules that affect cell fates in the 16-cell embryo. *Proc Natl Acad Sci U S A* **2015**, 112, 6545-6550.

(123) Pan, N.; Standke, S. J.; Kothapalli, N. R., et al., Quantification of Drug Molecules in Live Single Cells Using the Single-Probe Mass Spectrometry Technique. *Anal. Chem.* **2019**, 91, 9018-9024.

(124) Liu, R.; Pan, N.; Zhu, Y., et al., T-Probe: An Integrated Microscale Device for Online In Situ Single Cell Analysis and Metabolic Profiling Using Mass Spectrometry. *Anal. Chem.* **2018**, 90, 11078-11085.

(125) Lombard-Banek, C.; Moody, S. A.; Nemes, P. Single-Cell Mass Spectrometry for Discovery Proteomics: Quantifying Translational Cell Heterogeneity in the 16-Cell Frog (Xenopus) Embryo. *Angew. Chem., Int. Ed.* **2016**, 55, 2454-2458.

(126) Lombard-Banek, C.; Moody, S. A.; Manzini, M. C., et al., Microsampling Capillary Electrophoresis Mass Spectrometry Enables Single-Cell Proteomics in Complex Tissues: Developing Cell Clones in Live Xenopus laevis and Zebrafish Embryos. *Anal. Chem.* **2019**, 91, 4797-4805.

(127) Jackson, H. W.; Fischer, J. R.; Zanotelli, V. R. T., et al., The single-cell pathology landscape of breast cancer. *Nature* **2020**, 578, 615-620.

(128) Wagner, J.; Rapsomaniki, M. A.; Chevrier, S., et al., A Single-Cell Atlas of the Tumor and Immune Ecosystem of Human Breast Cancer. *Cell* **2019**, 177, 1330-1345 e1318.

(129) Bregy, L.; Sinues, P. M.; Nudnova, M. M., et al., Real-time breath analysis with active capillary plasma ionization-ambient mass spectrometry. *J Breath Res* **2014**, 8, 027102.

(130) Zhang, J. I.; Tao, W. A.; Cooks, R. G. Facile determination of double bond position in unsaturated fatty acids and esters by low temperature plasma ionization mass spectrometry. *Anal. Chem.* **2011**, 83, 4738-4744.

(131) Gilbert-Lopez, B.; Geltenpoth, H.; Meyer, C., et al., Performance of dielectric barrier discharge ionization mass spectrometry for pesticide testing: a comparison with atmospheric pressure chemical ionization and electrospray ionization. *Rapid Commun. Mass Spectrom.* **2013**, 27, 419-429.

(132) Huba, A. K.; Mirabelli, M. F.; Zenobi, R. High-throughput screening of PAHs and polar trace contaminants in water matrices by direct solid-phase

microextraction coupled to a dielectric barrier discharge ionization source. *Anal. Chim. Acta* **2018**, 1030, 125-132.

(133) Liu, Q.; Zenobi, R. Rapid Analysis of Fragrance Allergens by Dielectric Barrier Discharge Ionization Mass Spectrometry. *Rapid Commun. Mass Spectrom.* **2020**, e9021.

(134) Swierczynski, J.; Hebanowska, A.; Sledzinski, T. Role of abnormal lipid metabolism in development, progression, diagnosis and therapy of pancreatic cancer. *World J. Gastroenterol.* **2014**, 20, 2279-2303.

(135) Carrer, A.; Trefely, S.; Zhao, S., et al., Acetyl-CoA Metabolism Supports Multistep Pancreatic Tumorigenesis. *Cancer Discovery* **2019**, 9, 416.

(136) Adusumilli, R.; Mallick, P. In *Proteomics: Methods and Protocols*; Comai, L., Katz, J. E., Mallick, P., Eds.; Springer New York: New York, NY, 2017, p 339-368.

(137) Raphael, B. J.; Hruban, R. H.; Aguirre, A. J., et al., Integrated Genomic Characterization of Pancreatic Ductal Adenocarcinoma. *Cancer Cell* **2017**, 32, 185-203.e113.

(138) Covarrubias, A. J.; Aksoylar, H. I.; Yu, J., et al., Akt-mTORC1 signaling regulates Acly to integrate metabolic input to control of macrophage activation. *eLife* **2016**, 5, e11612.

(139) Hatzivassiliou, G.; Zhao, F.; Bauer, D. E., et al., ATP citrate lyase inhibition can suppress tumor cell growth. *Cancer Cell* **2005**, 8, 311-321.

(140) Huang, L.; Fang, M.; Cupp-Sutton, K. A., et al., Spray-Capillary-Based Capillary Electrophoresis Mass Spectrometry for Metabolite Analysis in Single Cells. *Anal. Chem.* **2021**, 93, 4479-4487.

(141) Li, Z.; Wang, Z.; Pan, J., et al., Single-cell mass spectrometry analysis of metabolites facilitated by cell electro-migration and electroporation. *Anal. Chem.* **2020**, 92, 10138-10144.

(142) Li, Z.; Cheng, S.; Lin, Q., et al., Single-cell lipidomics with high structural specificity by mass spectrometry. *Nat. Commun.* **2021**, 12, 2869.

(143) Liu, F. L.; Ye, T. T.; Ding, J. H., et al., Chemical Tagging Assisted Mass Spectrometry Analysis Enables Sensitive Determination of Phosphorylated Compounds in a Single Cell. *Anal. Chem.* **2021**, 93, 6848-6856.

(144) Neumann, E. K.; Ellis, J. F.; Triplett, A. E., et al., Lipid Analysis of 30000 Individual Rodent Cerebellar Cells Using High-Resolution Mass Spectrometry. *Anal. Chem.* **2019**, 91, 7871-7878.

(145) Lanni, E. J.; Dunham, S. J.; Nemes, P., et al., Biomolecular imaging with a C60-SIMS/MALDI dual ion source hybrid mass spectrometer: instrumentation, matrix enhancement, and single cell analysis. *J. Am. Soc. Mass Spectrom.* **2014**, 25, 1897-1907.

(146) Zhuang, M.; Hou, Z.; Chen, P., et al., Introducing charge tag via click reaction in living cells for single cell mass spectrometry. *Chem. Sci.* **2020**, 11, 7308-7312.

(147) Kompauer, M.; Heiles, S.; Spengler, B. Atmospheric pressure MALDI mass spectrometry imaging of tissues and cells at 1.4-mum lateral resolution. *Nat. Methods* **2017**, 14, 90-96.

(148) Tian, H.; Sparvero, L. J.; Blenkinsopp, P., et al., Secondary-Ion Mass Spectrometry Images Cardiolipins and Phosphatidylethanolamines at the Subcellular Level. *Angew. Chem., Int. Ed.* **2019**, 58, 3156-3161.

(149) Abouleila, Y.; Onidani, K.; Ali, A., et al., Live single cell mass spectrometry reveals cancer-specific metabolic profiles of circulating tumor cells. *Cancer Sci.* **2019**, 110, 697-706.

(150) Fujii, T.; Matsuda, S.; Tejedor, M. L., et al., Direct metabolomics for plant cells by live single-cell mass spectrometry. *Nat. Protoc.* **2015**, 10, 1445-1456.

(151) Tsuyama, N.; Mizuno, H.; Tokunaga, E., et al., Live Single-Cell Molecular Analysis by Video-Mass Spectrometry. *Anal. Sci.* **2008**, 24, 559-561.

(152) Zhang, L.; Foreman, D. P.; Grant, P. A., et al., In situ metabolic analysis of single plant cells by capillary microsampling and electrospray ionization mass spectrometry with ion mobility separation. *Analyst* **2014**, 139, 5079-5085.

(153) Zhang, L.; Khattar, N.; Kemenes, I., et al., Subcellular Peptide Localization in Single Identified Neurons by Capillary Microsampling Mass Spectrometry. *Sci Rep* **2018**, 8, 12227.

(154) Zhang, L.; Vertes, A. Energy Charge, Redox State, and Metabolite Turnover in Single Human Hepatocytes Revealed by Capillary Microsampling Mass Spectrometry. *Anal. Chem.* **2015**, 87, 10397-10405.

(155) Stolee, J. A.; Vertes, A. Toward single-cell analysis by plume collimation in laser ablation electrospray ionization mass spectrometry. *Anal. Chem.* **2013**, 85, 3592-3598.

(156) Stopka, S. A.; Wood, E. A.; Khattar, R., et al., High-Throughput Analysis of Tissue-Embedded Single Cells by Mass Spectrometry with Bimodal Imaging and Object Recognition. *Anal. Chem.* **2021**, 93, 9677-9687.

(157) Lombard-Banek, C.; Moody, S. A.; Manzini, M. C., et al., Microsampling Capillary Electrophoresis Mass Spectrometry Enables Single-Cell Proteomics in Complex Tissues: Developing Cell Clones in Live Xenopus laevis and Zebrafish Embryos. *Anal. Chem.* **2019**, 91, 4797-4805.

(158) Lombard-Banek, C.; Moody, S. A.; Nemes, P. Single-Cell Mass Spectrometry for Discovery Proteomics: Quantifying Translational Cell Heterogeneity in the 16-Cell Frog (Xenopus) Embryo. *Angew. Chem., Int. Ed.* **2016**, 55, 2454-2458.

(159) Onjiko, R. M.; Moody, S. A.; Nemes, P. Single-cell mass spectrometry reveals small molecules that affect cell fates in the 16-cell embryo. *Proc. Natl. Acad. Sci. U. S. A.* **2015**, 112, 6545-6550.

(160) Lombard-Banek, C.; Li, J.; Portero, E. P., et al., In Vivo Subcellular Mass Spectrometry Enables Proteo-Metabolomic Single-Cell Systems Biology in a Chordate Embryo Developing to a Normally Behaving Tadpole (X. laevis)*. *Angew. Chem., Int. Ed.* **2021**, 60, 12852-12858.

(161) Adamovich, I.; Baalrud, S. D.; Bogaerts, A., et al., The 2017 Plasma Roadmap: Low temperature plasma science and technology. *J. Phys. D: Appl. Phys.* **2017**, 50.

(162) Brandt, S.; Klute, F. D.; Schutz, A., et al., Dielectric barrier discharges applied for soft ionization and their mechanism. *Anal. Chim. Acta* **2017**, 951, 16-31.

(163) Müller, S.; Krähling, T.; Veza, D., et al., Operation modes of the helium dielectric barrier discharge for soft ionization. *Spectrochim. Acta, Part B* **2013**, 85, 104-111.

(164) Cheng, S. C.; Jhang, S. S.; Huang, M. Z., et al., Simultaneous detection of polar and nonpolar compounds by ambient mass spectrometry with a dual electrospray and atmospheric pressure chemical ionization source. *Anal. Chem.* **2015**, 87, 1743-1748.

(165) Barry, J. A.; Robichaud, G.; Bokhart, M. T., et al., Mapping antiretroviral drugs in tissue by IR-MALDESI MSI coupled to the Q Exactive and comparison with LC-MS/MS SRM assay. *J. Am. Soc. Mass Spectrom.* **2014**, 25, 2038-2047.

(166) Rosen, E. P.; Bokhart, M. T.; Ghashghaei, H. T., et al., Influence of Desorption Conditions on Analyte Sensitivity and Internal Energy in Discrete Tissue or Whole Body Imaging by IR-MALDESI. *J. Am. Soc. Mass Spectrom.* **2015**, 26, 899-910.

(167) Stark, A. K.; Meyer, C.; Kraehling, T., et al., Electronic coupling and scaling effects during dielectric barrier electrospray ionization. *Anal. Bioanal. Chem.* **2011**, 400, 561-569.

(168) Huba, A. K.; Mirabelli, M. F.; Zenobi, R. Understanding and Optimizing the Ionization of Polycyclic Aromatic Hydrocarbons in Dielectric Barrier Discharge Sources. *Anal. Chem.* **2019**, 91, 10694-10701.

(169) Yin, R.; Prabhakaran, V.; Laskin, J. Quantitative Extraction and Mass Spectrometry Analysis at a Single-Cell Level. *Anal. Chem.* **2018**, 90, 7937-7945.

(170) Gong, X.; Zhao, Y.; Cai, S., et al., Single cell analysis with probe ESI-mass spectrometry: detection of metabolites at cellular and subcellular levels. *Anal. Chem.* **2014**, 86, 3809-3816.

(171) Varghese, R. S.; Zhou, B.; Nezami Ranjbar, M. R., et al., Ion annotation-assisted analysis of LC-MS based metabolomic experiment. *Proteome Sci.* **2012**, 10 Suppl 1, S8-S8.

(172) Evers, T. M. J.; Hochane, M.; Tans, S. J., et al., Deciphering Metabolic Heterogeneity by Single-Cell Analysis. *Anal. Chem.* **2019**, 91, 13314-13323.

(173) Kim, J.; DeBerardinis, R. J. Mechanisms and Implications of Metabolic Heterogeneity in Cancer. *Cell Metab.* **2019**, 30, 434-446.

(174) Karmaus, P. W. F.; Chen, X.; Lim, S. A., et al., Metabolic heterogeneity underlies reciprocal fates of TH17 cell stemness and plasticity. *Nature* **2019**, 565, 101-105.

(175) Liu, R.; Zhang, G.; Sun, M., et al., Integrating a generalized data analysis workflow with the Single-probe mass spectrometry experiment for single cell metabolomics. *Anal. Chim. Acta* **2019**, 1064, 71-79.

Appendices

A. Mass Spectrometry Reveals High Levels of Hydrogen Peroxide in Pancreatic Cancer Cells

Reactive oxygen species (ROS) are critical for many cellular functions, and dysregulation of ROS involves the development of multiple types of tumors, including pancreatic cancer. However, ROS have been grouped into a single biochemical entity for a long time, and the specific roles of certain types of ROS in tumor cells (e.g., PDAC) have not been systematically investigated. In this work, a highly sensitive and accurate mass spectrometry-based method was applied to study genetically modified animals and human PDAC cells. The results show that the oncogenic *KRAS* mutation promotes the accumulation of hydrogen peroxide (H_2O_2) rather than superoxide or hydroxyl radicals in pancreatic cancer cells. We further identified that the enriched H_2O_2 modifies cellular metabolites and promotes the survival of pancreatic cancer cells. These findings highlight the specific roles of H_2O_2 in pancreatic cancer development, which may provide new directions for pancreatic cancer therapy.

1. Introduction

Reactive oxygen species (ROS), in particular hydrogen peroxide (H_2O_2), superoxide ($\cdot O_2^-$) and hydroxyl radicals ($\cdot OH$), play important roles in tissue homeostasis, cellular signaling, differentiation, and survival.[1-2] ROS dysregulation contributes to the

development of various diseases, including multiple types of cancer.[2] However, whether ROS can prevent or promote the development of cancer remains controversial. Cellular responses to ROS are complex and they usually reflect a complex integration of various ROS types and levels. Therefore, ROS have mostly been studied as a whole, which unavoidably renders the precise roles of various ROS in tumor cells unclear.[3] Early literature showed that ROS play a major role in translational regulation processes as well as metastasis in pancreatic ductal adenocarcinoma (PDAC), which is the most lethal solid tumor.[3-5] More recently, we have studied pancreatic cancer initiation as well as lipid metabolism taking advantage of the genetic animal models and single-cell mass spectrometry.[6-7] However, the specific roles of specific ROS in PDAC remain unclear, which necessitates the use of appropriate assay techniques to study the functions and levels of specific ROS in PDAC.

From the analytical point of view, the detection of ROS is not easy, due to the fact that most oxygen radicals are unstable, short-lived and can interfere with each other. Current methods used to detect ROS include fluorescent[8] and chemiluminescent assays,[9-10] chromatographic[11] and spectrophotometric methods,[12-13] electrochemical biosensors[14-15] as well as electron paramagnetic resonance (EPR).[16] Luminous detection probes are cell-permeable and can form stable adducts. However, these probes lack specificity and sensitivity to the target ROS.[11] In addition, the reaction process and products of chromatography methods are complex. Electrochemical biosensors require complicated preparation, and the types of proteins coated on the electrode surface are limited. EPR analysis is not suitable for detecting intracellular ROS.[17] Alternatively, mass spectrometry (MS) is a promising technique to detect different types of ROS rapidity, and with high selectivity, sensitivity and accuracy. MS has been coupled with liquid

chromatography (LC) to detect 2-hydroxyethidium (2OH-E[+]), the reaction product of $O_2^{\bullet-}$ with the fluorescent probe hydroethidine (HE), and 7-hydroxycoumarin (COH), the reaction product of H_2O_2 with the fluorescent probe coumarin boronic acid (CBA).[18-21] Furthermore, fluorescent probe-based methods usually induce the formation of several adducts that would absorb or emit light at similar wavelengths. MS can accurately detect the mass-to-charge (m/z) ratio of specific adducts, thereby avoiding such interferences. Here, a mass spectrometry-based method was established to specifically measure different types of ROS in PDAC cells. More specifically, we detected the product 2-hydroxyethidium (2OH-E[+]) formed from the reaction of hydroethidine (HE) with $O_2^{\bullet-}$, the product 2,3-DHBA formed from salicylic acid and •OH, and the product 7-hydroxycoumarin (COH) formed from coumarin-7-boronic acid (CBA) and H_2O_2 by mass spectrometry (Figure S1).

Using mass spectrometry for direct infusion of cell lysates, we found that the level of H_2O_2 instead of $\cdot O_2^-$ or •OH, was dysregulated in murine and human PDAC cells. By using genetic techniques, we also showed that the oncogenic KRAS mutation in PDAC cells not only promoted the production of H_2O_2, but also suppressed the catalase (*CAT*) gene expression, which is the specific enzyme that metabolizes H_2O_2. We further monitored the effect of high levels of H_2O_2 on cellular metabolites and cell viability in PDAC cells.

2. Experimental Section

2.1 Chemicals, Materials and cells

Methanol (99.9%), ammonium formate (>99.0%), catalase, N-acetyl-L-cysteine, salicylic acid, hydrogen peroxide and dimethylsulfoxide (DMSO) were purchased from Sigma-Aldrich Chemie GmbH (Buchs, Switzerland). Phosphate Buffer Saline (PBS)

were purchased from Thermo Fisher Scientific (Buchs, Switzerland). Catalase polyclonal antibody was purchased from Proteintech (Rosemont, USA). Hydroethidine (HE) and coumarinboronic acid (CBA) were purchased from Adipogen AG (Liestal, Switzerland). PANC-1, CFPAC-1 BxPC-3 cells were purchased from ATCC. H6c7 was purchased from Kerafast.

2.2 Cell culture

CFPAC-1 and BxPC-3 cells were maintained in RPMI-1640 medium supplemented with 10% (v/v) fetal bovine serum and 1% Penicillin-Streptomycin (P/S). PANC-1 was maintained in high glucose DMEM supplied with 10% (v/v) fetal bovine serum and 1% Penicillin-Streptomycin (P/S). H6c7 was maintained in a keratinocyte serum-free medium following the manufacturer's instructions (Keragast, Cat#ECA001-FP).

The cells were cultured at 37°C in the humidified incubator (Thermo Fisher Scientific) with 5% CO_2.

2.3 In vivo animal studies

All animal experiments were in accordance with institutional guidelines and approved by the Kantonale Veterinäramt Zürich (Project license: ZH184/2018, ZH043/2019). Mice were housed in a pathogen-free animal facility at the Institute of Molecular Systems Biology at ETH Zurich. The animals were maintained in a temperature-controlled room (22°C), with humidity at 55% and on a 12 h light-dark cycle (lights on from 6 a.m. to 6 p.m.). Mice were fed a standard laboratory chow diet and water ad libitum, and the age of the mice is indicated in the Figures. Both male and female mice were used in this study.

Kras^{G12D} and *Ptf1a^{Cre}* GEMMs have been described before[22-23]. All mice were maintained on a mixed background. The genotyping results are showed in the supplemental information (Fig.S1). The related genotyping primers (5'-3'):

Ptf1^{cre}_1   ATAGGCTACCTGGCCATGC

Ptf1^{cre}_2   GGGCTGCAGGAATTCGTCG

Jax Kras WT_F   TGT CTT TCC CCA GCA CAG T

Jax Kras common_R   CTG CAT AGT ACG CTA TAC CCT GT

Jax Kras Mut_F   GCA GGT CGA GGG ACC TAA TA

Primary pancreatic acinar cell isolation method can be found in our previous work.[6]

2.4 Histology

Tissues were fixed with 4% PFA overnight, then embedded in paraffin follow standard protocol and sectioned at the thickness of 3.5 μm. Haematoxylin and eosin staining were performed using the standard protocol.

2.5 Mouse primary acinar cell isolation

Mice were sacrificed, sprayed with 70% EtOH and the pancreas was dissected. The pancreas was digested with 0.5 mL 2 mg/mL collagenase P at 37°C for 25 min with shake. Digestion was stopped by washing with ice-cold 1xHBSS supplemented with 5% FBS. Filter the cells through 500 μm and 100 μm mesh. The resulting cells were gently loaded on top of 50 mL falcon tube containing 20 mL 1xHBSS plus with 30% FBS. Primary acini clusters were pelleted by centrifugation at 67.08 xg for 2 min.

2.6 Catalase treatment of PANC-1 and BxPC-3 cells (negative control experiment for COH formation)

The cells were maintained until the they reached 80% confluence. Then 500 Units/mL catalase (Sigma Aldrich, Cat#C9322, dissolved in 50 mM potassium phosphate buffer at pH 7.0) were added to the fresh cell culture medium. Control cells received 50 mM potassium phosphate buffer treatment. The cells were treated with catalase or 50 mM potassium phosphate buffer for 24 hours followed by mass spectrometry analysis. Cell densities were the same in experimental and control groups.

2.7 Positive control experiment for COH formation

Cells were aliquoted into five 1mL tubes and were centrifuged to remove DMEM. Next, cells were added separately with different concentrations of H_2O_2 (0, 88, 176, 264, 352 μM), and were finally incubated with coumarin-7-boronic acid (CBA) (500 μM) for 30 minutes. After the incubation, the cells were lysed by MeOH and centrifuged (67.08 xg, 4 minutes). The supernatant was collected for COH analysis.

2.8 Cancer Genome Atlas (TCGA) dataset analysis

Gene expression data of normal pancreatic tissues (GTEx; n = 167) and pancreatic ductal adenocarcinoma (TCGA-PDCA; n = 178) were downloaded from UNSC Xena (https://xena.ucsc.edu/). Differential expression analysis was performed using DESeq2. Gene Set Enrichment Analysis (GSEA v3.0) of GO biological processes was performed on normalized counts.[24]

2.9 qPCR

Total RNA was isolated with Trizol following the manufacturer's protocol (Sigma, Cat# T9424). The resulting RNA was treated with DNase I (Thermofisher Scientific, Cat# AM1906). Then the RNA was reverse transcribed using High-Capacity cDNA Reverse Transcription Kit (Thermo Fisher Scientific, Cat# 4368813) by using random primers. Quantitative PCR was performed by KAPA SYBR FAST qPCR assay (Sigma, Cat# KK4611) in a LC480 II Lightcycler (Roche). Results were normalized to 36B4 or GAPDH mRNA levels.

qPCR primer information (5'-3'):

mus_*cat*_F	CAAGATTGCCTTCTCCGGGT
mus_*cat*_R	CAGGACATCAGGTCTCTGCG
mus_*sod*1_F	CATGGCGATGAAAGCGGTG
mus_*sod*1_R	GCACTGGTACAGCCTTGTGTA
mus_*gpx4*_F	CCGTCTGAGCCGCTTACTT
mus_*gpx4*_R	ATGCACACGAAACCCCTGTA
homo_*SOD1*_F	CCTAGCGAGTTATGGCGACG
homo_*SOD1*_R	AGTCTCCAACATGCCTCTCTTC
homo_*CAT*_F	CTCCGGAACAACAGCCTTCT
homo_*CAT*_R	ATAGAATGCCCGCACCTGAG
homo_*GPX4*_F	AGGGCATCCTGGGAAATG
homo_*GPX4*_R	GGGGCAGGTCCTTCTCTATC

2.10 MTT assay

Cell viability was determined by MTT [3-(4,5-dimethyl-2-thiazolyl)-2,5- diphenyl-2H-tetrazoliumbromid] (Sigma, Cat# M5655) assay after treated with catalase and 50 mM potassium phosphate buffer for 24 hours. Briefly, MTT solution in 1x PBS was added to each well of 96 well-plate at the final concentration of 0.5 mg/mL. The plate was protected from light and incubated for 3 hours at 37 °C. The medium was then aspirated and the dark-blue formazan was dissolved with dimethylsulfoxide (DMSO, Sigma, Cat# D4540). Optical density was measured with a spectrometer at 490 nm. The raw luminescence data were normalized to the adenovirus control.

2.11 Immunoblots (IB)

Cells were lysed in RIPA buffer (150 mM sodium chloride, 50 mM Tris-HCl pH7.4, 0.1% SDS, 1 mM EDTA, 1% NP-40, 0.5% sodium deoxycholate) freshly supplied with protease inhibitors cocktail and PhosSTOP. The protein concentration was determined using the Bradford protein assay. Equal amount of proteins was subjected to 10-15% SDS-PAGE analysis. The immune signal was detected by the ECL kit (Thermo Scientific). The amounts of protein were quantified by Image J software.

Antitbodies used in this study:

Phos-Erk1/2   Cell signalling, Cat# 4370, RRID:AB_2315112

Erk1/2   Cell signalling, Cat# 4695s, RRID:AB_390779

HA-tag   Cell signalling, Cat# 3724, RRID:AB_1549585

KRAS   Santa Cruz, Cat# sc-30, RRID:AB_627865

GAPDH   Sigma, Cat # G9545, RRID:AB_796208

HSP90   Cell signaling, Cat# 4874s, RRID:AB_2121214

Cleved caspase 3   Cell   signaling,   Cat#   9661s,
RRID:AB_2341188

2.12 Mass spectrometry analysis of H_2O_2 at the population level

Cells were incubated with Coumarin-7-boronic acid (CBA) (500 μM) for 30 minutes to enable the full reaction between CBA and H_2O_2 in the cells to produce 7-hydroxycoumarin (COH) (Figure S2a). After the incubation, DMEM was removed by centrifugation (67.08 xg, 4 minutes), and the cells were resuspended in PBS. Then the cells were centrifuged again (67.08 xg, 4 minutes) to remove PBS, and lysed by MeOH. After centrifugation at 3286.92 xg for 5 min at 4 °C, the supernatant was collected for COH analysis.

2.13 Mass spectrometry analysis of •OH at the population level

Cells were incubated with salicylic acid (500 μM) for 30 minutes to enable the full reaction between salicylic acid and •OH in the cells to produce 2,3-DHBA (Figure S2b). After the incubation, DMEM was removed by centrifugation (67.08 xg, 4 minutes), and the cells were resuspended in PBS. Then the cells were centrifuged again (67.08 xg, 4 minutes) to remove PBS, and lysed by MeOH. After centrifugation at 3286.92 xg for 5 min at 4 °C, the supernatant was collected for 2,3-DHBA analysis.

2.14 Mass spectrometry analysis of $O_2^{\bullet-}$ at the population level

Cells were incubated with hydroethidine (HE) (500 µM) for 30 minutes to enable the full reaction between HE and $O_2^{\bullet-}$ in the cells to produce 2-hydroxyethidium ($2OH-E^+$) (Figure S2c). After the incubation, DMEM was removed by centrifugation (67.08 xg, 4 minutes), and the cells were resuspended in PBS. Then the cells were centrifuged again (67.08 xg, 4 minutes) to remove PBS, and lysed by MeOH. After centrifugation at 3286.92 xg for 5 min at 4 °C, the supernatant was collected for $2OH-E^+$ analysis.

2.15 Analysis of metabolites in cell lysates

Cells were centrifuged (67.08 xg, 4 minutes) to remove DMEM and were resuspended in PBS. PBS was then removed by centrifugation (67.08 xg, 4 minutes), and lysed by MeOH. After centrifugation at 3286.92 xg for 5 min at 4 °C, the supernatant was diluted by MeOH: water=1:1(v/v) and collected for metabolites analysis.

2.16 Mass Spectrometry

Mass spectra were acquired in positive ion mode, with an LTQ Orbitrap mass spectrometer (Thermo Fischer Scientific, San Jose, U.S.A.), in fullscan mode at a resolution of 30,000 FWHM (at m/z 400) with a mass tolerance specified to be < 10 ppm. The mass-to-charge range was set to 100–1000, capillary voltage is 50 V, tube lens voltage is 120 V, capillary temperature is 320℃, AGC target = 10^6. Mass spectra were acquired using 1 microscans and a maximum injection time of 10 ms.

2.17 Data analysis

The raw MS data generated from the mass spectrometer was recorded with Xcalibur™ version 2.2 software (Thermo Fisher Scientific, San Jose, U.S.A.). The MSConvert software (ProteoWizard, v3.0)[25] was used to convert MS raw data (.raw) to mzML format. The converted mzML format file is imported into R (version 4.0.2 (2020-06-22)),[26] and preprocessed using self-developed R code with the package MALDIquant for the preprocessing steps. All the spectra from a sample were integrated and the intensity was averaged for each detected peak, signal to noise ratio of 3 was used for peak picking, peak alignment and binning were done on all the processed files. From this procedure, a matrix containing the relevant information was obtained for every condition. Spectra were normalized using lipids signals, 782.57 (PC(36:4)) for cell lines and 780.55 (PC(34:2)) for mice cells. After normalization, intensities were log2 transformed. Two-sided T-test was made for three repetitions for each condition for each cell type. Fold change was also calculated and the information obtained was used to do the volcano plots, and constructed with the package EnhancedVolcano. Significative features were selected as those with a P-value lower than 0.05, and a fold change higher than 2 or lower than -2. Using the information from MS/MS, a few metabolites were assigned and bar plots with dots were done for the compounds, each dot represents the average normalized intensity of a biological replicate, and the bar is the mean value, the error bars present the standard deviation of the three samples, the graphs were designed with the program Prism (Graph Pad v9.4.1).

2.18 Metabolite assignments

Preliminary peak assignments were done by comparing the observed accurate m/z values with the theoretical mass in online databases, including the Human Metabolome Database (http://www.hmdb.ca/), LIPID MAPS (http://www.lipidmaps.org) and the METLIN metabolite database (https://metlin.scripps.edu/). The MS/MS spectra of specific parent ions obtained by ESI-MS were then used to confirm the assignment of metabolites by matching the characteristic product ions to MS/MS spectra in the databases, see Figure S6 and Table S1.

3. Results and Discussion

3.1 Mass Spectrometry Reveals High Levels of H_2O_2 in Pancreatic Cancer.

In order to study different ROS species in PDAC, the state-of-art pancreatic cancer model *Kras*[G12D/+] *Ptf1a*[Cre/+] (KC) was used (Figures 1a and S2). Mice pancreatic tissue was collected for histological and mass spectrometric analysis (Figure 1b). By haematoxylin and eosin (H&E) staining, we found that one-month-old KC mice already showed clear signs of cancer initiation as there are some acinar-to-ductal-metaplasia (ADM) lesions, but the progression of PDAC was much more aggressive in 6-month-old KC mice than one-month-old KC mice (Figures 1c-f), consistent with our previous work.[6] Importantly, by using electrospray (ESI)-MS, we found H_2O_2 to increase around 2.5-fold in freshly isolated primary acinar cells from 6 months-old KC mice compared to littermate controls (Figure 1i). In contrast, $O_2{}^{•-}$ and $•OH$ levels remain almost unchanged in KC animals when compared to their littermate controls (Figures 1g and

h). Furthermore, the effect of aging[27] on the release of H_2O_2 by mitochondria was also observed in KC mice (Figure 1j).

These interesting findings in KC mice encouraged us to monitor different ROS species in human cells. We found that H_2O_2 instead of $\cdot O_2^-$ or $\cdot OH$ increased around 10-fold in human PDAC cells (PANC-1 cells and CFPAC-1 cells) compared to normal human pancreatic H6C7 cells (Figures 1k-m).

To verify that COH is the reaction product formed by CBA and H_2O_2, we added 500 μM CAB and different concentrations of H_2O_2 to cell lysates, as shown in Figure S3. The intensity of COH increased linearly with increasing H_2O_2 concentration. To confirm that H_2O_2 was indeed the oxidant we measured by ESI-MS, we added H_2O_2 specific inhibitor catalase to eliminate H_2O_2, and found that the oxidation of CBA to COH was suppressed (Figure S4), supporting the notion that CBA did not react with other species. These observations support that H_2O_2, rather than the other two ROS, is dysregulated in both mouse and human pancreatic cancer cells.
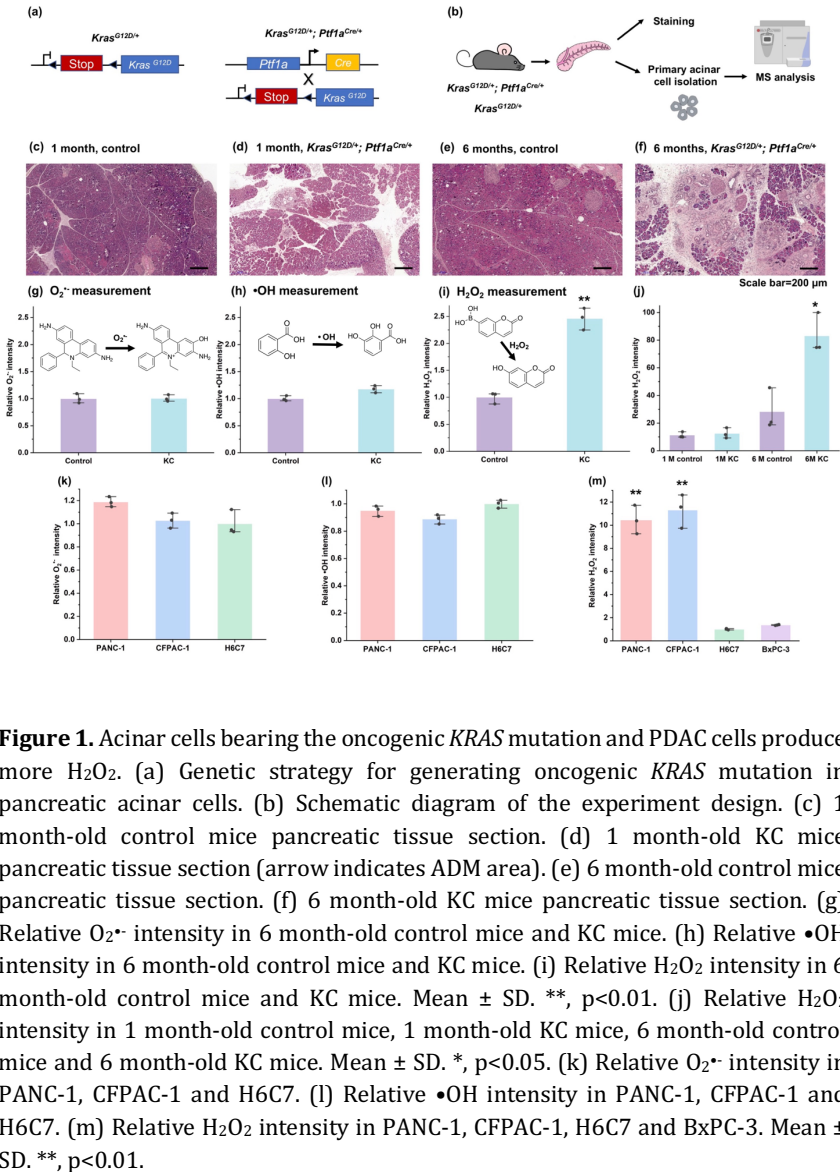
Figure 1. Acinar cells bearing the oncogenic *KRAS* mutation and PDAC cells produce more H_2O_2. (a) Genetic strategy for generating oncogenic *KRAS* mutation in pancreatic acinar cells. (b) Schematic diagram of the experiment design. (c) 1 month-old control mice pancreatic tissue section. (d) 1 month-old KC mice pancreatic tissue section (arrow indicates ADM area). (e) 6 month-old control mice pancreatic tissue section. (f) 6 month-old KC mice pancreatic tissue section. (g) Relative $O_2^{•-}$ intensity in 6 month-old control mice and KC mice. (h) Relative •OH intensity in 6 month-old control mice and KC mice. (i) Relative H_2O_2 intensity in 6 month-old control mice and KC mice. Mean ± SD. **, $p<0.01$. (j) Relative H_2O_2 intensity in 1 month-old control mice, 1 month-old KC mice, 6 month-old control mice and 6 month-old KC mice. Mean ± SD. *, $p<0.05$. (k) Relative $O_2^{•-}$ intensity in PANC-1, CFPAC-1 and H6C7. (l) Relative •OH intensity in PANC-1, CFPAC-1 and H6C7. (m) Relative H_2O_2 intensity in PANC-1, CFPAC-1, H6C7 and BxPC-3. Mean ± SD. **, $p<0.01$.

162

3.2 *KRAS^G12D* Mutations Produce More H_2O_2 and Reduce *CAT* Expression Levels in PDAC Cells.

Oncogenic *KRAS* mutations were well-documented as driving oncogenic events in pancreatic cancer[28]. We found that mice with *KRAS* mutations harbour more H_2O_2 than mice without *KRAS* mutations (Figure 1i). Moreover, *KRAS* wildtype BxPC-3 and H6C7 cells harbour much less H_2O_2 compared to the *KRAS* mutant PANC-1 as well as CFPAC-1 cells (Figure 1m). Therefore, we speculated that the *KRAS* mutation may be the reason for the enrichment of H_2O_2 in PDAC cells. To this end, we re-expressed the *KRAS^G12D* gene in BxPC-3 cells and found the activation of KRAS-Erk signalling (Figure 2a). As expected, the intensity of H_2O_2 in BxPC-3 was significantly increased, roughly 2-fold, in the *KRAS^G12D*–expressed group compared to the empty vector group (Figure 2b), which suggested that the oncogenic *KRAS* mutation led to the production of H_2O_2 in PDAC cells.

Superoxidase dismutase (*SOD*), *CAT* (Catalase) and glutathione peroxidase (*GPx)* are genes associated with H_2O_2 production and consumption[29]. $O_2^{\bullet-}$ is converted into H_2O_2 by *SOD*, and H_2O_2 is converted into water by *CAT* or *GPx* (Figure 2c). We found that the mRNA levels of *SOD* and *GPx* were not regulated by the oncogenic *KRAS* mutation, but the levels of *CAT* were controlled by the oncogenic *KRAS* mutation in both KC mice and BxPC-3 cells (Figures 2d-f). We further investigated the relevance of *CAT* levels in human PDAC, using 178 PDAC and 167 normal pancreatic tissue datasets from The Cancer Genome Atlas (TCGA) and the Genotype-Tissue Expression (GTEx) projects, respectively. As expected, we found that the expression levels of *CAT* decreased around 40% in human PDAC biopsies (Figure 2g). These data suggest that oncogenic *KRAS* mutations not only produce more H_2O_2, but also silence *CAT* expression levels in PDAC cells.
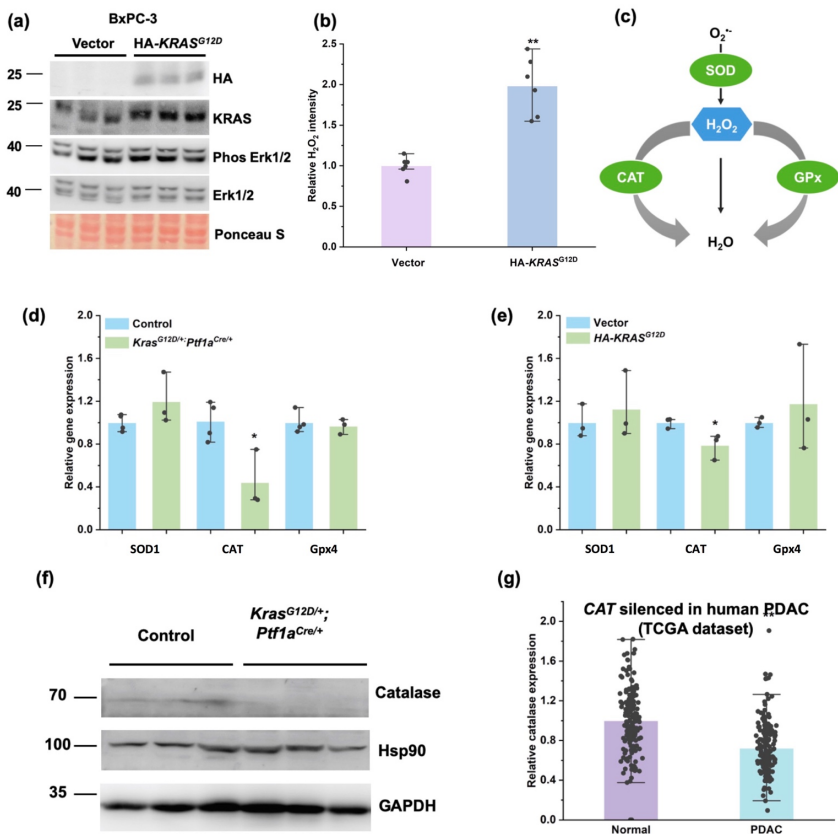
Figure 2. *KRAS^{G12D}* mutations produce more H_2O_2 and suppress *CAT* expression levels in PDAC cells. (a) Immunoblot (IB) analysis of total cell lysate isolated from BxPC-3 cells transfected with pBaBe-Vector and pBaBe-HA-*KRAS^{G12D}* plasmids by Lipofectamine 2000 for 48 hours. HA and KRAS antibodies were used to monitor the HA-*KRAS^{G12D}* expression efficiency. Erk1/2 and phos-Erk1/2 antibodies were used to detect the activity of the main downstream signaling pathway of KRAS. Ponceau S is used as a protein loading control. (b) Relative H_2O_2 intensity analysis in BxPC-3 cells described in (a). Mean ± SD.**, *p*<0.01. (c) The relationship between H_2O_2 and SOD1, CAT and Gpx4. (d) Relative *SOD1*, *CAT* and *Gpx4* expression levels in 6-month-old control and KC mice. Mean ± SD. *, *p*<0.05. (e) Relative *SOD1*, *CAT* and *Gpx4* expression levels in BxPC-3 cells described in (a). Mean ± SD. *, *p*<0.05. (f)

164

IB analysis of the total cell lysate derived from 6-month-old control and KC mice. Hsp90 and GAPDH were used as a protein loading control. (g) Relative *CAT* expression in TCGA and GTEx dataset. Mean ± SD. **, *p*<0.01. (178 PDAC tissue samples were from TCGA dataset, 167 normal pancreatic tissue samples were from GTEx dataset)

3.3 Enriched H_2O_2 Modifies Metabolites in Pancreatic Cancer Cells.

The effect of ROS on lipids and other metabolites has been widely reported[30]. We also reported that lipids metabolism was dysregulated in PDAC[7]. Thus, we hypothesized that increased H_2O_2 levels may affect the metabolites in PDAC cells. To this end, we investigated the effect of H_2O_2 inhibition by catalase on chemical modifications of metabolites in pancreatic cancer cells, including PANC-1, BxPC-3 and KC mice, using ESI-MS. Mass spectra of PANC-1, BxPC-3 and KC mice, as well as PANC-1, BxPC-3 and KC mice treated with catalase are shown in Figure 3.

We performed MS/MS on the 50 most intense signals from each cell lysate in an attempt to identify key metabolites. Positive identifications, based also on agreement with MS/MS data in databases, are shown in Figure S6 and in Table S1. As shown in Figures 3a and b, PC(34:1) (m/z 760.59, [M+H]+), PC(36:4) (m/z 782.57, [M+H]+) and PC(38:5) (m/z 808.58, [M+H]+) are the three predominant lipids in PANC-1. However, when PANC-1 cells were treated with catalase, the lipid profile changed dramatically. For instance, the intensity of PC(38:5) was higher than that of PC(34:1) before catalase treatment, whereas the intensity of PC(38:5) became lower than that of PC(34:1) after treatment with catalase. In contrast, Figure S5a and b show that, compared with the mass spectrum of BxPC-3, the mass spectrum of BxPC-3 cells treated with catalase does not change significantly. In addition to cell lines, we also detected lipid modifications in KC mice and control mice (Figure 3h and i). We found that PC(34:2) (m/z 780.55) and PC(38:7) (m/z

804.55) were the predominant lipids in control mice and KC mice, but their distribution is different. For example, the intensity of PC(34:2) was higher than that of PC(38:7) in control mice, while the intensity of PC(34:2) was lower than that of PC(38:7) in KC mice. The mass spectra of PANC-1 cells and acinar cells with KRAS mutation show a very clear change after suppressing H_2O_2, but the mass spectra of BxPC-3 cells without the KRAS mutation did not change significantly after the H_2O_2 was suppressed.

To clearly demonstrate the effect of H_2O_2 on metabolites in cells, we used volcano plots to visualize the significantly different features in PACN-1 cells and PACN-1 cells treated with catalase (Figure 3c), and in control mice and KC mice (Figure 3j). For example, valine (m/z 140.07, [M+Na]+), nordeoxycholic acid (m/z 379.28, [M+H]+), LysoPC(18:3) (m/z 518.32, [M+H]+) and PC(40:4) (m/z 860.61, [M+Na]+) displayed statistically significant differences between the PACN-1 cells and PACN-1 cells treated with catalase (Figures 3d-g). In control mice and KC mice, for instance, valine (m/z 140.07, [M+Na]+), nordeoxycholic acid (m/z 379.28, [M+H]+), palmitoylcarnitine (m/z 400.34, [M+H]+) and PC(30:2) (m/z 724.49, [M+Na]+) are metabolites with statistical differences between normal acinar cells and acinar cells bearing the oncogenic *KRAS* mutation (Figures 3k-n). MS/MS data on some of these compounds can be found in Figure S6 and Table S1.

Our data not only revealed that enhanced H_2O_2 affected the metabolites in human and murine pancreatic cancer cells, but also highlight that the valine, nordeoxycholic acid, palmitoycatnitine, LysoPC(18:3), PC(40:4) and PC(30:2) may be required for PDAC development.
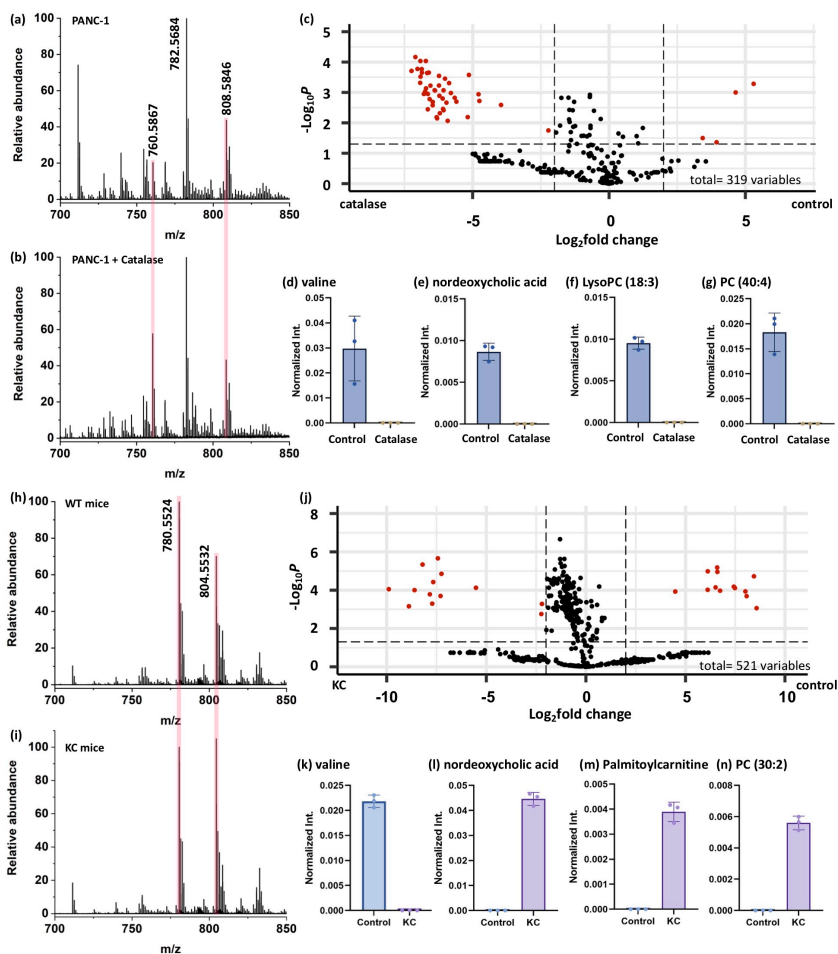
Figure 3. Metabolic changes caused by H₂O₂. (a) average mass spectrum of PANC-1 cell lysate. (b) average mass spectrum of a lysate of PANC-1cells treated with catalase. (c) volcano plot of the correlations between the P-values and fold changes for the metabolite signals in PANC-1 cells and PACN-1 cells treated with catalase. Relative intensities of (d) valine, (e) nordeoxycholic acid, (f) LysoPC(18:3) and (g) PC(40:4) in PANC-1 cells and PACN-1 cells treated with catalase are shown in the bar plots. (h) average mass spectrum of an acinar cell lysate. (i) average mass spectrum of a lysate of acinar cells bearing the oncogenic KRAS mutation. (j) volcano plot of the correlations between the P-values and fold changes for the metabolite

167

signals in normal acinar cells and acinar cells bearing the oncogenic *KRAS* mutation. Relative intensities of (k) valine, (l) nordeoxycholic acid, (m) palmitoylcarnitine and (n) PC(30:2) in normal acinar cells and acinar cells bearing the oncogenic KRAS mutation are shown in the bar plots.

3.4 Hydrogen Peroxide Promotes the Survival of *KRAS* Mutant PDAC Cells.

The above results revealed that H_2O_2 was dysregulated in PDAC cells. To investigate whether targeting H_2O_2 is beneficial for PDAC treatment, we first inhibited H_2O_2 in PANC-1 cells and BxPC-3 cells with catalase. As shown in Figures 4a and b, inhibition of H_2O_2 decreased the cell viability of PANC-1 cells, but inhibition of H_2O_2 had no significant effect on the cell viability of BxPC-3 cells. To prove that H_2O_2 is indeed the oxidant, we added catalase to inhibit H_2O_2. When H_2O_2 was inhibited, no COH was detected (Figures S7a and b). To further demonstrate that the decrease in PDAC cell viability was caused by the inhibition of H_2O_2, we inhibited all ROS in PDAC cells with N-acetylcysteine (NAC), which is the general ROS scavenger. As shown in Figures S7c-f, the cell viability of PANC-1 cells decreased when all ROS in the cells were removed, while the cell viability of BxPC-3 cells did not change significantly, consistent with the results obtained from the inhibition of H_2O_2 alone. In line with this, we found that catalase treatment induced more cell death indicated by trypan blue assay and apoptosis revealed by apoptosis marker cleaved caspase 3 in PANC-1 cells (Figures 4c and d), indicating that H_2O_2 promotes the survival of PDAC cells.
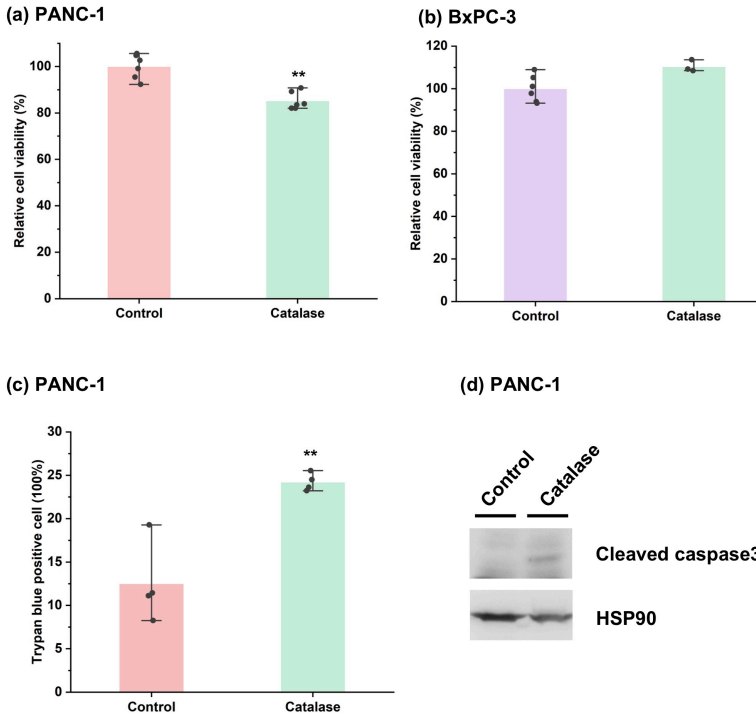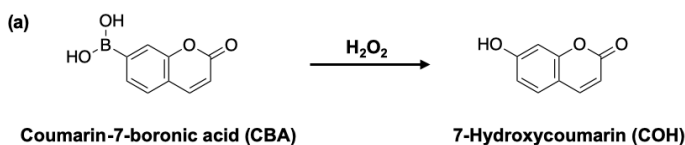
Figure 4. Hydrogen peroxide promotes the survival of KRAS mutant PDAC. (a-b) Relative cell viability detected by MTT assay in PANC-1 and BxPC-3 cells. Mean ± SD. **, $p<0.01$. (c) Trypan Blue assay indicating cell death in PANC-1 cells. Mean ± SD. **, $p<0.01$. (d) IB analysis of total cell lysate isolated from PANC-1 cells described in (a). Cleved caspase 3 antibody was used to monitor the apoptosis level. Hsp 90 used as protein loading control.

4. Conclusions

ROS play important roles in tissue homeostasis, cellular signalling, differentiation, and survival in both healthy and disease context. Literature reported that ROS were also dysregulated and had important roles in PDAC, while the detailed roles of specific ROS in PDAC had remained unclear. In this study, we applied powerful mass

spectrometry, genetic and molecular biology, as well as genomic sequencing data analysis techniques to analyze KC mice and human PDAC cells. We found that H_2O_2, but not other ROS, was dysregulated in PDAC. Moreover, we identified that the oncogenic *KRAS* mutation promoted H_2O_2 production and silenced *CAT* levels in PDAC, which may be the main reason for H_2O_2 enrichment in PDAC cells. Furthermore, we identified that H_2O_2 strongly affected the metabolites profile and promoted the survival of PDAC cells. These findings not only highlight that targeting H_2O_2 might be beneficial for PDAC therapy, but also remind us to study ROS individually with novel techniques instead of taking ROS as one single biochemical entity.
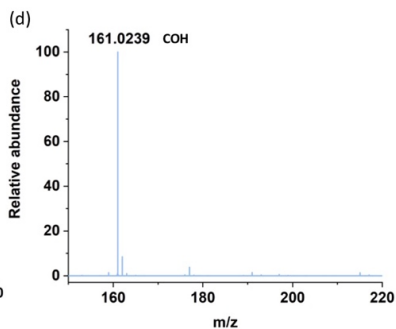
5. Supporting information

(a)

Coumarin-7-boronic acid (CBA) $\xrightarrow{H_2O_2}$ 7-Hydroxycoumarin (COH)

(b)

Salicylic acid $\xrightarrow{\bullet OH}$ 2,3-DHBA

(c)

Hydroethidine (HE) $\xrightarrow{O_2^{\bullet-}}$ 2-Hydroxyethidium (2OH-E+)
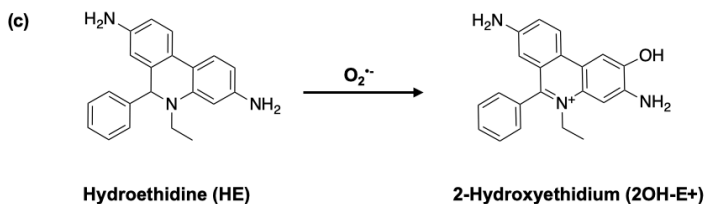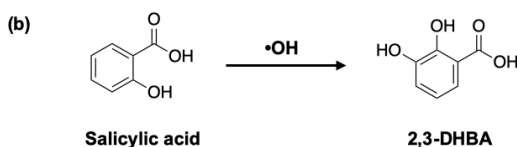
Figure S1. Probes and formed products from different ROS. (a) H_2O_2 reacts with CBA to generate COH detected as $C_9H_5O_3^-$, m/z 161.0239. (b) ·OH reacts with salicylic acid to generate 2,3-DHBA detected as $C_7H_5O_4^-$, m/z 153.0187. (c) $O_2^{·-}$ reacts with HE to generate 2OH-E$^+$ detected as $C_{21}H_{20}N_3O^+$, *m/z* 330.1601.

Mutant band:100 bp
WT band: 250 bp

Mutant band: 200 bp
WT band: 380 bp
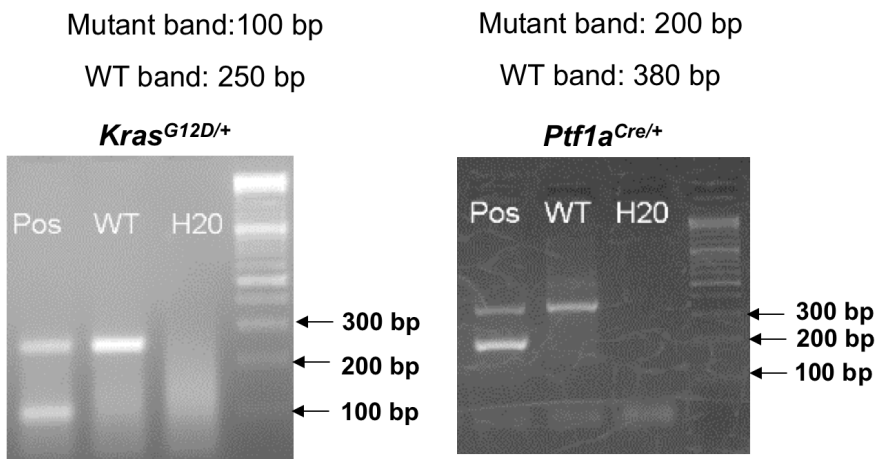
Figure S2. Representive genotyping results of $Kras^{G12D/+}$ and $Ptf1a^{Cre/+}$ mice.

172
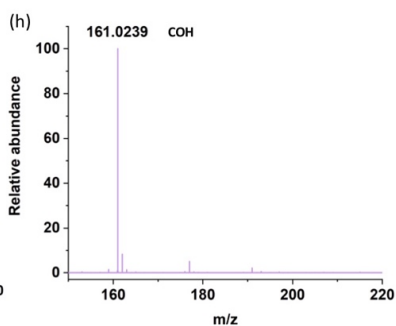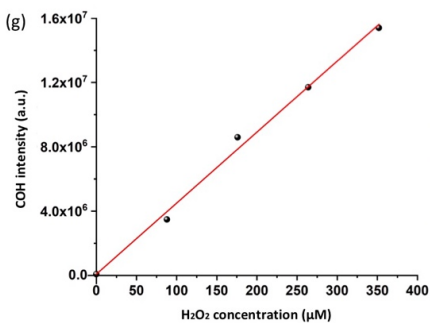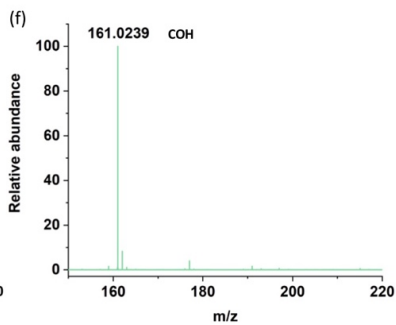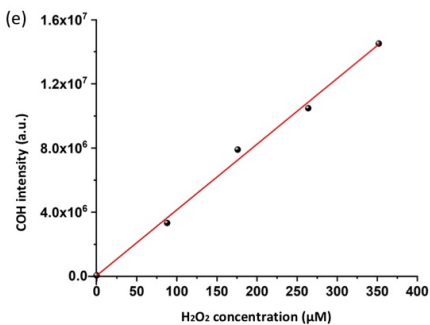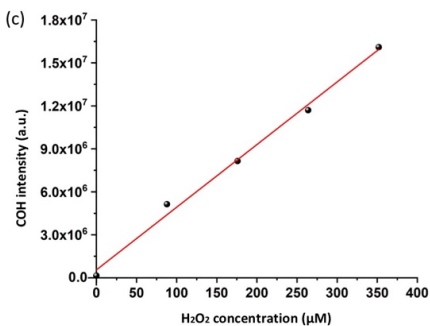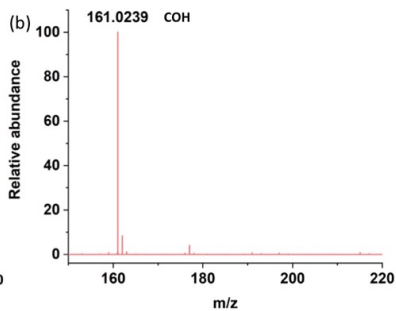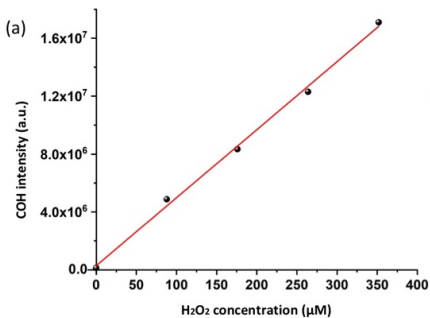
Figure S3. Positive control experiment for COH formation. (a) calibration curves for COH formed by CBA and H_2O_2 in PANC-1 cell lysate. (b) mass spectrum of PANC-1 cell lysate. (c) calibration curves for COH formed by CBA and H_2O_2 in CFPAC-1 cell lysates. (d) mass spectrum of CFPAC-1 cell lysate. (e) calibration curves for COH formed by CBA and H_2O_2 in H6C7 cell lysates. (f) mass spectrum of H6C7 cell lysate. (g) calibration curves for COH formed by CBA and H_2O_2 in BxPC-3 cell lysates. (h) mass spectrum of BxPC-3 cell lysate.
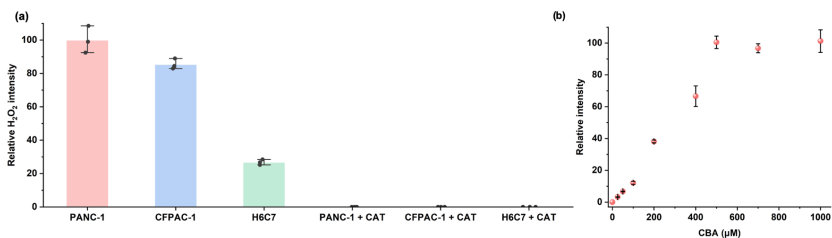
Figure S4. (a) Relative H_2O_2 intensity in PANC-1, CFPAC-1, H6C7, PANC-1 treated by CAT, CFPAC-1 treated by CAT, and H6C7 treated by CAT. (b) optimization of CBA concentration.
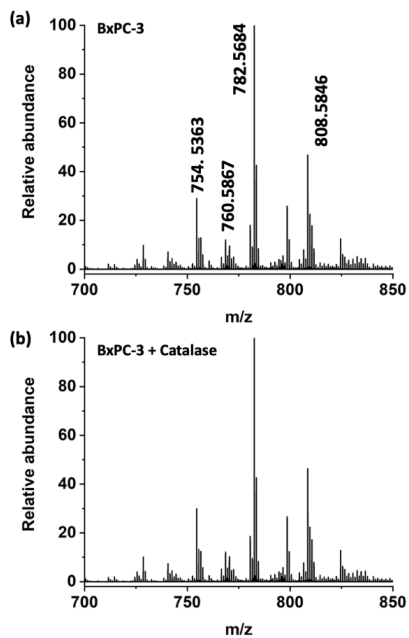
Figure S5. (a) average mass spectrum of BxPC-3 cell lysate. (b) average mass spectrum of a lysate of BxPC-3 cells treated with catalase.

174
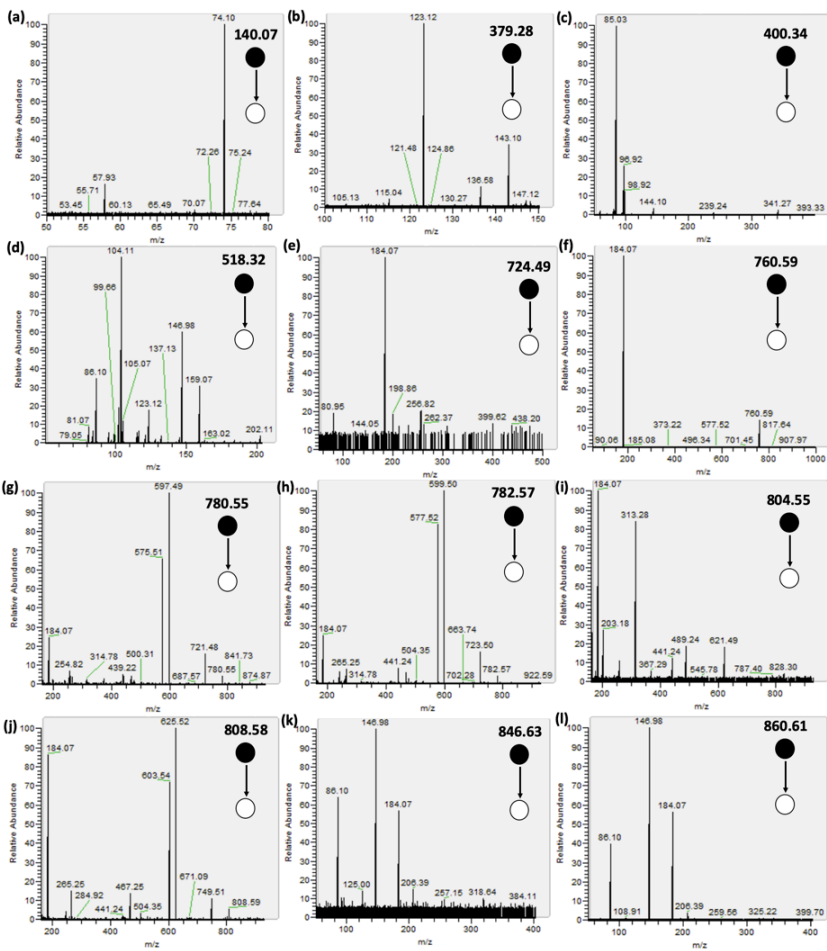
Figure S6. The MS/MS spectra used for metabolites assignment.

Table S1. Metabolites assignment.

	Putative metabolites	Adducts	Measured, m/z	Theoretical, m/z	Mass error, ppm	MS² fragments
1	Valine	[M+Na]⁺	140.0683	140.0682	0.71	74.1
2	Nordeoxy cholic acid	[M+H]⁺	379.2831	379.2843	3.16	123.12
3	Palmitoyl carnitine	[M+H]⁺	400.3451	400.3421	7.49	85.03, 341.27
4	LysoPC(18:3)	[M+H]⁺	518.3251	518.3241	1.93	104.11, 184.07
5	PC(30:2)	[M+Na]⁺	724.4873	724.4888	2.07	184.07
6	PC(34:1)	[M+H]⁺	760.5871	760.5851	2.61	184.07
7	PC(34:2)	[M+Na]⁺	780.5524	780.5514	1.23	184.07, 575.51
8	PC(36:4)	[M+H]⁺	782.5678	782.5694	2.04	184.07, 599.50, 723.50
9	PC(38:7)	[M+H]⁺	804.5532	804.5538	0.71	184.07, 621.49
10	PC(38:5)	[M+H]⁺	808.5841	808.5851	1.21	184.07
11	PC(42:5)	[M+H-H₂O]⁺	846.6386	846.6377	1.06	184.07
12	PC(40:4)	[M+Na]⁺	860.6143	860.614	0.35	184.07
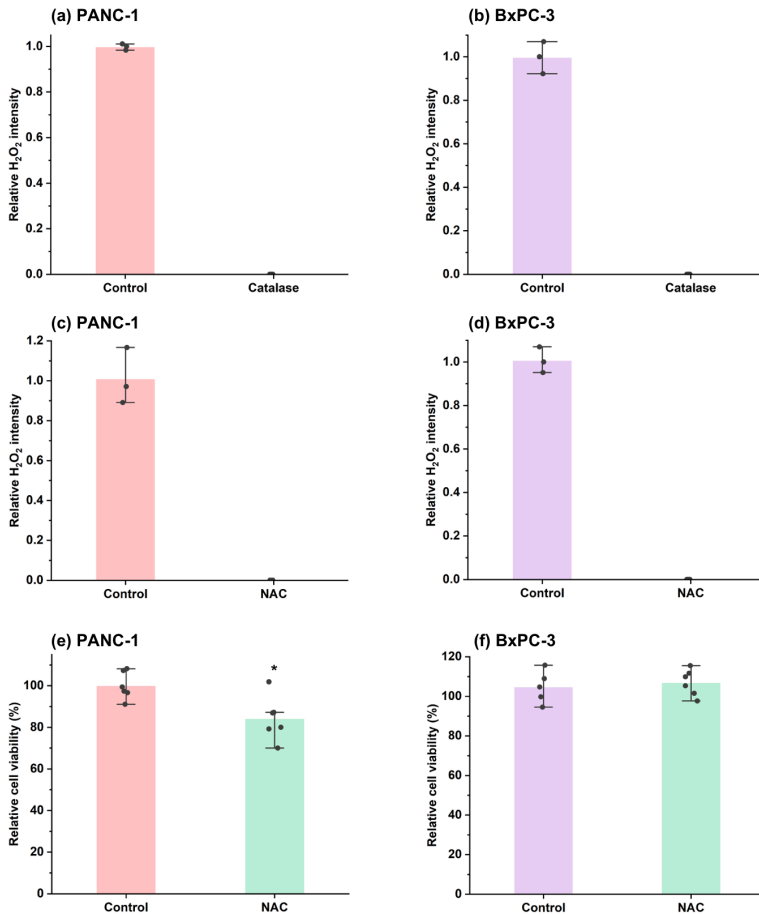
Figure S7. Hydrogen peroxide promotes the survival of KRAS mutant PDAC. (a) Relative H_2O_2 intensity in PANC-1 cells and PANC-1 cells after catalase treatment. (b) Relative H_2O_2 intensity in BxPC-3 cells and BxPC-3 cells after catalase treatment. (c) Relative H_2O_2 intensity in PANC-1 cells and PANC-1 cells after NAC treatment. (d) Relative H_2O_2 intensity in BxPC-3 cells and BxPC-3 cells after NAC treatment. (e-f) Relative cell viability detected by MTT assay in PANC-1 and BxPC-3 cells.

References

(1) Finkel, T.; Holbrook, N. J. Oxidants, oxidative stress and the biology of ageing. *Nature* **2000**, 408, 239-247.

(2) Hayes, J. D.; Dinkova-Kostova, A. T.; Tew, K. D. Oxidative Stress in Cancer. *Cancer Cell* **2020**, 38, 167-197.

(3) Chio, I. I. C.; Tuveson, D. A. ROS in Cancer: The Burning Question. *Trends in Molecular Medicine* **2017**, 23, 411-429.

(4) Cheung, E. C.; DeNicola, G. M.; Nixon, C., et al., Dynamic ROS Control by TIGAR Regulates the Initiation and Progression of Pancreatic Cancer. *Cancer Cell* **2020**, 37, 168-182 e164.

(5) Chio, I. I. C.; Jafarnejad, S. M.; Ponz-Sarvise, M., et al., NRF2 Promotes Tumor Maintenance by Modulating mRNA Translation in Pancreatic Cancer. *Cell* **2016**, 166, 963-976.

(6) Ge, W.; Goga, A.; He, Y., et al., miR-802 Suppresses Acinar-to-Ductal Reprogramming During Early Pancreatitis and Pancreatic Carcinogenesis. *Gastroenterology* **2022**, 162, 269-284.

(7) Liu, Q.; Ge, W.; Wang, T., et al., High-Throughput Single-Cell Mass Spectrometry Reveals Abnormal Lipid Metabolism in Pancreatic Ductal Adenocarcinoma. *Angew. Chem., Int. Ed.* **2021**, 60, 24534-24542.

(8) Zhao, H.; Joseph, J.; Fales, H. M., et al., Detection and characterization of the product of hydroethidine and intracellular superoxide by HPLC and limitations of fluorescence. *Proc. Natl. Acad. Sci. U. S. A.* **2005**, 102, 5727-5732.

(9) Kojima, R.; Takakura, H.; Kamiya, M., et al., Development of a Sensitive Bioluminogenic Probe for Imaging Highly Reactive Oxygen Species in Living Rats. *Angew. Chem., Int. Ed.* **2015**, 54, 14768-14771.

(10) Maskiewicz, R.; Sogah, D.; Bruice, T. C. Chemiluminescent reactions of lucigenin. 1. Reactions of lucigenin with hydrogen peroxide. *J. Am. Chem. Soc.* **1979**, 101, 5347-5354.

(11) Tsamesidis, I.; Egwu, C. O.; Perio, P., et al., An LC-MS Assay to Measure Superoxide Radicals and Hydrogen Peroxide in the Blood System. *Metabolites* **2020**, 10.

(12) Melov, S.; Coskun, P.; Patel, M., et al., Mitochondrial disease in superoxide dismutase 2 mutant mice. *Proc. Natl. Acad. Sci. U. S. A.* **1999**, 96, 846.

(13) Dickinson, B. C.; Chang, C. J. A Targetable Fluorescent Probe for Imaging Hydrogen Peroxide in the Mitochondria of Living Cells. *J. Am. Chem. Soc.* **2008**, 130, 9638-9639.

(14) Beissenhirtz, M. K.; Scheller, F. W.; Lisdat, F. A Superoxide Sensor Based on a Multilayer Cytochrome c Electrode. *Anal. Chem.* **2004**, 76, 4665-4671.

(15) Hu, K.; Relton, E.; Locker, N., et al., Electrochemical Measurements Reveal Reactive Oxygen Species in Stress Granules*. *Angew. Chem., Int. Ed.* **2021**, 60, 15302-15306.

(16) Zhou, N.; Qiu, T.; Yang-ping, L., et al., Superoxide anion radical generation in the NaOH/H2O2/Fe(III) system: a spin trapping ESR study. *Magn. Reson. Chem.* **2006**, 44, 38-44.

(17) Zhang, Y.; Dai, M.; Yuan, Z. Methods for the detection of reactive oxygen species. *Anal. Methods* **2018**, 10, 4625-4638.

(18) Kalyanaraman, B.; Hardy, M.; Podsiadly, R., et al., Recent developments in detection of superoxide radical anion and hydrogen peroxide: Opportunities, challenges, and implications in redox signaling. *Arch. Biochem. Biophys.* **2017**, 617, 38-47.

(19) Wang, Z. Y.; Li, Y.; Chang, W. Q., et al., Development and validation of a LC/MS-based method for the measurement of intracellular superoxide anion. *Anal. Chim. Acta* **2018**, 999, 107-113.

(20) Xiao, Y.; Meierhofer, D. Are Hydroethidine-Based Probes Reliable for Reactive Oxygen Species Detection? *Antioxid. Redox Signal.* **2018**, 31, 359-367.

(21) Zielonka, J.; Vasquez-Vivar, J.; Kalyanaraman, B. Detection of 2-hydroxyethidium in cellular systems: a unique marker product of superoxide and hydroethidine. *Nat. Protoc.* **2008**, 3, 8-21.

(22) Tuveson, D. A.; Shaw, A. T.; Willis, N. A., et al., Endogenous oncogenic K-ras(G12D) stimulates proliferation and widespread neoplastic and developmental defects. *Cancer Cell* **2004**, 5, 375-387.

(23) Kawaguchi, Y.; Cooper, B.; Gannon, M., et al., The role of the transcriptional regulator Ptf1a in converting intestinal to pancreatic progenitors. *Nat. Genet.* **2002**, 32, 128-134.

(24) Subramanian, A.; Tamayo, P.; Mootha, V. K., et al., Gene set enrichment analysis: A knowledge-based approach for interpreting genome-wide expression profiles. *Proc. Natl. Acad. Sci. U. S. A.* **2005**, 102, 15545-15550.

(25) Adusumilli, R.; Mallick, P. In *Proteomics: Methods and Protocols*; Comai, L., Katz, J. E., Mallick, P., Eds.; Springer New York: New York, NY, 2017, p 339-368.

(26) Gibb, S.; Strimmer, K. MALDIquant: a versatile R package for the analysis of mass spectrometry data. *Bioinformatics* **2012**, 28, 2270-2271.

(27) Sohal, R. S.; Sohal, B. H. Hydrogen peroxide release by mitochondria increases during aging. *Mech. Ageing Dev.* **1991**, 57, 187-202.

(28) Waters, A. M.; Der, C. J. KRAS: The Critical Driver and Therapeutic Target for Pancreatic Cancer. *Cold Spring Harb Perspect. Med.* **2018**, 8.

(29) Pandey, K. B.; Rizvi, S. I. Markers of oxidative stress in erythrocytes and plasma during aging in humans. *Oxid. Med. Cell. Longev.* **2010**, 3, 2-12.

(30) Sies, H.; Jones, D. P. Reactive oxygen species (ROS) as pleiotropic physiological signalling agents. *Nat. Rev. Mol. Cell Biol.* **2020**, 21, 363-383.

B. Curriculum Vitae

Personal information

Name: Qinlei Liu

Date of birth: 29 December 1993
Place of birth: Sichuan Province, China
Email: liuqinleiseven@gmail.com

Education

August 2019 – October 2022

PhD in Analytical Chemistry, Department of Chemistry and Applied
Biosciences, ETH Zurich, Switzerland
Supervisor: Prof. Dr. Renato Zenobi

September 2016 – June 2019

MSc in Analytical Chemistry, Department of Chemistry, Sichuan University,
Sichuan Province, China
Supervisor: Prof. Dr. Chengbin Zheng

September 2012 – June 2016

BSc in Chemistry, Department of Chemistry and Materials Science, Sichuan
Normal University, Sichuan Province, China

Teaching Experience

February 2020 – June 2022 Teaching Assistant at the Laboratory Class in
Analytical Chemistry at ETH Zurich, teaching infrared spectroscopy

Awards

2021 Chemistry Travel Award by SCNAT and SCS

C. Contributions

Publications

1. **Qinlei Liu+,** Sandra Martínez-Jarquín, and Renato Zenobi*. "Recent Advances in Single Cell Metabolomics Based on Mass Spectrometry". (Minor Revision)

2. **Qinlei Liu+,** Wenjie Ge+, Sandra Martínez-Jarquín, Yuliang He, Ri Wu, Markus Stoffel,* and Renato Zenobi*. "Mass Spectrometry Reveals High Levels of Hydrogen Peroxide in Pancreatic Cancer Cells". Submitted for publication.

3. **Qinlei Liu,** Jiayi Lan, Ri Wu, Alina Begley, Wenjie Ge, and Renato Zenobi*, "Hybrid Ionization Source Combining Nano-electrospray and Dielectric Barrier Discharge Ionization for Simultaneous Detection of Polar and Non-polar Compounds in Single Cells". ***Anal. Chem.*** **2022**, *94*, 2873-2881. (DOI: 10.1021/acs.analchem.1c04759)

4. **Qinlei Liu+,** Wenjie Ge+, Tongtong Wang, Jiayi Lan, Sandra Martínez-Jarquín, Christian Wolfrum, Markus Stoffel, and Renato Zenobi*, "High-throughput Single-cell Mass Spectrometry Reveals Abnormal Lipid Metabolism in Pancreatic Ductal Adenocarcinoma". ***Angew. Chem., Int. Ed.,*** **2021,** 60, 24534-24542. (DOI: 10.1002/ange.202107223)

5. **Qinlei Liu** and Renato Zenobi*, "Rapid Analysis of Fragrance Allergens by Dielectric Barrier Discharge Ionization Mass Spectrometry". ***Rapid Commun. Mass Spectrom.,*** **2020,** e9021. (DOI: 10.1002/rcm.9021)

6. **Qinlei Liu**, Yao Lin, Jing Xiong, Li Wu, Xiandeng Hou, Kailai Xu*, and Chengbin Zheng*, "Disposable Paper-based Analytical Device for Visual Speciation Analysis of Ag (I) and AgNPs in Commercial Products". ***Anal. Chem***. **2019,** 91, 5, 3359-3366. (DOI: 10.1021/acs.analchem.8b04609)

7. Ri Wu, Jonas B. Metternich, Prince Tiwari, Lukas R. Benzenberg, Julian A. Harrison, <u>Qinlei Liu,</u> and Renato Zenobi*, "Structural Studies of a Stapled Peptide with Native Ion Mobility Mass Spectrometry and Transition Metal Ion Förster Resonance Energy Transfer in the Gas Phase". ***J. Am. Chem. Soc. 2022***, 144, 32, 14441–14445. (DOI: 10.1021/jacs.2c02776)

Conference Contributions

1. The International Mass Spectrometry Conference, (Netherlands), **2022**
    Oral presentation: Hybrid Ionization Source Combining Nano-electrospray and Dielectric Barrier Discharge Ionization for Simultaneous Detection of Polar and Non-polar Compounds in Single Cells

2. 69th ASMS Conference on Mass Spectrometry and Allied Topics, (USA), **2021**
    Poster presentation: High-throughput Single-cell Mass Spectrometry Reveals Abnormal Lipid Metabolism in Pancreatic Ductal Adenocarcinoma Using a Dielectric Barrier Discharge Ionization Source

3. Swiss Group for Mass Spectrometry, (Switzerland), **2021**
    Poster presentation: High-throughput Single-cell Mass Spectrometry Reveals Abnormal Lipid Metabolism in Pancreatic Ductal Adenocarcinoma

4. 61st International Conference on Bioscience of Lipids, (Netherlands), **2021**
    Poster presentation: High-throughput Single-cell Mass Spectrometry Reveals Abnormal Lipid Metabolism in Pancreatic Ductal Adenocarcinoma

5. Swiss Chemical Society Fall meeting, (Switzerland), **2021**
    Poster presentation: High-throughput Single-cell Mass Spectrometry Reveals Abnormal Lipid Metabolism in Pancreatic Ductal Adenocarcinoma

6. Swiss Chemical Society Fall meeting, (Switzerland), **2020**
    Poster presentation: Exploring the high mass limits of ionization with a DBDI source

Qinlei Liu

ETH Zurich